

AN ABSTRACT OF THE THESIS OF

Robert Predosa for the degree of Master of Science in Water Resource Engineering, presented on
June 17, 2016

Title: Lasers in the Sky: Distributed Temperature Sensing and a Micro-Meteorological Approach
to Quantifying Evapotranspiration

Abstract approved: _____

Dr. Chad W. Higgins

Abstract:

Lower atmospheric flux measurements are a difficult subset of atmospheric data to accurately collect. The interplay of cost, precision, specialty, resolution and repeatability compound an already difficult experimental problem. In response to this, a new, novel instrumentation approach to measuring within the atmospheric boundary layer (ABL) is introduced.

The combination of Unmanned Aerial Vehicles (UAVs) and Distributed Temperature Sensing (DTS) technology are an unlikely pairing that show great potential for providing unprecedented levels of spatial and temporal resolution of the natural world. This pairing was deployed to the Oxbow Conservation Area near Bates, OR in July 2015 to measure vertically stratified temperature profiles. Additional modifications to the fiber optic cables were done in order to replicate the sling psychrometer approach to measuring humidity values by replicating a 'dry' and 'wet' bulb thermometer capable of measuring temperature gradients at high spatial and temporal resolutions.

Out of 23 UAV flights conducted, thirteen provided usable data. Measurements and calculations were compared to a co-located Open Path Gas Analyzer and Sonic Anemometer (Irgason) for accuracy and precision. Four flights showed strong correlation to Eddy-Covariance calculations on sensible heat and evaporative flux. More so, the modified DTS field deployment provided new insights into stratified heterogeneities in vapor pressure, temperature, sensible heat, evaporative flux and temperature variance.

©Copyright by Robert Predosa

June 17, 2016

All Rights Reserved

Lasers in the Sky: Distributed Temperature Sensing and a Micro-Meteorological Approach to Quantifying Evapotranspiration

by

Robert Predosa

A THESIS

Submitted to

Oregon State University

In partial fulfillment of
the requirements for the
degree of
Master of Science

Presented June 17, 2016

Commencement June 2017

Master of Science thesis of Robert Predosa presented on June 17, 2016

APPROVED:

Major Professor, representing Water Resources Engineering

Director of the Water Resources Graduate Program

Dean of the Graduate School

I understand that my thesis will become part of the permanent collection of Oregon State University libraries. My signature below authorizes release of my thesis to any reader upon request.

Robert Predosa, Author

ACKNOWLEDGEMENTS

What a ride! In much the same tone, though perhaps with a bit more joviality, I proclaim to the many of those kind enough to council me on this path that, indeed, you we're right; and to the many after who seek my council: please trust what I say! Trust what they told me, for my voice echoes only their wisdom, not merely my experience. And it will be an experience to behold, a challenge like no other, and a reward superior to any other. Embrace it, tackle it – choose your active verb! And don't blink, because it's over; a lifetime's adventures, trials and tribulations suppressed into a microcosm of your life. The tooling you'll need to make a lifetime of impact beyond Corvallis started here two years ago. Now the real fun begins!

Some people embark on a Graduate School experience as a means to supplement a life's ambition or a life's passion. Others begin the walk with an air of inevitability to the process; what else was I going to do? Then there's the wandering minority of us who, whilst head-down plunging through day-to-day stick our heads out of the hunt just long enough to wonder: what else can I do? What more can I do? This momentary lapse in trudging is what brought me to Oregon State University two winters ago in search of a challenge.

Turns out the challenge was the smallest piece of the pie. The world got a little smaller after this experience. More approachable for me than ever before. Big problems, complicated problems; seemingly insurmountable when seen through the lenses I wore to OSU. Now? Still big and complicated, but as with all things, context is king. We've been handed an opportunity and a responsibility to do good things on whatever scale we feel appropriate.

With all that's to be said of the past, and of the future, and of myself; more ought to be said of the shared experience itself.

There's simply no way this experience is fruitful without the constant, patient guidance and support of my advisor, Dr. Chad Higgins. As was mentioned, things simply don't look the same now as they did when I arrived here at OSU, and he, above all, is the reason why.

A special thanks to Jason Kelly as well. Not for one minute did Jason waste time explaining things in simple terms; from day one, whether I liked it or not, I was treated like someone who was – at the very least – *supposed* to know what he was talking about. Thanks to his perspective, patience and persistence form did eventually begin to follow function.

And finally those who walked it with me: thank you. In the classroom, the office, the conference, the trail, the river and the backyard: from those forums our knowledge grew. Through you came the confidence and trust to take it and make something more for tomorrow than we observed yesterday. All that had been forewarned by so many before I began this journey left one thing out: The profound positive effect of patient friends. You all: Kelsey, Joseph, Susan, Alex, Jacob, Kira, Russell, Scott, Idrees, Elnaz.

And a final thanks to Ben Hickson for reading (over and over) drafts of a pile of thoughts. Wouldn't be what it is without your help.

With that, here we go: the culmination of so many hours, so many failed ideas, and just enough successful ones...

TABLE OF CONTENTS

	<u>Page</u>
Introduction	1
Measuring Evapotranspiration and Evaporative Fluxes: A Review of Common Methods	4
<i>Mass Transfer Approaches</i>	4
<i>Energy Balance Approaches</i>	6
<i>Water Balance Approaches</i>	7
<i>Combination Approach: Penman-Monteith Equation</i>	8
Applications of DTS to Environmental Monitoring	8
<i>Raman, Rayleigh backscattering and its application to temperature calculations</i>	9
<i>Calibrating DTS-derived data</i>	10
<i>Physical Considerations when applying DTS to environmental temperature sensing</i>	13
Bowen Ratio, Humidity, Sensible Heat and Evaporation	16
Utilizing the Bowen Ratio with Vertically Distributed Temperature Data to Quantify Evapotranspiration Rates in the Lower Atmosphere	16
Field Deployment and Experimental Design	24
Overview	24
Fiber Optic Cable Used	25
Cable Modifications	26
<i>Duplexed dry Temperature Cable</i>	26
<i>Wet Bulb Cable Modifications</i>	27
Drone Deployment	29

TABLE OF CONTENTS (Continued)

	<u>Page</u>
UAV Regulations	30
Field Deployment	31
<i>DTS</i>	31
Results	33
Overview	33
Summary Data	33
Temperature and Humidity Analysis	35
<i>Statistical Comparison of Irgason and DTS data</i>	35
<i>Temperature and Humidity Profiles</i>	36
Bowen Ratio Analysis	38
<i>Comparing DTS-Derived Bowen Ratio values to Irgason Bowen Ratio Values</i>	41
Sensible and Evaporative Flux Values	42
<i>Comparing Profile Data to Irgason Data</i>	42
Variance	45
Results Recap	47
Discussion: Positives, Shortcomings, and Moving Forward	49
Feasibility of DTS as a Humidity Measuring Device	49
The Implementation of UAV's for Broader Atmospheric Sensing	52
Response Times, Sampling Rates and Variance	54

TABLE OF CONTENTS (Continued)

	<u>Page</u>
On the Critical Components of the Calculation Process	59
Summary	60
Appendix A: Temperature and Specific Humidity Profiles	62
Appendix B: Flux Plots	69
Appendix C: Variance Plots	76
Appendix D: Bowen Ratio Plots	79
Bibliography	86

LIST OF FIGURES

Figure:

Figure 1: DTS Field setup for Calibration.....	25
Figure 2: Example of Stokes, Anti-Stokes backscatter data, plotted.....	26
Figure 3: Example Bowen Ratio Plot.....	34
Figure 4: Sample of a Reynolds Decomposition Plot.....	36
Figure 5: Map of Field Site.....	38
Figure 6: Image of Duplexed Fiber Optic Cable.....	40
Figure 7: Image of Fiber Optic Cable Wrapped with Yarn, Vent Tape.....	41
Figure 8: Field DTS set up for John Day DTS Flights.....	46
Figure 9: Comparison Plots of Specific Humidity and Temperature.....	49
Figure 10: Vertical Profiles of Wet Bulb, Dry Bulb and Specific Humidity.....	51
Figure 11: Example of Plot used for Bowen Ratio Calculations, with phases.....	52
Figure 12: Bowen Ratio Plot, Flight 47.....	53
Figure 13: Bowen Ratio Plot, Flight 37.....	54
Figure 14: Comparison Plot of Bowen Ratio Values.....	55
Figure 15: Sensible and Latent Heat Profile Plot, Flight 36.....	56
Figure 16: Sensible and Latent Heat Profile Plot, Flight 47.....	57
Figure 17: Sensible and Latent Heat Profile Plot, Flight 37.....	58
Figure 18: Variance Profile Plots, Flights: 36, 37, and 47.....	60
Figure 19: Comparison Plot of Variance Values.....	60
Figure 20: Plot of Sensible Heat from Irgason and DTS over Time of Day.....	61
Figure 21: Example Plot of Stratified Error in Wet Bulb Cable.....	64
Figure 22: Plot of DTS Data Showing Morning Transition, Hermiston, OR.....	67

LIST OF TABLES

Table

Table 1: Information of UAV's: flight time, load capacity..... 43

Table 2: Summary Data Values used in Calculations..... 48

LIST OF VARIABLES AND CONSTANTS

Values Listed are with units typically used. May not always be exact units listed here.

	DESCRIPTION	UNITS
α	Differential attenuation between Stokes and Anti-Stokes signals within fiber optic cable	<i>unitless</i>
a_{psy}	Fitting parameter for windspeed-dependent calculations of the psychrometric constant, γ .	<i>unitless</i>
β	Bowen Ratio	<i>unitless</i>
C	Distributed Temperature Sensing (DTS) fitting parameter	<i>unitless</i>
C_1	Fitting parameter within Evaporation equation	<i>unitless</i>
c_p	Specific heat capacity of dry air	<i>kJ/kg K</i>
ρ_{air}	Density of dry air (unless subtext notes otherwise)	<i>g/m³</i>
E	Evapotranspiration, or Evaporative flux	<i>W/m²</i>
e_a	Actual vapor pressure of moist air	<i>kPa</i>
$e_{s,w}$	Saturation vapor pressure for dry bulb, wet bulb calculation	<i>kPa</i>
g	Gravity	<i>m/s²</i>
γ	1: Photon energy shift, DTS calibration equation 2: Psychrometric Constant	<i>unitless</i> <i>kPa/K</i>
H	Sensible Heat Flux	<i>W/m²</i>
K	Von Karman Constant, dimensionless parameter	<i>unitless</i>
L	Characteristic length	<i>m</i>
LE	Latent heat energy	<i>W/m²</i>
λ_e or L_e	Latent heat of evaporation/vaporization of water in air	<i>kJ/kg or MJ/kg</i>
m	Mass	<i>g or kg</i>
P	Pressure	<i>kPa</i>
R_d	Gas constant	<i>unitless</i>
RH	Relative humidity	<i>unitless</i>
σ	Standard deviation	<i>unitless</i>
σ^2	Variance	<i>unitless</i>

LIST OF VARIABLES AND CONSTANTS (Continued)

DESCRIPTION	UNITS
SH Specific Humidity	g_{water}/kg_{air}
T Temperature	$^{\circ}K$ or $^{\circ}C$
\bar{T} Mean Temperature	$^{\circ}K$ or $^{\circ}C$
T' Temperature prime. Value absolute distance from \bar{T}	$^{\circ}K$ or $^{\circ}C$
θ Potential Temperature	$^{\circ}K$ or $^{\circ}C$
$\bar{\theta}$ Mean Potential Temperature	$^{\circ}K$ or $^{\circ}C$
θ' Potential temperature prime.	$^{\circ}K$ or $^{\circ}C$
V Volume	m^3
u, v, w Component wind velocities in x,y,z direction, respectively	m/s
z 1: Measured distance along cable from photon sensor within DTS	cm or m
2: Height	m

Additionally, units may be subscripted to indicate which device the measurement came from, i.e.

T_{DTS} VS T_{IRGA} .

Introduction

When considering the movement of water on regional and global scales, water is transported in massive quantities not only as a liquid, but as a vapor as well. Precipitation and evapotranspiration of water between these two states drives the hydrologic cycle (Brutsaert, 2005). However, water vapor makes up an annual average storage of only 25mm if equivalently spread out over the entirety of the Earth. Groundwater, by comparison, would cover the earth with approximately 45 meters of water (Korzoun, 1978). Therefore, the importance of water vapor in the hydrologic cycle doesn't lie in the mass or volume of water transferred, but rather in the energy that gets transferred and moved.

The large thermal energy storage capacity of water in conjunction with the abundance of water across the Earth's surface results in the changing of phase from liquid to vapor to be a primary energy transfer mechanism between the atmosphere and the Earth. Re-condensed vapor is a surrogate for that energy transfer, and is thus a significant component driving changes in atmospheric conditions on larger scales (Brutsaert, 2005). Hydrologic interconnectedness on a global scale is then through oceanic processes primarily, but also through atmospheric ones. Being able to quantify the transition of water into a vapor phase from either evaporation or plant transpiration allows for a greater understanding of both local and regional system dynamics. Further, being able to repeatedly quantify this phenomenon, regardless of vegetation cover, soil type, and water availability would be a powerful approach to measuring energy and mass transfer of water vapor off the Earth's surface. It may become convenient to imagine a scenario by which this approach to measuring evaporative flux significantly contributes to precision agriculture,

further honing in on water budget, thus significantly reducing water usage and loss due to evaporation.

On a local level, precisely measuring evapotranspiration (ET) is a difficult task to complete, relative to measuring groundwater or surface water, for example. Current technologies adequately provide precise information on evaporative fluxes and evapotranspiration rates on field scales, though the instrumentation and data analysis required to obtain this information is costly and complex, and thusly limited to specialists or the academic realm only. Less expensive, hand-held tools exist for measuring humidity, and while evaporation rates can be gleaned from this information through calculation or conversion methods, this information is low accuracy and provides little more than a gross estimation of the amount of water in the local atmosphere at any given time.

When looking at traditional measuring techniques – summarized in the pages that follow – for their spatial and temporal resolution in conjunction with their cost and implementation, the demand for a new approach appears. For example, the eddy-covariance approach, while perhaps one of the most precise methods for measuring mass, energy and momentum fluxes in the lower atmosphere, becomes prohibitively expensive when attempting to measure vertical profiles of atmospheric information. Each device, a gas analyzer and a sonic anemometer, requires installation on field-towers. The most robust field deployment for these would require using fixed, tall towers on the order of at least 30m, severely limiting data collection locales. The larger problem then for approaching data collection of these vertical profiles is multi-fold: too costly, too specialized, limited to where one can collect profile data via infrastructure limitations, and a lack of accuracy provided. These issues provide an impetus for wanting to develop a method to

measure these data in a new way that is accurate, moveable, relatively easy to implement and in time, less costly as well. Distributed Temperature Sensing (DTS) technology, in conjunction with the use of unmanned aerial vehicles (UAV's), provides the – seemingly unlikely – potential to fill a data collection niche.

DTS systems have provided new insights on groundwater flow, hyporheic flow energy exchange, and other environmental fields (Tyler et al., 2009). The importance of ET in the hydrologic cycle, and its importance in energy transfer between the Earth and atmosphere (Brutsaert, 1982) has driven scientists to use DTS systems as a potential tool for measuring the lower atmosphere. Nocturnal and morning boundary layer atmospheric measurements have been undertaken in a few instances, and the results have proven to be promising (Keller et al., 2011; Thomas et al., 2012; Zeeman et al., 2015). The approach and analysis of this thesis is to accurately measure evapotranspiration through a profile in the lower atmosphere using the innovative work, technology and methods being conducted with DTS and atmospheric sensing. For the data collected to test this approach, a series of field experiments were conducted at the Oxbow Conservation Area, east of John Day, OR.

Evaporative flux of the lower atmosphere above a pasture was measured by utilizing a mass balance approach within the application of the Bowen Ratio to temperature data collected through a DTS system. The field design and modifications of our fiber optic system was inspired by the concept of the sling psychrometer: creating a wet and dry bulb temperature measurement technique vertically resolved within the lower atmosphere.

A brief summary of various approaches to evapotranspiration are documented, followed by a description of DTS technology and its application to environmental sciences. The field experiment in Eastern Oregon utilized unmanned aerial vehicles (UAVs) to deploy fiber optic cables through a vertical profile, and so a justification of UAV technology is also given. Analysis of the vertical temperature and humidity profiles observed in John Day are reviewed. Finally, a discussion on the potential of this approach moving forward, improvements on experimental design and setup, and implications on future works are discussed.

Measuring Evapotranspiration and Evaporative Fluxes: A Review of Common Methods

There are three primary approaches to measuring evapotranspiration: mass balance, energy balance, and water balance methodologies (Brutsaert, 1982, 2005). Field instrumentation technologies and numerical models have been developed that can take advantage of each of these approaches, all of which have provided trusted results that the lexicon has accepted as reliable methodologies.

Mass Transfer Approaches

Calculations involving the movement of water itself is the most direct approach to determining evapotranspiration, and it is recommended that this methodology be utilized whenever possible (Brutsaert, 2005). Perhaps the most well-known approach under this category is the use of lysimeters. Lysimeters require a well-defined control space, making them ideally suited for understanding the relationship between evapotranspiration, root water uptake and soil water retention in an academic setting. While their expense and complexity are a worthy

scientific justification for creating a control space that can accurately account for evapotranspiration, their applications beyond academic endeavors are limited.

The Eddy Covariance method, originally developed in the 1950's by Swinbank, Obukhov and Montgomery (Aubinet et al., 2012; Swinbank, 1951), takes advantage of atmospheric turbulence being the primary mechanism for mass and momentum transport to precisely measure vertical fluxes of water vapor, carbon dioxide and sensible and latent heat exchange between the surface and the ground (Aubinet et al., 2012). This methodology has been widely accepted since the early 1990's as a reliable approach to measuring continuous flux measurements (Aubinet et al., 2012). An example of the applicability of the Eddy Covariance Method is the FLUXNET project; a national network of Eddy Covariance towers, funded by NASA and the National Science Foundation. This network provides continuous data collection and computational resources for scientists (fluxnet.ornl.gov). Although this project is an example of the extent to which Eddy Covariance data is collected and utilized, the implementation of Eddy Covariance instrumentation is limited largely to the scientific community (Dingman, 2008).

Soil water budget approaches can also be done to estimate evapotranspiration. Instrumenting, the input and output of water into a soil system. Measuring changes in soil water content in the root zone provides information necessary for estimating evapotranspiration. This 'bucket' approach is popular for its simplicity, though it can also be instrumentally stringent, as in the case of the implementation of tools like a neutron probe. Additionally, it provides only a generalized measurement of water in vapor state through deduction and doesn't provide a perspective on the distribution of vapor in the local atmosphere.

Energy Balance Approaches

A common energy balance approach to quantifying water movement through a hydrologic system is the implementation of sap-flow Sensors. Sap flow sensors attempt to measure water transport through trees – analogous to a choke point in the path of water from precipitation to interception, root uptake, and finally re-released as water vapor through stomata. Typically, sap flow measuring approaches utilize the application and measuring of heat. By precisely measuring how heat is transferred via sap flow, or how it is dissipated, transpiration rates can be quantified (Davis et al., 2012). This approach is limited, necessarily, to forest systems where evaporation rates are negligible compared to transpiration rates. More often than not, tree and stand health are metrics analyzed via this type of information.

A more sophisticated energy balance method, yet relatively simple in comparison to Eddy Covariance is surface renewal. This approach assumes a parcel of air with a given measurable parameter, or scalar (temperature, wind speed, water vapor), will descend and interact with the canopy top for a short amount of time. At some point, that parcel of air will rise, severing contact with the canopy top. A new parcel of air will take its place, and the process begins anew. The parcel leaving the surface has with it those measurable metrics. The interaction phase, or ‘ramp’ phase is where the scalar – water vapor when using a mass balance approach – quantity is either added or removed from the air parcel. The second, faster ‘ejection’ phase marks the end of the cycle for the air parcel. High frequency measuring of these events can measure fluxes of these scalars by measuring length and height of these parcels of air (Castellví, 2012). Vertical transport is the necessary component being observed. Though many inputs are also required for a surface

renewal analysis, these inputs are relatively easier to measure and are cheaper to accurately measure (Castellví and Snyder, 2010).

An increasingly popular approach to measuring sensible and latent heat fluxes – our ultimate goal – is the use of scintillometers. Scintillometers measure changes in the intensity of light, or light fluxes that are caused by turbulent eddy's moving through the transmitted light path. Scintillometers provide temperature and humidity data that can be applied with Monin-Obukhov Similarity Theory to estimate sensible and latent heat fluxes over, depending on the type of scintillometers used, several kilometer ranges (Geli et al., 2012). This approach, along with Eddy-Covariance, Surface Renewal, and other Bowen Ratio approaches, depend on a homogenous land surface, and a relatively flat terrain in order for estimates to be considered reliable (Fedorovich, 2011; Geli et al., 2012).

A classic, and simpler, energy balance approach that evapotranspiration can be derived from is the Bowen Ratio; the ratio between sensible heat and latent heat (moisture) in a system (Bowen, 1926). Packed into the latent heat variable is the latent heat of vaporization of water and evaporative flux rate. Thus, by knowing the change in humidity over time and the latent heat of vaporization of water, one can use this method to calculate evapotranspiration. This approach is what was utilized in this study, and is discussed in further detail.

Water Balance Approaches

Water balance approaches are simplest in term of conceptual understanding. In these cases, evapotranspiration is the only unknown parameter in the hydrologic water budget equation. Theoretically, if one could continuously measure all components of the hydrologic

cycle in a controlled volume, then the rate of state change resulting from evapotranspiration could be determined. However simple this is conceptually, it is impractical and often inaccurate in application (Brutsaert, 2005).

Combination Approach: Penman-Monteith Equation

Perhaps the most widely recognized standard used to measure evapotranspiration over a vegetated surface is the Penman Monteith-Equation (Dingman, 2008). The two versions of Penman's approach discussed here are a blend of mass balance and energy balance approaches. The Penman, approach was initially developed to calculate evapotranspiration without the need to measure surface temperature (Penman, 1948). Van Bavel later came up with an approximation that has become known as the Combination Approach. Van Bavel was able to eliminate many empirical constants, and showed the flexibility and range (i.e., over water, bare soil and over vegetated surfaces) of the original Penman Model (Van Bavel, 1966).

The formal Penman-Monteith equation widely used today incorporates the combination approach. Additionally, by incorporating the canopy conductance factor, the formal Penman-Monteith equation has become a standard by which ET over vegetated surfaces can be calculated (Brutsaert, 2005; Dingman, 2008).

Applications of DTS to Environmental Monitoring

Distributed Temperature Sensing was originally developed for the oil and gas industry in the early 1980's, and was used primarily for hot spot detection and fire monitoring, among other industrial applications. (Dakin et al., 1985; Kersey, 1996) More recently, environmental scientists, hydrologists and other natural scientists have appropriated this high spatial and temporal

resolution technology for a range of applications in surface water, groundwater and atmospheric science monitoring (Bakker et al., 2015; Bond et al., 2015; Briggs et al., 2012; Zeeman et al., 2015). As will be described in more detail, the high spatial (distributed) and temporal resolution of DTS-derived temperature data is capable of providing up to four orders of magnitude more data than conventional point measurements. This improved data density has provided a robust new approach to measuring hyporheic zone exchanges, groundwater source flows, stream temperature profiling, and, most pertinent to our study, atmospheric boundary layer profiling (de Jong et al., 2015; Euser et al., 2014; Keller et al., 2011; Thomas et al., 2012; Zeeman et al., 2015).

Raman, Rayleigh backscattering and its application to temperature calculations.

DTS technology comes in many forms, all of which measure changes in laser light waves travelling through a fiber optic cable (Selker et al., 2006; Ukil et al., 2012). The type of DTS system utilized in field experiments throughout this project worked on the physical principle of Raman Backscattering. The underlying physical phenomenon is theoretically straightforward; however, its implications for temperature sensing are profound.

In the transmission of light through the glass core of a fiber optic cable, the photons interact with electrons within the glass. This interaction produces one of two results: the light may be directly reflected by the molecule's electron (the specific interaction being described here involves that between a light wave and an electron only) and not lose any energy at all, or it will be absorbed by the molecule and re-emitted at a significantly higher or lower energy level (Ferraro et al., 2003; Selker et al., 2006). In cases of the application of spectrometry, the quantifiable increase or decrease in energy from the incident beam is used to identify specific

molecules (Ferraro et al., 2003). In DTS systems however, the sum of re-emitted wavelengths is measured (Ukil et al., 2012).

When a beam of light (typically in the visible or ultraviolet spectrum) interacts with electron clouds, the wavelength and frequency of the return is very nearly the same as the incident beam. This identical return is called Rayleigh backscattered light. In DTS systems, Rayleigh backscattered light is filtered out of the return, leaving only the comparatively fewer ($\sim 10^{-5}$ compared to incident) re-emitted light waves, which are referred to as Stokes and Anti-Stokes Raman backscattered light (Ferraro et al., 2003).

Calibrating DTS-derived data

With the determination of the ratio of Stokes (shorter wavelength) to the Anti-Stokes (longer wavelength) light waves, the temperature at the point of collision between the incident light wave and the molecules of glass within the core of the fiber can be calculated. Whereas the Stokes values are only a function of energy transmission (wave amplitude), Anti-Stokes light waves are a linear function of energy transmission and an exponential function of the temperature of the molecule the incident beam interacted with (Selker et al., 2006). Therefore, taking the ratio of these two eliminates the energy level, leaving only a value that is a function of the temperature of the interaction at the measured location within the cable (Selker et al., 2006)

Knowing the wavelength of the incident beam, and being able to calculate the time of return of the backscattered photons, the precise distance from the DTS instrument's photon detector can be calculated. (Hausner et al., 2011). In order to calculate temperature with respect to distance from the sensor, the distribution of temperature along the cable must be calibrated

to account for photon energy shift (γ), differential attenuation between the Stokes and Anti-Stokes backscattered photons ($\Delta\alpha$), and a third dimensionless parameter (C) (Kobs and Hausner, 2015). The equation below is the foundational theory for this process (Hausner et al., 2011).

$$T(z) = \left(\frac{\gamma}{\ln\left(\frac{P_s(z)}{P_{as}(z)}\right) + C - \Delta\alpha} \right)$$

The resulting temperature data, if raw Stokes and Anti-Stokes data are collected and calibrated correctly, is a dataset that is orders of magnitude (both spatially and temporally) ahead of other temperature measuring devices (Hausner et al., 2011).

Provided experimental design of the field deployment is carefully considered, calibrating DTS data is a relatively simple process. There are a series of ways in which a fiber optic temperature configuration can be implemented: Single-ended, duplexed single-ended and double-ended. (Hausner et al., 2011). The field equipment developed for the John Day field study utilized a duplexed, single-ended calibration configuration (Figure 1).

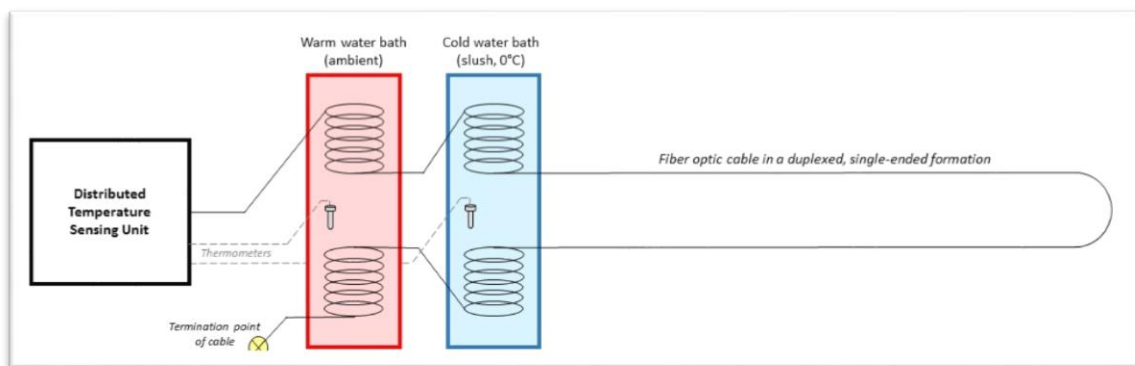


Figure 1: Diagram of a duplexed, single-ended fiber optic cable calibration configuration. This configuration allows for a cable configuration that provides two temperature values at essentially the same point in space. Thermometers provide independent measurements of water bath temperatures over time and are used as calibration metrics for calculating $\Delta\alpha$ in the calibration equation.

The important part of configuring DTS systems is in creating tightly controlled temperature regions along the cable that are independently measured. This is commonly done by coiling a significantly long section (typically enough for 40 or more spatial measurements) of cable inside

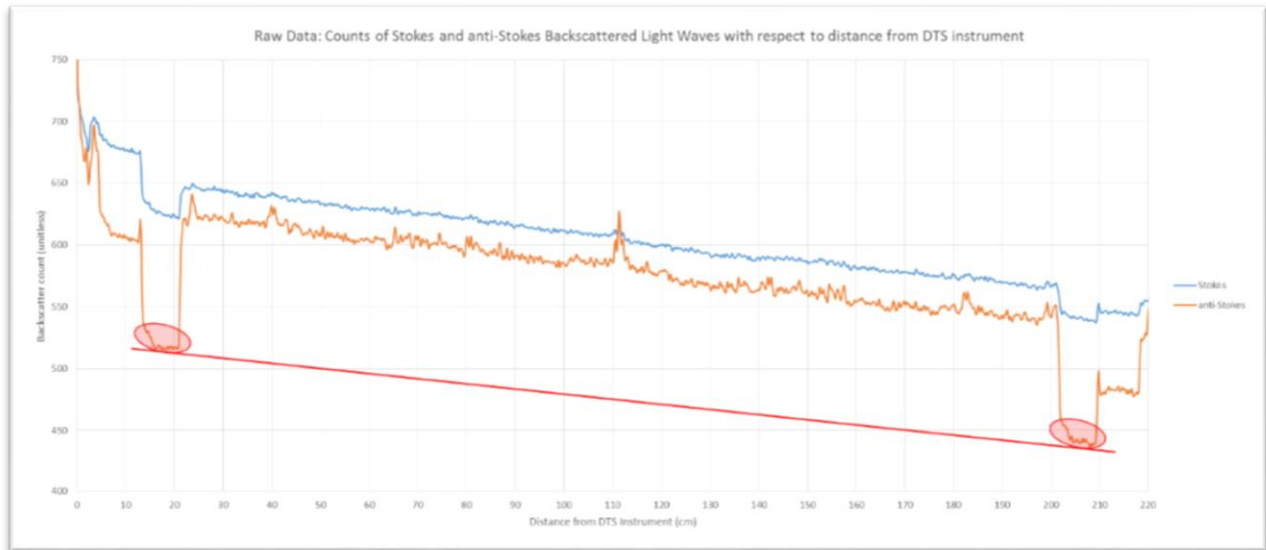


Figure 2: Sample plot of collected Stokes and Anti-Stokes values. Y-axis represents the number of Stokes and Anti-Stokes light waves the DTS instrument detected as a result of a collision along every critical distance (12.5cm in this case) from the instrument. The red line and red ovals indicate the critical pieces of data correlating to known temperatures along the cable, used for calculating the first of three calibration constants in the equation given earlier, α .

a pair of warm or ambient temperature and cold-water baths (red and blue boxes, Figure 1). This configuration allows for the maximization of temporal resolution, though it may sacrifice some precision in temperature reading, due to differential attenuation (Tyler et al., 2009), one of a series of issues covered in following sections.

Figure 2 demonstrates a raw Stokes and Anti-Stokes signal plot. The red line superimposed on the data correlates to the first set of data used to calculate $\Delta\alpha$. Accounting for the linear negative slope inherent in the data due to attenuation, the loss of backscatter return density is determined first. Using the known mean temperature of the ambient and cold water baths allows one to solve for the final two fitting parameters, C and Y.

Physical Considerations when applying DTS to environmental temperature sensing

There are a number of physical considerations that must be taken into account when applying this system to environmental monitoring (Hilgersom et al., 2016). While many considerations apply to helical configurations of fiber optic cables to further enhance spatial resolution along an axis (vertically typically), many physical limitations must also be taken into account when using fiber optic deployments in straight-line configurations. To address these considerations, the difference between the equipment's resolution and true spatial resolution; cable construction and size; solar radiation; and differential attenuation must be carefully considered with mitigation measures applied either in the field or during post-processing.

Regardless of cable type, instrument type, or length of cable, there is a fundamental difference between an instrument's physical resolution and the resulting sampling resolution that may be considered an accurate reflection of reality (Hilgersom et al., 2016; Tyler et al., 2009). Tyler et al, 2009 established a value for determining effective spatial resolution in a laboratory experiment. Their experiment determined that: "spatial resolution of the DTS system [is] the length of fiber [optic cable] required to show 90% of the known temperature change" (Tyler et al., 2009). The essential point of Tyler's experiment was to demonstrate the difference between advertised resolution of the DTS machine; what the device is mechanically capable of collecting, and what the fiber optic cable's material properties are capable of actually responding to in the physical world.

For example, the instrument used in this experiment, the Silixa Ultima S ("Ultima DTS Datasheet," 2015) has an advertised spatial resolution of 12.5cm and a maximum temporal resolution of 1 second (1Hz). Based on the Tyler et al. (2009) determinations, this would translate

to the physical spatial resolution for accurate readings in applying the Silixa Ultima S to be 27.5cm. When thinking of a temperature change at two points along the cable then, it can be reasonably determined that 90% of the change between the two temperature values can be resolved inside of 27.5cm.

For temporal resolution, the physical response of the machine is more directly applicable to reality, as this measurement depends primarily on the machine's ability to quickly count Stokes and Anti-Stokes waves returning to the sensor (Tyler et al., 2009). The longer the count, or the more counts averaged into a single return signal value; the less variance in the precision of the temperature reading that can be expected.

Temporal resolution is also a factor when choosing a fiber optic cable. A fundamental consideration is the heat capacity of the cable (Tyler et al., 2009). The relationship between cable diameter and heat capacity should be considered, as should the cable construction (i.e. cable sheath material type and thickness, reinforcing material, secondary sheathing, etc...). The thinner the cable, and with the fewest internal reinforcing layers separating the fiber from the ambient environment, the faster the cable will respond to ambient temperature changes.

In addition to the consideration of the cable itself and to temperature calculations from the backscattered data, solar radiation (solar loading) must be considered. Incoming short-wave radiation creating a radiant flux is a known and relevant phenomenon to sensitive field equipment. This is a significant contributor to the commonly observed phenomena of an object sitting in the sun being typically hotter than the air surrounding it. Because short-wave radiation

can be a significant influence on the exposed cable, it must be considered when collecting measurements of the atmosphere during hot, sunny days.

Differential attenuation is yet another phenomenon to consider when using DTS systems. Differential attenuation issues arise when a factor other than temperature affects the ratio between Stokes and Anti-Stokes values. While this is of particular importance for the consideration of helical cable deployments (Arnon et al., 2014; Hilgersom et al., 2016), it is a factor in linear cable deployments as well. The best way to reduce this problem is in the initial field set up. For a single ended calibration, accounting for this linear trend is relatively easy to account for.

Though the physical and numerical considerations inherent in the configuration of a distributed temperature sensing system are significant, the information gleaned from its data has the potential to provide insight into atmospheric systems that is unprecedented compared to conventional measurement systems.

Bowen Ratio, Humidity, Sensible Heat and Evaporation

Utilizing the Bowen Ratio with Vertically Distributed Temperature Data to Quantify Evapotranspiration Rates in the Lower Atmosphere.

Of the many approaches available to calculating ET, many of them require multiple data inputs that can be arduous and time intensive to collect. The primary motivation for the application of DTS to data collection for ET calculations is to reduce the variety of data inputs needed for accurate calculations and improve vertical resolution and precision of data collected. In this case, only temperature profiles of the lower atmosphere need to be calculated, with appropriate modifications to fiber optic cables being made so as to mimic a wet bulb, dry bulb approach to measuring temperature.

The foundational Bowen Ratio equations is,

$$\beta = \frac{H}{LE} \quad (1)$$

Where H is sensible heat, and LE is latent heat. Latent heat is the product of the latent heat of vaporization of water and evapotranspiration, E. Thus,

$$\beta = \frac{H}{L_e E} \quad (2)$$

Brutsaert, 2005, indicates that the Bowen Ratio can also be described in a mean profile method that includes specific humidity and potential temperature only.

$$\beta = \frac{c_p(\overline{\theta_1} - \overline{\theta_2})}{L_e(\overline{SH_1} - \overline{SH_2})} \quad (3)$$

In this equation, c_p is the specific heat capacity of water, θ is potential temperature and SH is specific humidity. A final form of the equation for evaporation via this mean profile, mass balance approach is:

$$E = \frac{H(\overline{SH_1} - \overline{SH_2})}{c_p(\overline{\theta_1} - \overline{\theta_2})} \quad (4)$$

This will be returned to later on. Returning to the original Bowen Ratio shows that, when looking at vertical profiles, the ratio of actual air temperature and vapor pressures is what is required (Bowen, 1926). This original ratio, when multiplied by the psychrometric constant, provides a value with respect to height (Euser et al., 2014),

$$\beta(z) = \gamma \frac{(T_2 - T_1)}{(e_{a2} - e_{a1})} \quad (5)$$

In this form, temperature, T, replaces potential temperature, as the difference between the two is negligible near the Earth's surface (Brutsaert, 2005). Actual vapor pressure at the two points is then determined. γ , is the determining factor in this approach. It is important to note the misnomer of the label for γ , as it is actually pressure-dependent,

$$\gamma \equiv \frac{c_a P}{0.622 L_e} \quad (6)$$

Here, c_a is the specific heat capacity of air, P is pressure, and 0.622 is the fixed ratio of the molecular weight of water vapor over the molecular weight of dry air (Allen et al., 1998). L_e is the latent heat of vaporization of water.

An established method for approximating L_e , varying with temperature, can be done with the following approximation (Dingman, 2008),

$$L_e = 2.50 - 0.0124T_{air} \quad (7)$$

T_{air} is in °C, and L_e is in MJ/kg. This approximation is accurate over the range of temperatures found in our field deployment, and so was used to approximate L_e . Traditional values of L_e are approximated at anywhere from 2257 to 2264 kJ/kg (Brutsaert, 1982; Dingman, 2008; Stull, 1988).

Work completed by Allen et al, 1998 indicated that in fact the psychrometric constant is, practically, a function of wind speed at the site as well, giving an approximation for γ ,

$$\gamma = a_{psy}P \quad (8)$$

Where a_{psy} represents the temperature-dependent coefficient affecting the psychrometric constant. a_{psy} increases as wind speed decreases, due to the lack of advective energy present to induce evaporative cooling of the wet-bulb temperature measurement (Allen et al., 1998). It is important to note that the above equation is an approximation for evaluating the psychrometric constant based on wind speed and pressure. This is done to account for the dependence of the wet bulb temperature output being a factor of wind speed (Allen et al., 1998; Euser et al., 2014).

All of the above is derived in a manner such that a wet bulb-dry bulb approach to determining humidity values can be obtained. The intermediate step between what has been described above and what is needed to make final calculations is the determination of the

saturation vapor pressures for dry bulb and wet bulb temperatures, and finally an actual water vapor pressure calculation. The general form of saturation vapor pressure, or the vapor pressure depending on the wet bulb and dry bulb temperatures collected is (Allen et al., 1998):

$$e_s = 0.61e^{\frac{17.3T_{w,d}}{T_{w,d}+237}} \quad (9)$$

Where $T_{w,d}$ represents the dry or wet bulb temperature. This equation is a common approximation for vapor pressure, similar to the Clausius Clapeyron Equation.

The actual vapor pressure, or the vapor pressure being calculated based on the actual amount of water vapor in the air at time t , is given by (Allen et al., 1998; Dingman, 2008; Euser et al., 2014),

$$e_a = e_s - \gamma(T_a - T_w) \quad (10)$$

This final equation is the last piece of information needed to return to,

$$\beta = \gamma \frac{(T_1 - T_2)}{(e_{a1} - e_{a2})} \quad (11)$$

With this, now the Bowen Ratio can be calculated using only temperature and vapor pressure calculations of the wet and dry bulb temperature values obtained.

Euser, et al provides a final equation incorporating both (Euser et al., 2014):

$$\beta = \gamma \frac{T_{d,2} - T_{d,1}}{(e_{s,2} - e_{s,1}) - \gamma(T_{d,2} - T_{d,1}) + \gamma(T_{w,2} - T_{w,1})} \quad (12)$$

T_d and T_w are the dry and wet bulb temperatures collected. Information on (11), save the psychrometric constant, can be obtained by plotting actual air vapor pressure, e_a , against actual air temperature, T_d , for every point, z (Euser et al., 2014), and determining the slope made by the data.

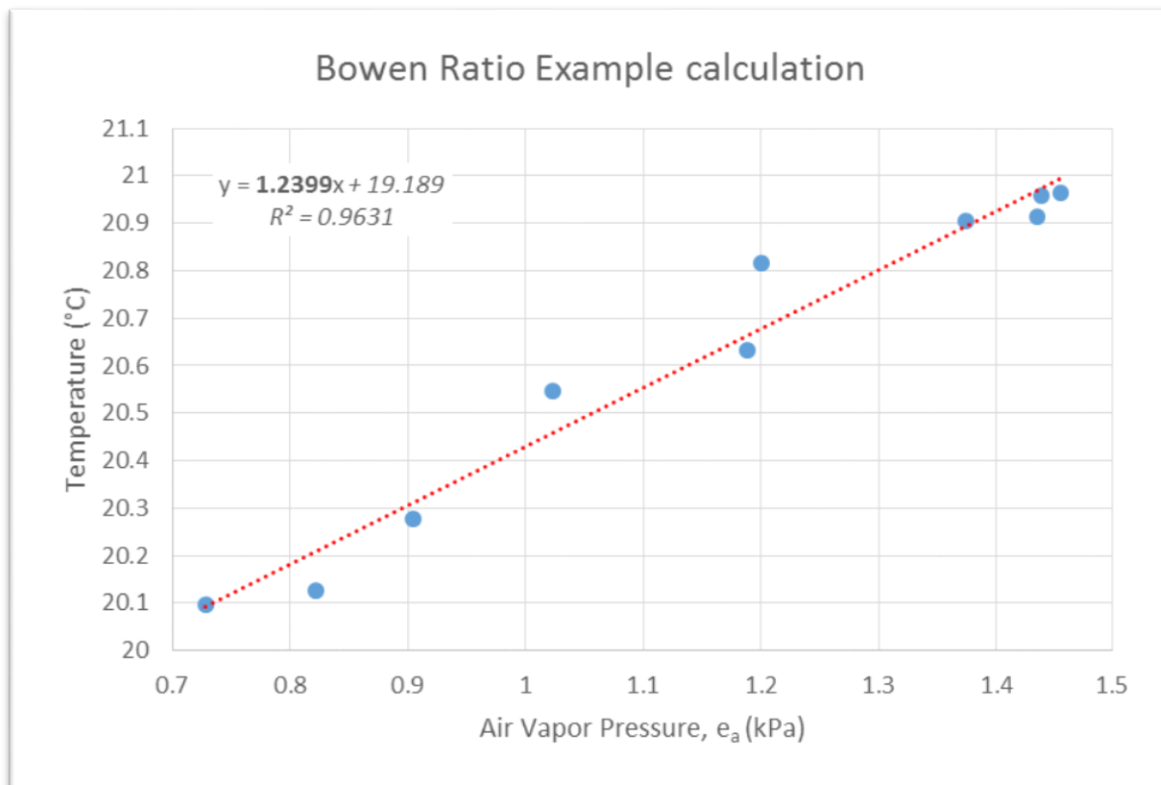


Figure 3: Example of how to use a plot of temperature and moist air vapor pressure to obtain a critical piece of the Bowen Ratio calculation. The slope value, in bold, subset of figure 3, multiplied by γ , is the full Bowen Ratio calculation.

The plot in figure 3 shows an example of this technique. The Bowen Ratio calculation via a vertical mean profile method is therefore a sound way to gather relevant information on sensible and latent heat flux. The next step is, as was mentioned above, to calculate relative and absolute humidity. Relative Humidity can be defined as:

$$RH = \frac{e_a}{e_{s,d}} * 100 \quad (13)$$

Where $e_{s,d}$ is the saturation vapor pressure of dry air (Allen et al., 1998; Dingman, 2008).

The calculation of relative humidity is an important intermediate step in ultimately determining the absolute humidity, or actual amount of water vapor in the air. The derivation from relative to absolute humidity is necessarily a multistep process, but involves (12), the ideal gas law and a final form of mass per volume; the unit equivalent of absolute humidity (Allen et al., 1998).

$$\frac{m}{V} = \frac{e_a}{R_v T} \quad (14)$$

In the above equation, e_a is the actual vapor pressure, dependent on relative humidity (or in this case, on the wet and dry bulb calculations from the DTS temperature profiles), R_v is universal gas constant, and T is the actual air temperature. The final humidity value to consider is specific humidity,

$$SH \approx 0.622 \frac{e_a}{P} \quad (15)$$

This approximation provides an equivalent value in g_{H2O}/kg_{air} (Stull, 1988). This approximation is more sensitive to error propagation at lower e_a values.

Equation (4) has one variable embedded in it that has not been accounted for, and is critical for the final evaporative flux calculations: sensible heat, H . Because only dry bulb and wet bulb temperature data can be used, a novel approach to calculating H is necessary. Tillman, et al provides an approximation for sensible heat that can be utilized (Tillman, 1972),

$$H = \frac{\rho c_p \sigma^{1.5} (KgZ)^{1.5}}{T_{db}^{0.5} C_1^{-1.5}} \quad (16)$$

H is sensible heat, and the new parameters, σ , K, and C_1 , are the temperature variance, Von Karman constant, and a fitting parameter derived empirically (Tillman, 1972). Calculating the dry air temperature variance is the critical piece of information that allows for the calculation of sensible heat. Variance of temperature with respect to height can be derived via a Reynold's decomposition of co-located temperature measurements. This is one reason why a duplexed fiber optic cable was utilized.

Reynold's averaging of a signal – in this case, temperature measurements – can be thought of as a conflation of a signal's mean value over time, and the fluctuations from that mean value at every sampling point in time (Figure 4).

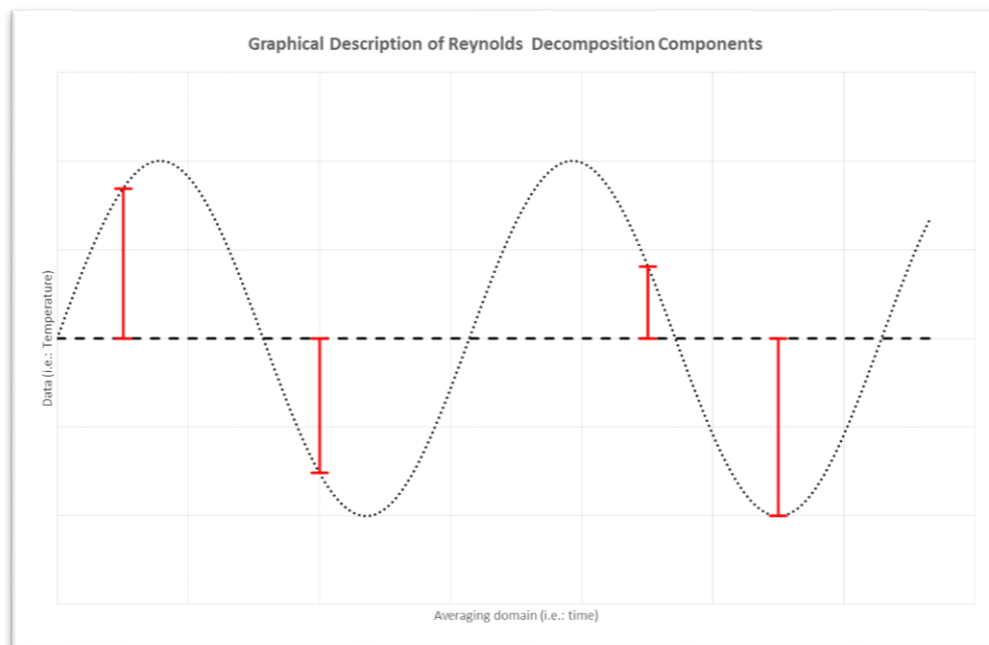


Figure 4: Graphical generalization of how data is comprised in a Reynolds Decomposition. Data collected over time or space consists of actual points of information (the dotted line) that can be taken as discrete values, and the time or space average of those points (dashed line). The deviation between the two (the red lines) are the second part of the decomposition.

The mathematical description is,

$$T = \bar{T} + T' \quad (17)$$

Here, T' is the deviation from the mean T . Temperature data collected is T , and the mean temperature is over a sufficiently long averaging period, thus, a simple calculation can be made on temperature values collected by the duplexed temperature cable, To calculate the covariance, both prime values are needed (Stull, 1988),

$$\sigma_T = \overline{T'_1 * T'_2} \quad (18)$$

This covariance value can then be inserted into (14) to calculate sensible heat flux. The final step in this process is to calculate evaporative flux, E . Combining (12), (16), (18) into (4), the following result is obtained,

$$E = \frac{c_p \sigma_T^{1.5} (Kgz)^{0.5}}{\gamma \frac{\Delta T}{\Delta e a} T_d^{0.5} C_1^{1.5}} \quad (19)$$

Equation (19) is therefore the equation that can be numerically solved for to calculate the evaporative flux at any point where dry bulb and wet bulb temperature values were collected. When applied to the vertical profile data collected during our field study, a vertical evaporative flux with respect to height, z , can be obtained.

Field Deployment and Experimental Design

Overview

Data for analysis was obtained during two summer field campaigns just outside John Day, Oregon (Figure 5). The first of these two experiments took place from June 20th – 22nd, 2015; the second campaign was the following month, from July 18th – 21st, 2015. The local geography of the field site was ideal for the intended purpose of the field experiments. For best measurements,

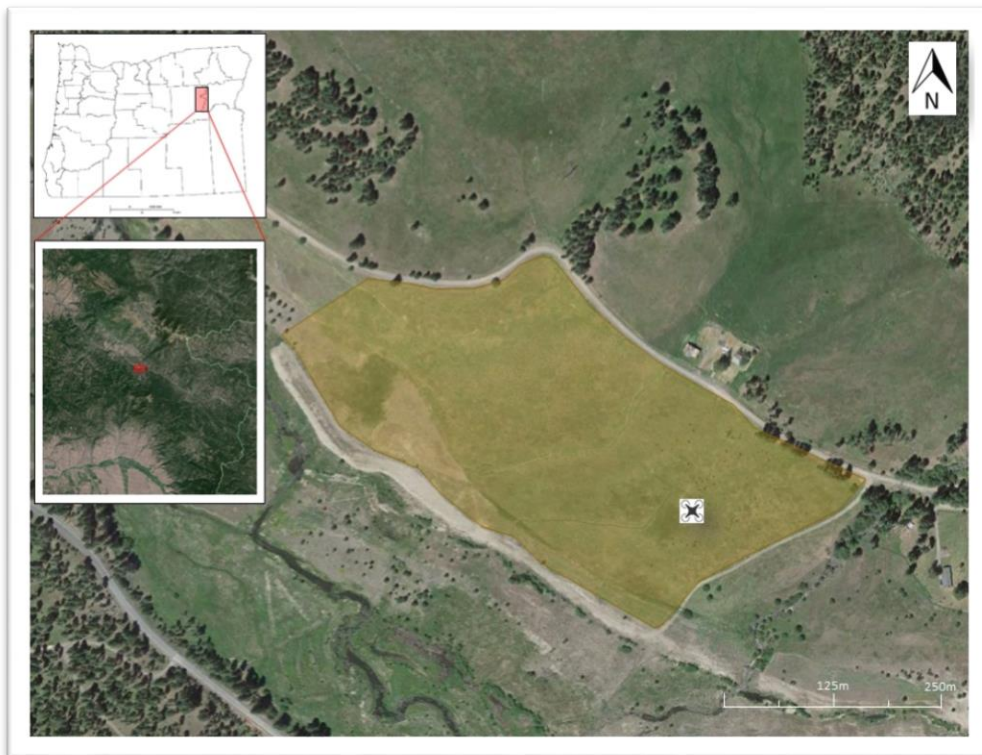


Figure 5: Location of field site. Highlighted section of map is the representative field area; vegetation is homogeneous and land surface is flat, with an average elevation of 1150m, with a deviation of 15 m from the mean, over an area of approximately 0.13 km².

the field site must be flat and homogeneous. The field site (highlighted, Figure 5) is approximately 0.13 km² with a mean elevation of 1150 m with a deviation of 15 m. During the July deployment, an extensive vegetation survey was done in conjunction with another field study being simultaneously conducted. Primary species were bluegrass (*Poa*), meadow foxtail (*Alopecurus*)

and field rushes (*Juncus*). The percent of dead species was elevated, at approximately 63.0%. The vegetation cover however, could still be thought of as homogeneous, as the vegetation types were of similar height and size.

To measure vertical profiles of the formation of the mixed layer from a stable evening layer of the atmosphere, UAV's were used to deploy the DTS fiber optic cables. The primary objective of the June deployment was to measure vertical temperature profiles of air temperature during the morning transition; a critical time in the development of atmospheric phenomena resulting from heat energy added to the ground at sunrise (Stull, 1988). Of all of these flights, only six were dedicated to attempting to capture data for humidity calculations. The July deployment was also primarily intended to measure a vertical profile of temperature during the morning transition, however, 23 flights were also conducted to capture data needed for calculating humidity, sensible heat, and evaporation.

Fiber Optic Cables Used

For all field campaigns, a 900 micron, white, pvc-jacketed cable was used. This had two important physical characteristics; it's response to temperature changes was on the same order of magnitude our DTS device could measure temporally (~1.0 seconds). The cable sheath's material properties meant minimal effects on temperature values due to solar loading. Mathematical corrections for solar loading on cables do exist, however, studies show that the cable utilized in these field experiments exhibited negligible effects resulting from solar loading (de Jong et al., 2015).

Cable Modifications

Duplexed dry Temperature Cable

The local precision, with respect to time, of temperature data from distributed temperature sensing technology is limited and data can be noisy. For most applications (stream monitoring or groundwater monitoring, for example) this noise is easily averaged out if a long enough temporal averaging period is taken. Atmospheric temperature fluctuations are more subtle and occur at higher frequencies, meaning seemingly noisy data has inside it a representation of reality as well. To maximize the potential for DTS to accurately reflect subtle, fast changing air temperatures, the signal noise of the DTS must be minimized in as many ways as possible. In addition to accurate calibration with the use of constant temperature baths, a cable that is capable of physically responding to sudden atmospheric changes, and the use of the calibration equation from Hausner et al., 2011, the cables were duplexed to provide the ability to further increase precision of the temperature data collected. To duplex the cables, two extents of a single cable were braided together (Figure 6).



Figure 6: Sample of duplexed cabling configuration. Node distances varied slightly, but were approximately 2.5 cm apart, providing a physical resolution six times greater than DTS spatial resolution. This resolution guaranteed the DTS machine itself would be the limiting resolution factor.

Braiding the cable in this fashion provided co-located temperature values that could be assumed to be the same point in space. While the nodal distance in the twisted-together cable varied, the mean distance was 2.5cm, providing a physical resolution that was well below the 12.5cm sampling resolution.

Wet Bulb Cable Modifications

For an accurate wet-bulb temperature to be measured, the cable measuring through the modification must stay completely saturated. Modifications to the fiber optic cable were done with this consideration in mind.

Two types of modification of the fiber optic cables intended to collect measurements for humidity, sensible heat, and evaporation were configured. These cables however, were not duplexed in the same manner as dry temperature. The first modification (Figure 7a) had a yarn-wrapped fiber then taped over with a high permeability tape. The yarn was a 52% acrylic, 48% cotton blend. The cotton provided the hydrophilic parameter needed, and the acrylic

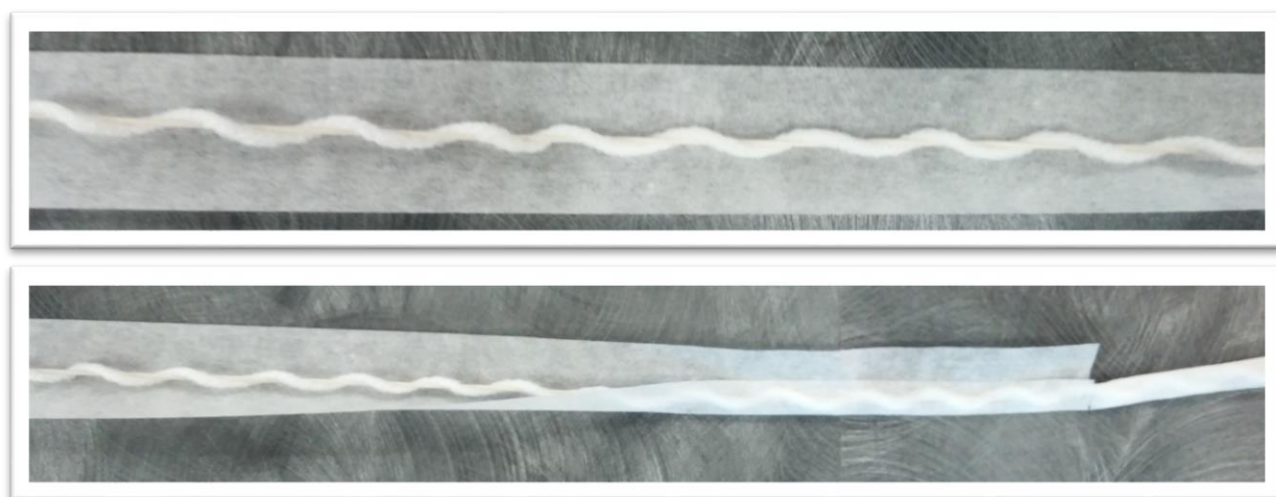


Figure 7 a, b: Figure 7 a shows the initial design of the wet bulb fiber optic cable. The cable was first coated with a blended cotton and acrylic yarn of medium weight. A similar design, without the addition of the cotton/acrylic yarn was used in the John Day, OR field experiments.

(acetonitrile polymer), though not hydrophilic, provided strength and stability within the yarn and – relative to cotton – was less resistive to water vapor advecting from the modified cable.

The tape, manufactured by 3M (“3M Specifications Sheet for Vent Tape: Technical Specifications Sheet,” n.d.), was used to fix yarn to the fiber optic cable as well as to provide an extra reservoir for water. An acrylic adhesive on one side of the porous, non-woven tape is designed to maintain its adhesive properties at higher humidity values. (“3M Specifications Sheet for Vent Tape: Technical Specifications Sheet,” n.d.). The water resistant acrylic adhesive provided repeatability to wetting the modified cables without degradation of the yarn.

The braiding of the yarn was intended to act as a water reservoir analogous to the cotton used for a typical sling psychrometer. Qualitative lab experiments showed that, under mild winds ($\sim 3\text{m/s}$), the vent tape alone would stay saturated for approximately 15-20 minutes after having been soaked in tap water for 10 minutes. Adding cotton to the cable-tape modification proved to add saturation time beyond what a typical flight time would be. The negative to this modification was weight (table 1).

Once the yarn was woven around the cable, the tape was folded over the braided modification. Three sections of fiber optic cable, each approximately 100m in length, were modified in this matter. Two more 75m sections of cable were modified with only the addition of vent tape. Originally constructed as a contingency, this modified tape was what was utilized in the July field deployment.

Table 1: Summary information on cable weights and drone's flight times and lift capacities.

Drone Model	Approx. Flight Time (mins)	Lift Capacity (grams)
3D Robotics: IRIS+	16-22 mins	400g
Turbo Ace: Matrix-S	25 mins (bat. dependent)	1130g/1500g
Cable Modification	Weight Per meter	Estimated max Elevation Given weight per meter
3M Tape + Duplex	4.65 g/m + 3.25 g/m	50 m (IRIS); >100 m (Matrix)
Cotton/Tape + Duplex	6.7 g/m + 3.25 g/m	40 m (IRIS); >100 m (Matrix)
Duplexed, braided cable	3.25 g/m	123.1 m (IRIS); >100 m (Matrix)

By ensuring a fiber optic cable could hold moisture and maintain saturation for a period of time, yet be able to readily diffuse water vapor away from its reservoir, humidity, sensible heat, and finally evaporation was postulated to be calculable from the data collected.

Drone Deployment

For the summer, 2015 deployments, both the drones listed in table 1 were utilized. For the June, 2015 field deployment, the Matrix UAV was deployed. This platform was ideal for our implementation purposes as its payload capacity was strong enough to test out multiple cable modifications at once, while maintaining our desired design altitude of 100 m. A total of twenty flights were conducted over three days. Of the twenty flights attempted, 14 were conducted with only the duplexed cable deployed. These flights were designed to capture the full, lower atmospheric profile during the morning transition. Additionally, 6 flights were conducted with the cotton-braided, taped fiber optic cable. These initial flights were to field-test the safety and

feasibility of utilizing a drone for the deployment of multiple cables. Data from these flights were not used in analysis, as comparative data to confirm results was not available.

The July, 2015 deployment provided the vertical temperature for this analysis. A total of 75 flights were conducted over four days to collect vertically stratified temperature data. A total of 51 flights were conducted using the smaller payload IRIS+ drone with only the duplexed cable attached. With only the duplexed cable, maximum reachable altitude was approximately 70m. For the 23 wet bulb temperature flights (also completed with the IRIS+), an average altitude of 30m was attained. Flight times were shortened by an average of 4 minutes due to the extra weight attached. In calm, early morning winds (when only the duplexed cable was utilized), flight times could be extended to upwards of 15 minutes, depending on battery life and wind gusts.

UAV Regulations

In order to legally fly UAVs for scientific research, a series of steps must be undertaken before a flight can be planned. The principle component of this process is the obtainment of a Certificate of Authorization (CoA) from the Federal Aviation Administration (FAA). To successfully obtain a CoA, a number of requirements must be met and documentation shown.

Additional regulations on UAV's are to be followed prior to implementing a flight plan. Among these are to file a Notice to all Airmen (NoTAM) to any airports nearby, at least 48hrs ahead of the experiment's first flight. During flight, the UAV altitude ceiling is 100m, so as to ensure redundancy in limiting any possible interference between the drone and other aircraft.

A final regulatory requirement at the time of this field study was that the individual flying the UAV, or pilot-in-command (PIC) was to have had, at the least, formal FAA ground school flight training and successful completion of the FAA ground school exam; as well as a class III medical certification, obtained from a certified physician. Additional spotters must have at least a class III medical certification, and at least one spotter is needed. For further information, the reader is encouraged to visit www.CTemps.org, or the FAA website www.faa.gov.

Field Deployment

DTS

Implementing our modified DTS set up in the field required the co-location of known measuring instrumentation to compare our experimental analysis to. For both field deployment locations, a Campbell Scientific Integrated CO₂/H₂O Open Path Gas Analyzer and 3D Sonic Anemometer was used to collect high temporal resolution temperature, humidity, and wind speed data that is typically used for Eddy Covariance flux calculations (“Campbell Scientific: IRGASON Integrated Gas Analyzer and Sonic Anemometer,” 2014). A single IRGASON system was deployed at 1.75m above ground, and oriented perpendicular to the prevailing wind direction in the valley of the site. Prevailing wind direction at Oxbow was determined to be coming primarily in from the West-by Southwest. Campbell Scientific’s CR3000 Measurement and Control System was used to run the IRGASON.

Figure 8 depicts a schematic of the drone-deployed temperature cables. The figure diagrams both cables being deployed. For flights after the first morning that didn’t require a humidity data gathering component, the wet bulb cable was detached from the drone.

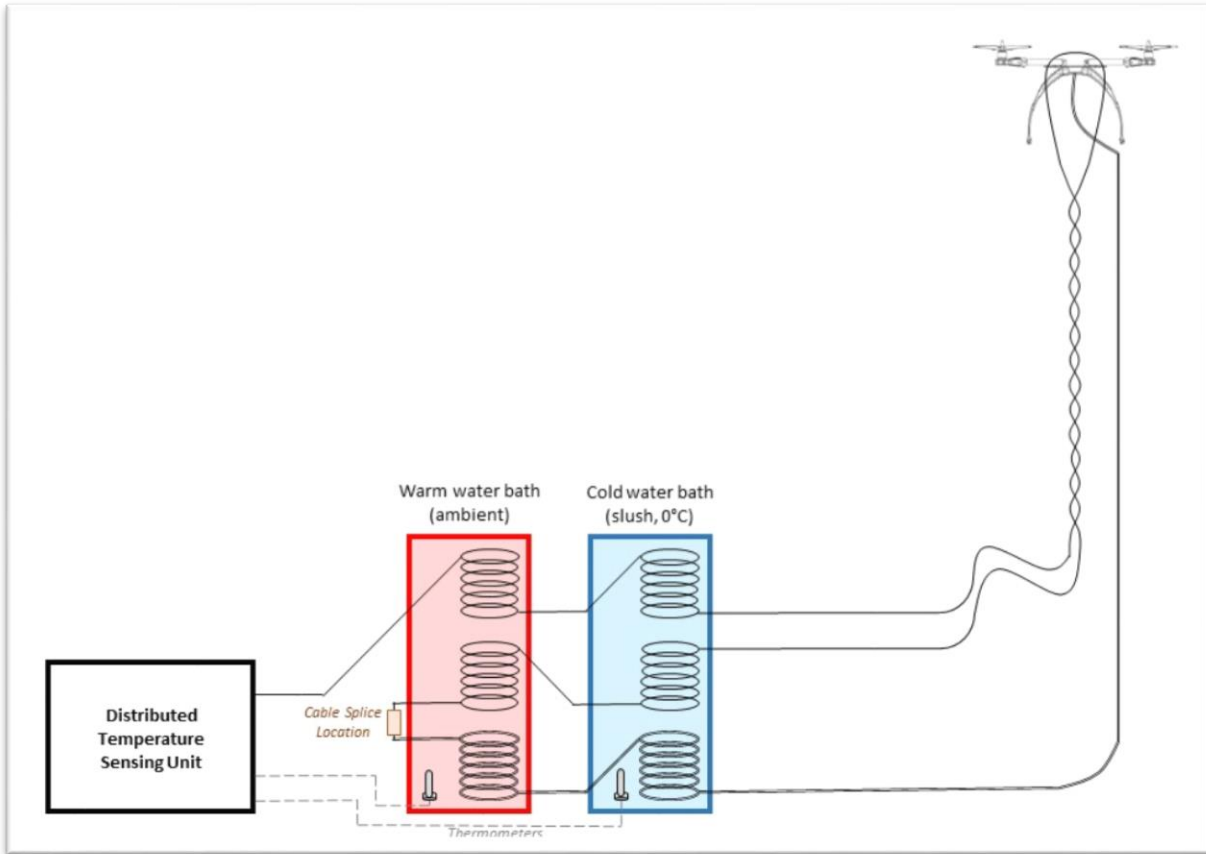


Figure 8: Diagrammatic description of the Oxbow field deployment with both air temperature and wet bulb temperature. The wet bulb section of the cable is spliced to the duplexed, dry bulb section of the cable. This allows for maximum temporal resolution.

The duplexed cable was un-braided at the midpoint of the measuring extent and fixed over the body of the drone. The terminal end of the wet bulb extent of the cable (spliced in-line with the dry temperature cable) was fixed to the bottom of the drone along the drone body's center of mass. Co-location of the cables in space was done via orienting common points of measurement from the body of the UAV down to ground level.

To mark the ground level with the cable, a field assistant held on to the cable with his or her hand on the ground. The cable's tensile strength and the UAV's stability proved to be enough to maintain enough tension throughout the cable to maintain a straight profile/

Results

Overview

Results displayed and discussed in this report were collected during the July field deployment to Oxbow Conservation Area. Of the available flights conducted during the study, 13 provided sufficient reliable data to analyze for feasibility in measuring temperature and calculating humidity, sensible heat flux and evaporative flux. All flux measurements were compared to Irgason-collected Eddy Covariance calculations. Temperature and specific humidity measurements showed a strong correlation to Irgason Tower data. Temperature correlation was expected, as DTS is a proven precise temperature measurement tool. Correlation between specific humidity values was a positive test result, as a fiber optic-based, dry bulb/wet bulb approach to measuring humidity has not, to the author's knowledge, been successfully conducted.

Correlation between sensible heat flux measurements and evaporative flux measurements proved less strong. Four of the 13 flights showed a strong correlation to Irgason-derived values at the same height. The other 9 flights were significantly different. As a result, evaporative flux measurements were similarly off. However, overall trends gleaned from the thirteen flights showed significant patterns in Bowen Ratio, sensible heat flux and evaporative flux values with respect to height off the ground and time of day.

Summary Data

A summary data table of key components to calculations is in table 2.

Table 2: Summary of Critical Data used for mean value calculations.

Flight	Iragson Data										DTS Data							
	UW (m/s)	VW (m/s)	Mean Horizontal Wind Speed (m/s)	Vertical Momentum Flux (m/s)	Sensible Heat, H (W/m ²)	Evaporative Flux, E (W/m ²)	Mean Temperature, T (K)	Specific Humidity, SH (g/kg)	B _{area}	σ _{r,area}	Specific Humidity, SH (g/kg)	Mean Temperature, T (K)	Sensible Heat, H (W/m ²)	Evaporative Flux, E (W/m ²)	B _{ons}	σ _{r,ons}	Time	Flight Duration (seconds)
36	-0.0027	-0.0033	0.6188	0.0648	48.1893	92.1345	291.3721	7.1594	0.5230	0.4925	7.9245	290.0549	56.9418	222.0710	0.2564	0.3330	7/20/15 8:30	221
37	0.0293	-0.0336	0.2471	0.2113	60.5143	164.0717	295.3543	7.4047	0.3688	0.5584	8.7465	294.4923	51.3347	68.5603	0.7488	0.3153	7/20/15 9:15	242
40	-0.0301	0.0123	1.0444	0.1804	93.0565	277.0551	297.5639	7.5288	0.3359	0.5949	9.0219	298.0258	40.4082	70.5686	0.5726	0.2710	7/20/15 9:55	132
41	-0.0275	-0.0061	0.3664	0.1679	119.6269	338.3048	299.2110	7.6899	0.3536	0.8914	8.3829	299.3667	26.0178	45.0314	0.5778	0.2033	7/20/15 10:09	90
42	-0.2002	-0.0564	3.8554	0.4560	92.8880	368.7974	300.3271	6.9430	0.2519	0.5090	6.4486	300.3809	30.6445	38.5557	0.7948	0.2278	7/20/15 11:15	124
43	-0.1708	-0.0298	4.3087	0.4164	91.1416	320.8011	300.0506	6.5665	0.2841	0.5684	6.0348	300.3166	59.9055	62.4959	0.9586	0.3556	7/20/15 14:20	249
47	-0.1241	0.0109	3.8585	0.3530	68.2391	325.3702	302.7482	5.6636	0.2097	0.6210	5.9221	303.4340	67.9750	114.7477	0.5924	0.3907	7/21/15 8:30	244
61	-0.0090	-0.0069	0.4512	0.1064	62.2080	108.0714	290.7857	5.7255	0.3756	0.4668	6.8613	290.0795	52.4948	194.4881	0.2699	0.3149	7/21/15 9:30	144
63	-0.0030	0.0007	0.9799	0.0556	72.0911	109.2860	295.7721	5.4842	0.6597	0.6728	6.7118	294.2926	43.1580	139.7689	0.3088	0.2805	7/21/15 9:39	99
64	-0.0380	0.0270	3.3162	0.2160	52.1319	173.7286	296.6301	4.6540	0.3001	0.5036	5.1362	295.9278	38.3620	82.0510	0.4675	0.2612	7/21/15 9:59	65
68	0.0082	0.0108	0.7730	0.1165	83.5604	237.7583	299.9673	4.9192	0.3515	0.6433	5.0715	299.1425	58.4433	73.2883	0.7974	0.3496	7/21/15 12:30	77
69	-0.0590	0.0671	0.1197	0.2989	47.5214	318.8156	300.6989	5.0367	0.1491	0.7082	5.4425	299.8854	26.2424	32.3890	0.8102	0.2051	7/21/15 13:11	175
71	0.0176	0.0490	1.9715	0.2282	51.5207	216.8967	301.4039	4.3219	0.2375	0.5717	4.2064	301.6093	22.8459	117.9894	0.1936	0.1883	7/21/15 13:55	62

Temperature and Humidity Analysis

Statistical Comparison of Irgason and DTS data

Initial experimental design was intended to field test the feasibility of recreating a sling psychrometer. Comparative data on temperature and specific humidity is shown in Figure 9.

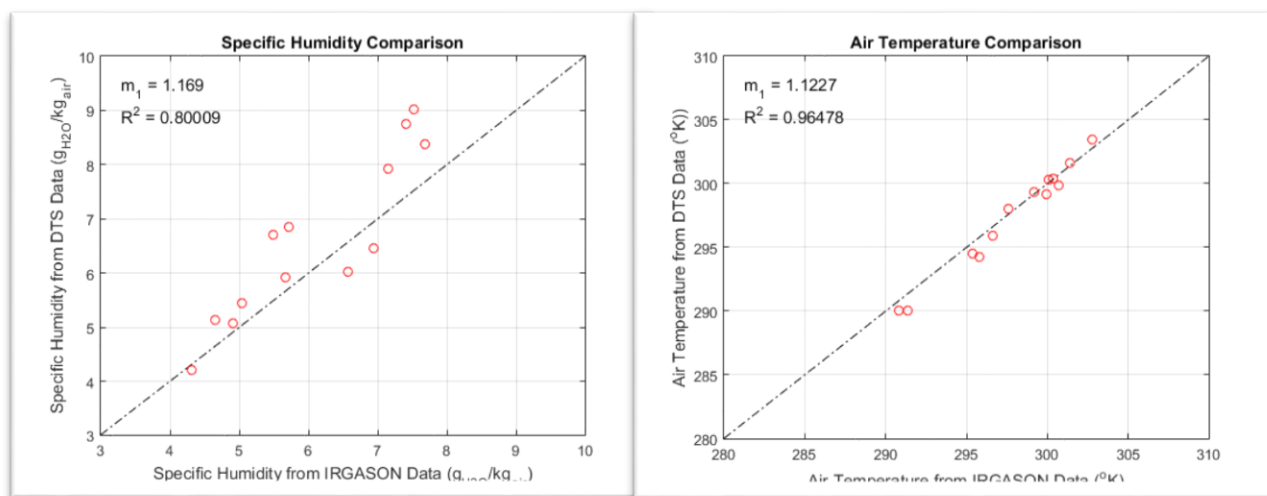


Figure 9: Specific humidity calculations, derived using equations (9), (10) and (15) show a strong correlation to calculated specific humidity from the Irgason data, without any correction being added to the DTS experimental data. As was expected, temperature values showed a very strong correlation. In these plots, m_1 refers to raw Bowen Ratio values.

The strong correlation in the absence of any correction factors was encouraging. Sufficient advection was a perceived plausible issue in the accuracy delivered by the DTS psychrometer configuration, however this problem seems to be of little consequence. Windspeed was considered a loose metric for minimum advective quantity. No correlation was found between mean vertical windspeed (momentum flux) and horizontal wind speed; and the difference in calculated specific humidity. However; given the strong correlation between the two calculated SH values, it is assumed that mean wind speed was sufficient to provide advective displacement of the diffused water leaving the wet bulb cable. Fluctuations in windspeed, particularly in flights where windspeed fluctuates over a threshold windspeed value (for example, Euser, et al claimed a 3m/s threshold would alter γ ; based off Allen, et al and equation (8) could

be observed, may be an indicator of relative effectiveness of the cable's accuracy compared to the Irgason's measurement.

Temperature and Humidity Profiles

Specific humidity correlation and temperature correlation were high when compared at the height of the Irgason (Figure 9). Temperature, as mentioned, is unsurprisingly well correlated, as it is an already proven instrument. The specific humidity correlation provides confidence that, to a sampling interval of 1Hz with a sampling rate of at least 1 minute, reasonably accurate humidity profiles can be derived. With these results, vapor pressure calculations used for humidity calculations and evaporative flux measurements can be attempted. As actual air vapor pressure, derived from saturation vapor pressure of the wet and dry bulb thermometer outputs, is a foundational step in calculating the Bowen Ratio and therefore evaporative flux. Irgason specific humidity calculations are done independent of the instruments evaporative flux, whereas DTS evaporative flux depends on the same set of information to calculate both specific humidity and evaporative flux. Therefore, comparing specific humidity values of both instruments provides an independent metric for testing the accuracy and precision of vapor pressure values.

Plots of vertical profiles show vertical shifts of temperature and humidity. Figure 10 illustrates a typical example of vertical temperature and humidity profiles. This sampling was

taken during an early afternoon flight (~2:20 pm). The sampling interval over this flight was approximately 4 minutes. Appendix A has the profile plots of all thirteen flights.

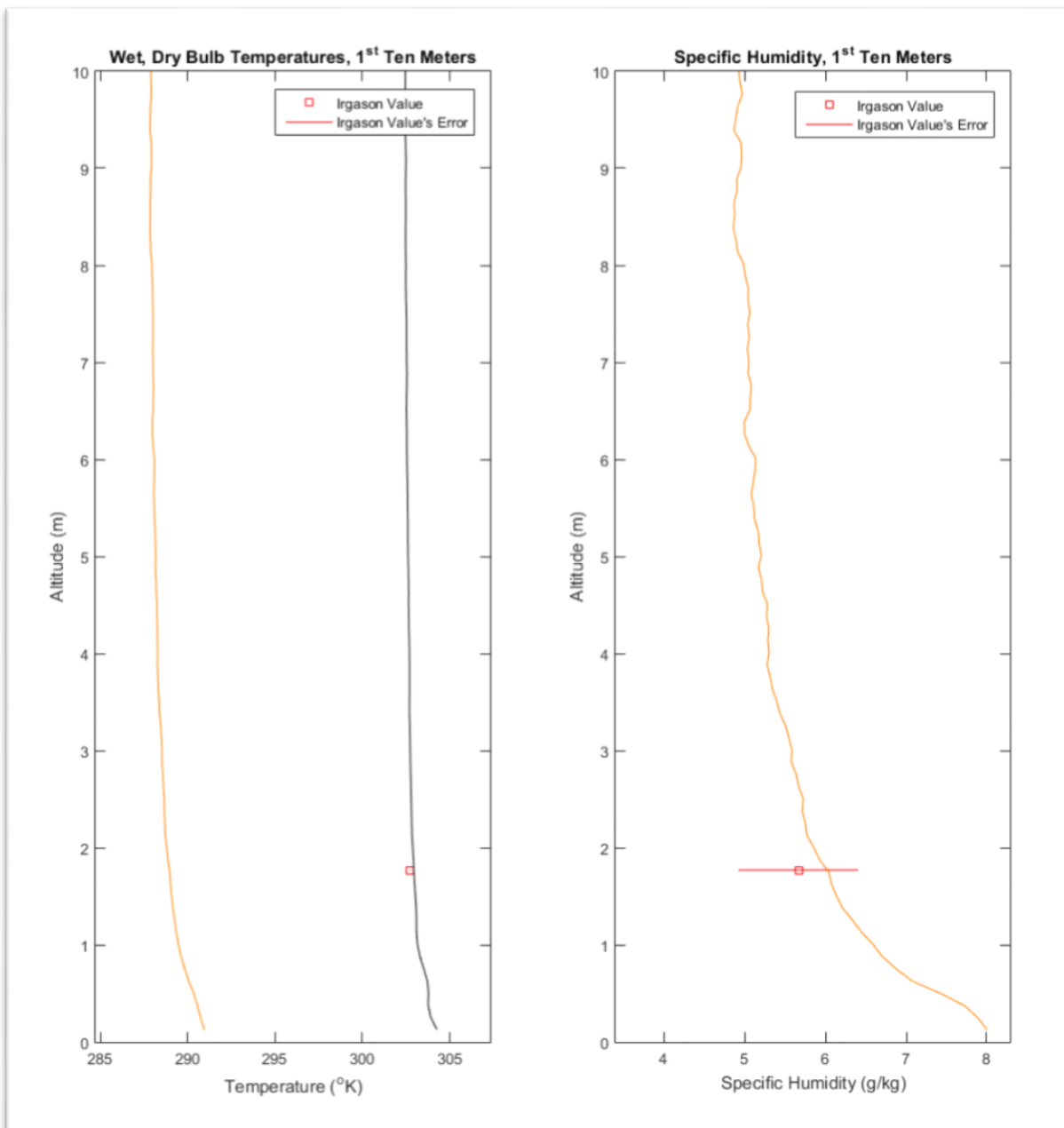


Figure 10: Example vertical profile of wet bulb (yellow), dry bulb (black) temperature vs Irgason air temperature (left side), and specific humidity values. Range bar on the specific humidity profile is calculated as the variance in the specific humidity over the duration of the flight. See appendix A for all vertical profiles. (Flight 43, July 20th, 2015; 14:20)

Bowen Ratio Analysis

There were, in all 13 flights, a characteristic pattern that appeared in the vertical profiles of our data when air temperature and actual vapor pressure were calculated. Figure 11 displays the general phases observed.

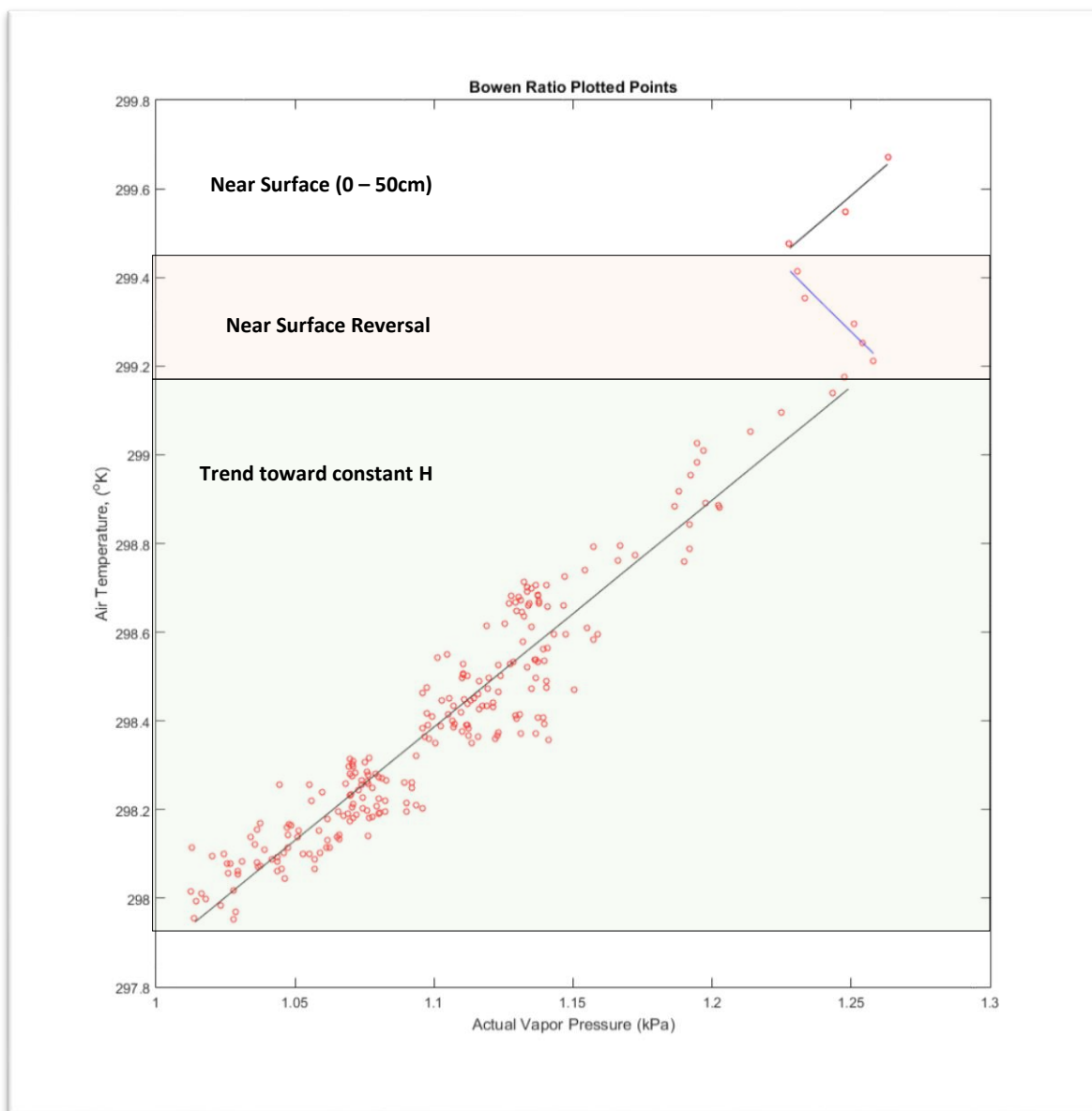


Figure 11: Example of typical sections seen in plots of Bowen Ratio values.

In the Bowen Ratio plots, note that data closest to ground level begin at the top. Moving down and to the left in these plots corresponds, to an increase in altitude. The Reversal value

indicated in Figure 11 indicate a recurring pattern slightly above the ground whereby a temporary increase in vapor pressure corresponds to an increase in temperature before returning to the more familiar, stable trend.

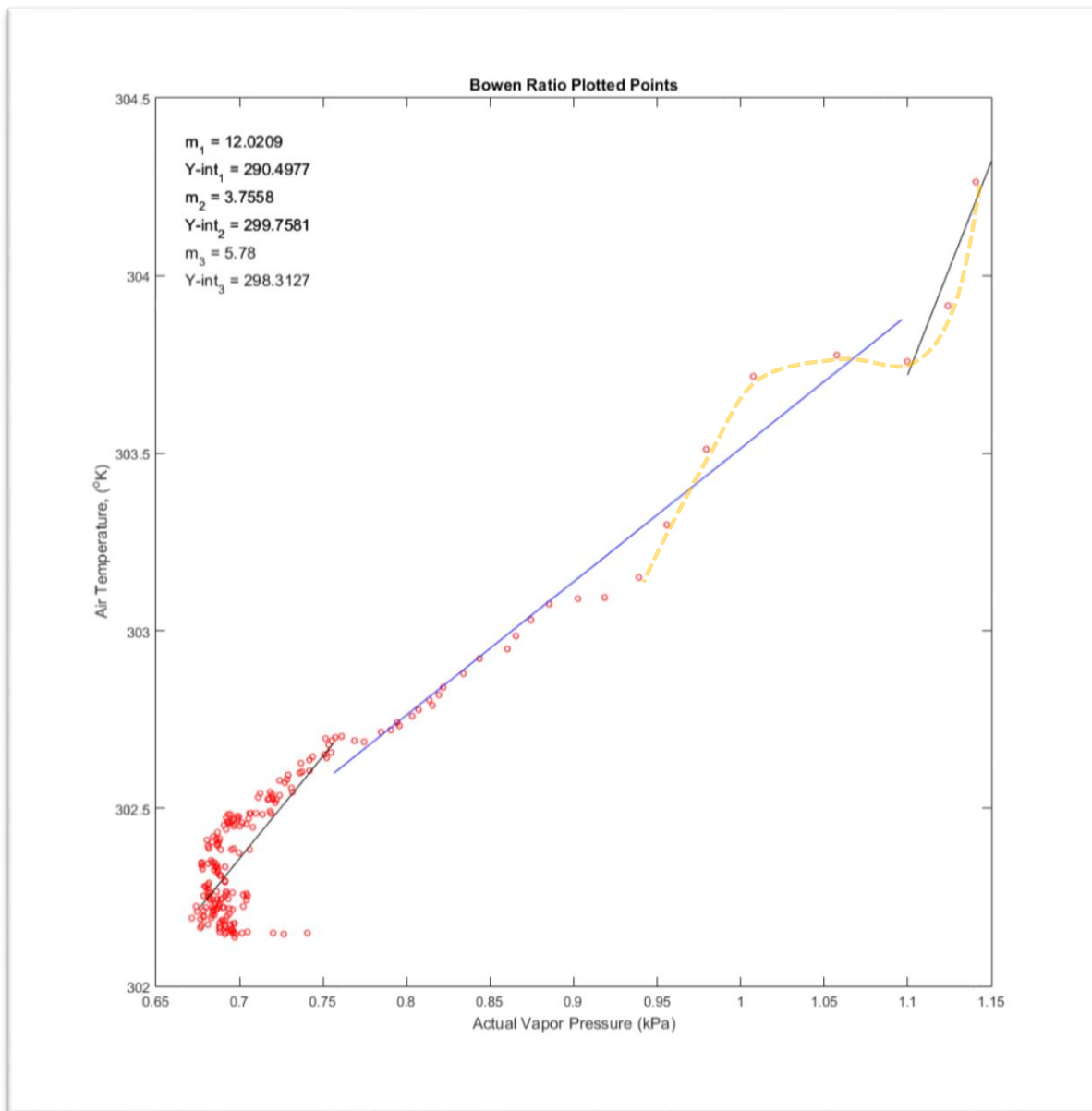


Figure 12: Example plots of Calculated Bowen Ratio Values and the linear fits approximated from data collected during Flight 47, at 8:25 in the morning of July 20th.

This dissection varied mildly with height depending on the flight, and in the skew at the surface and near surface reversal. In cases, such as in Figure 12, the shift in Bowen Ratio sign was significant. In other flights – flight 36 for example (see Figure 12, yellow, dashed line) – a subtle

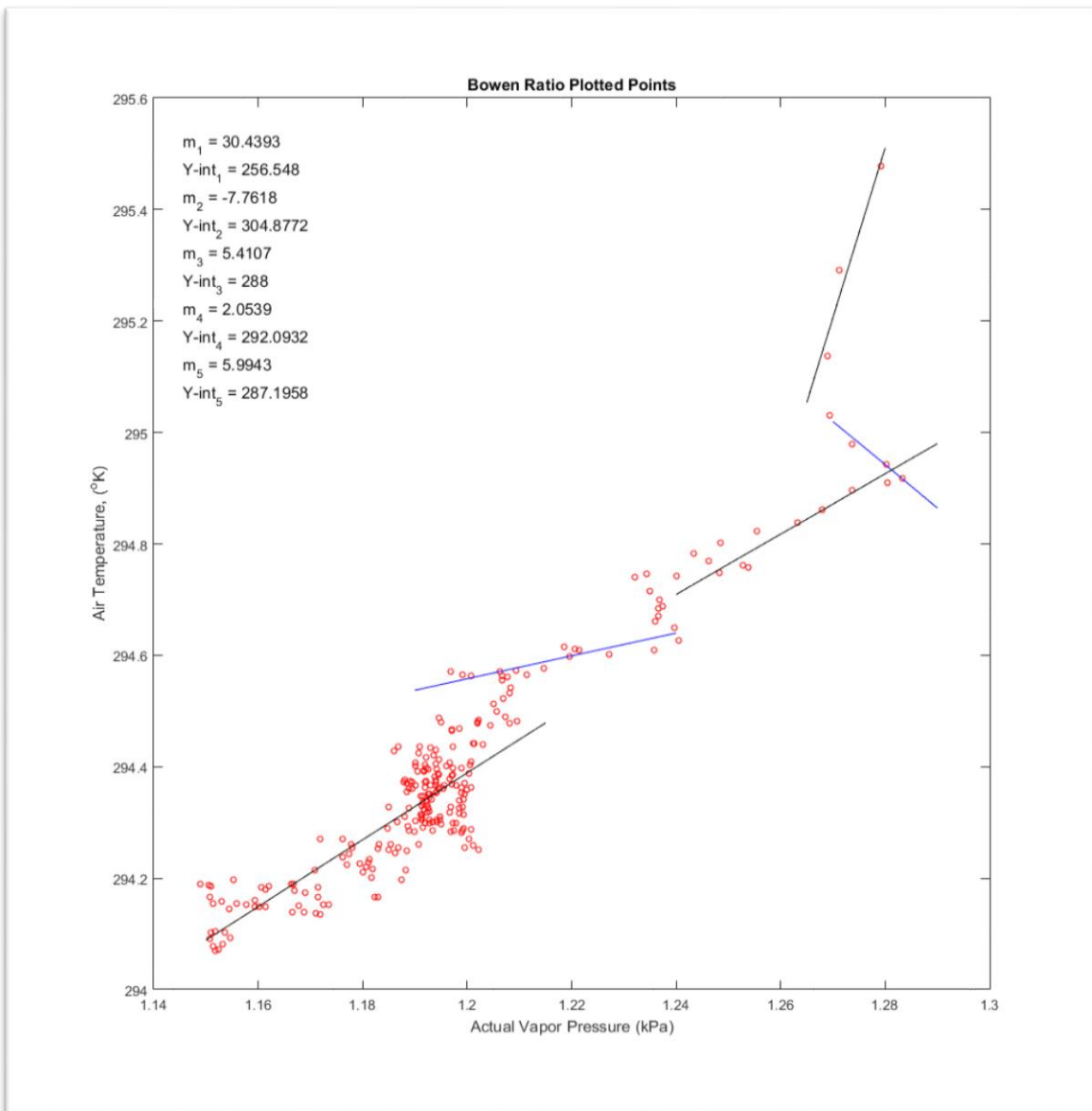


Figure 13: Another characteristic example of Bowen Ratio plots with linear fits to section of data. Flight 37, 7/20/2015, 09:15.

'S' shape was prevalent, but considered too weak to be separated. Contrastingly, some flights showed a series of significant reverses in trend that additional Bowen Ratios were determined (Figure 13).

Figures 12 and 13 show two characteristic profiles of plotted Bowen Ratio values. More specifically, these plots are of the ratio between dry air temperature and the actual vapor

pressure, e_a , derived during each flight. Each red dot is a time average value at a height, z . Bowen Ratios were obtained by fitting appropriate sections of each plot with a linear fit and extracting the slope of that section of the profile out. This slope value, multiplied by γ , was the final derived Bowen Ratio.

As can be seen in Figure 10, on the right-hand plot, and in Figure 13, there was a distinct reversal of trend. This was a common, if not always significant recurrence. The negative value here does indicate a loss of sensible heat energy locally, which was not an expected trend to see.

Comparing DTS-Derived Bowen Ratio values to Irgason Bowen Ratio Values

Figure 14 shows a comparative plot between Bowen Ratio values. The comparison plot itself shows no real correlation between the two methods. However, it is important to note that, in all cases (all 13 flights) the calculated Bowen Ratios were less than one, indicating a dominance

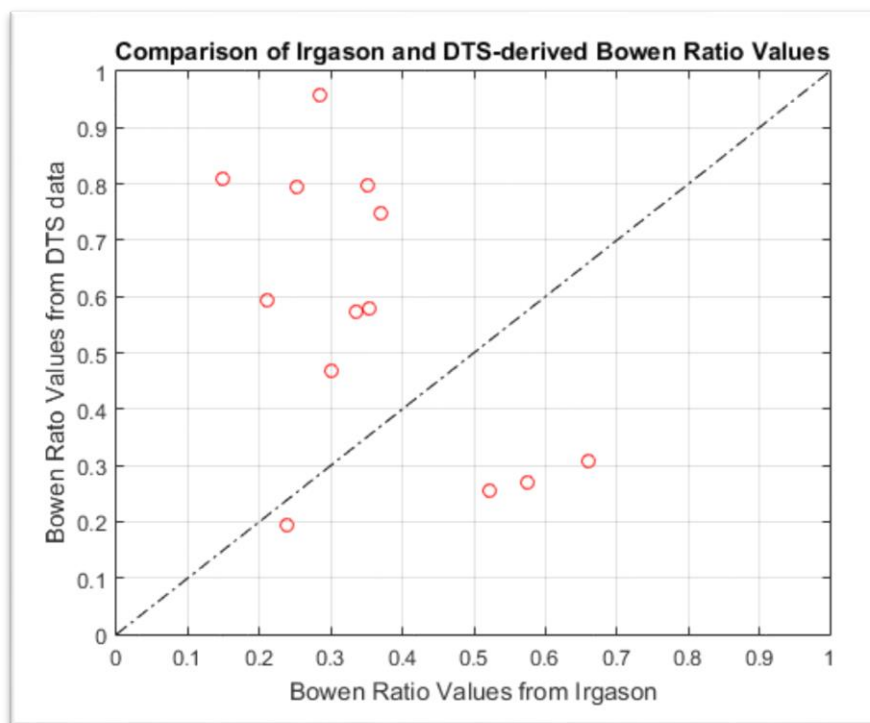


Figure 14: Comparison plot of calculated Bowen Ratio values. Importantly, All values are indicative of one common trend: Latent heat is dominating sensible heat, indicating evapotranspiration is occurring.

of latent heat energy relative to sensible heat energy. When looking at flux profiles, this relationship holds.

Sensible and Evaporative Flux Values

Comparing Profile Data to Irgason Data

Figures 15 and 16 show two examples of significant correlation between Irgason and DTS-derived sensible heat flux values at the height of the Irgason (~1.75m). Figure 14 also shows a

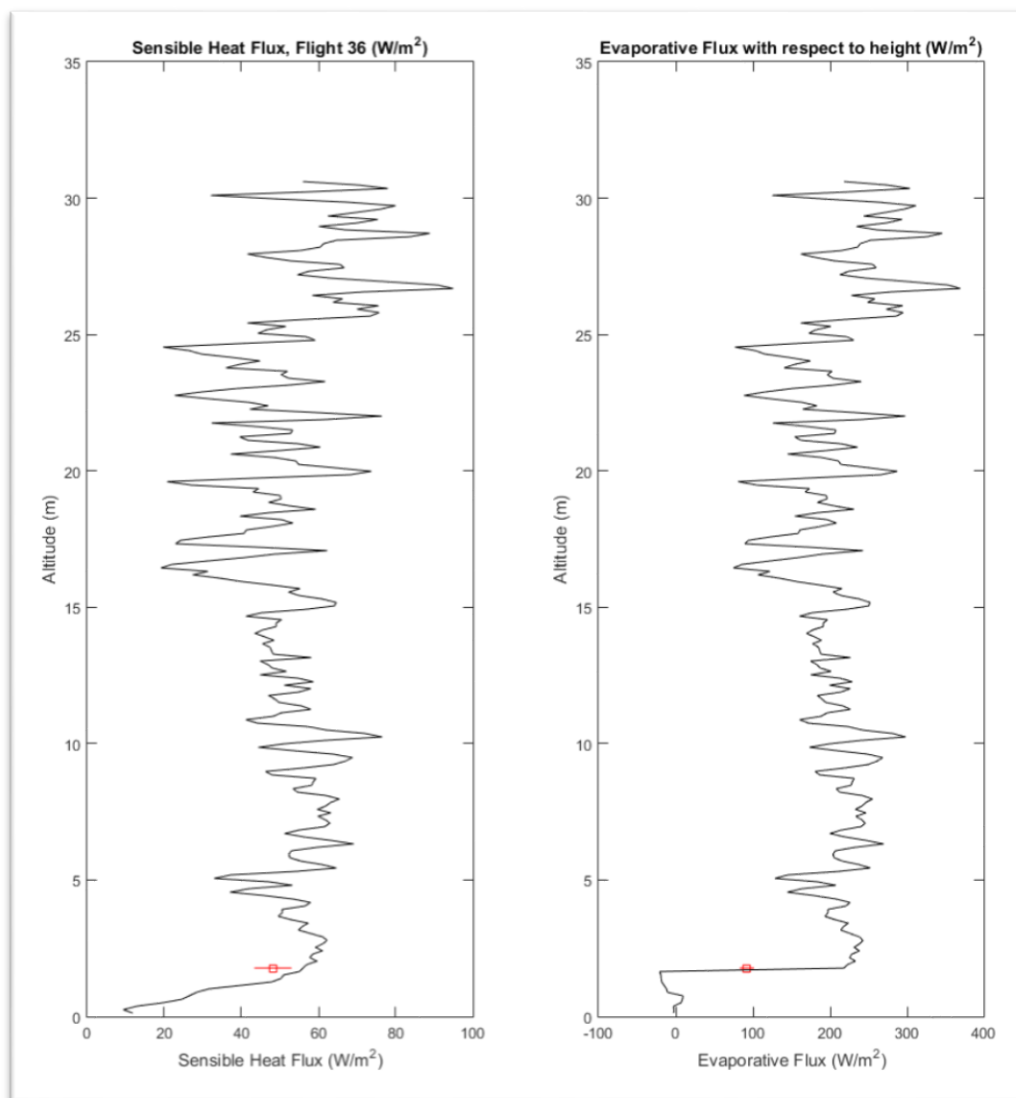


Figure 15: Comparison between H and E fluxes calculated at the Irgason (red point) and the full vertical profile of fluxes calculated from the DTS data. Flight 36; 7/20/2015, 08:30.

correlation between the two calculated evaporative flux values, though this correlation was less common in other samples (Appendix C). Red squares in the plots indicate the value obtained from the Irgason at 1.75m height. Red Range bars across the average Irgason value in the evaporative flux plot represent the variance in evaporative flux over the entire duration of the flight. Red range bars in the sensible heat flux plot indicate a researched maximum sensible heat

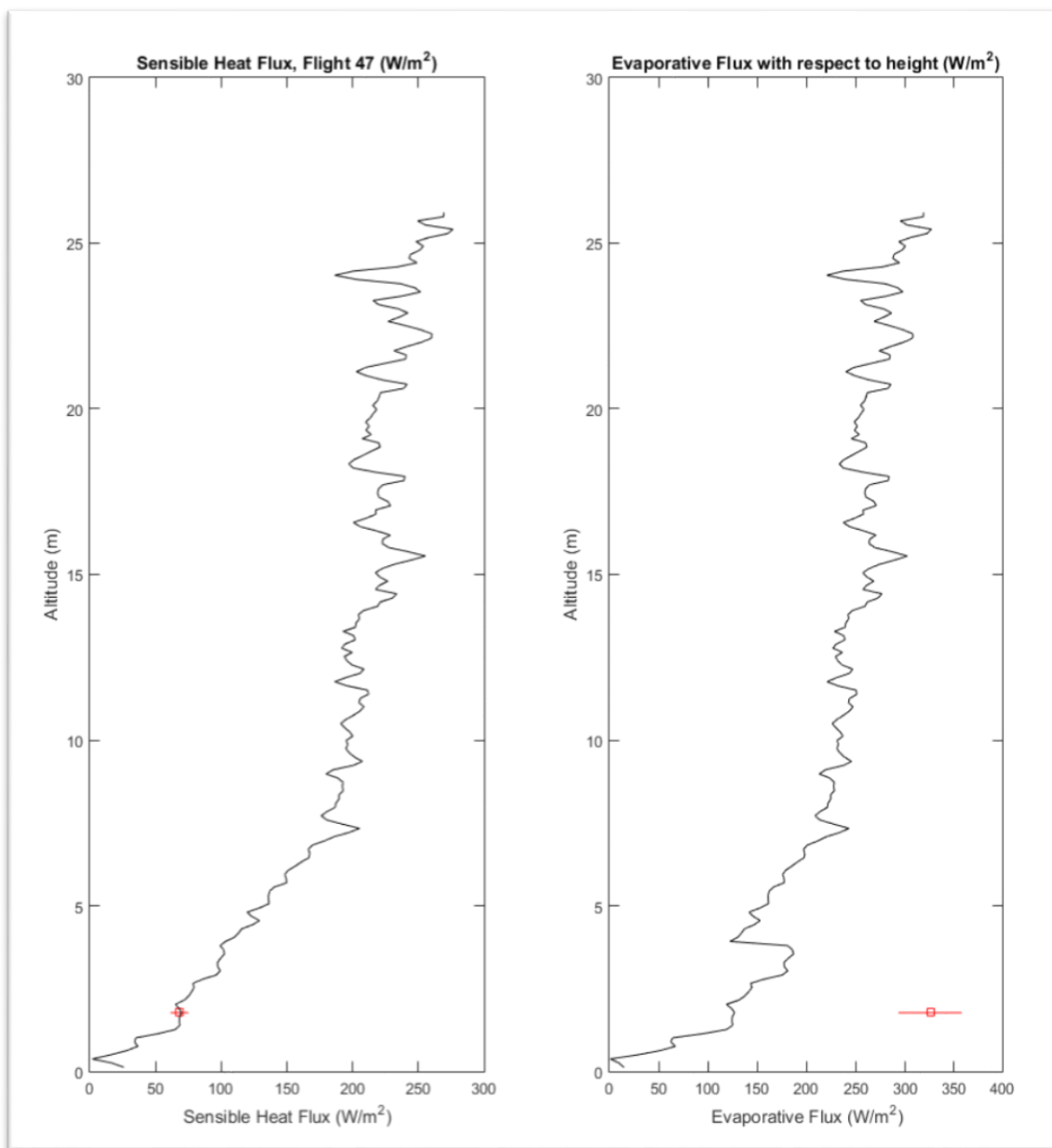


Figure 16: Sensible heat values track strongly at height. Evaporative flux values at height are off, but at 15-25 meters, the DTS-derived values do gain toward Irgason values. Flight 47; 7/21/2015, 08:30

flux error of 10% (Salesky et al., 2012).

The sharp increase in Evaporative flux at the Irgason height – coinciding with strong correlation – is due to the shift in the Bowen Ratio calculation at that height (see equation (5)).

For sampling flights that did not match with Irgason derived data, there are still strong patterns to be seen, despite the lack of strong spatial correlation. Figure 17 shows an example of

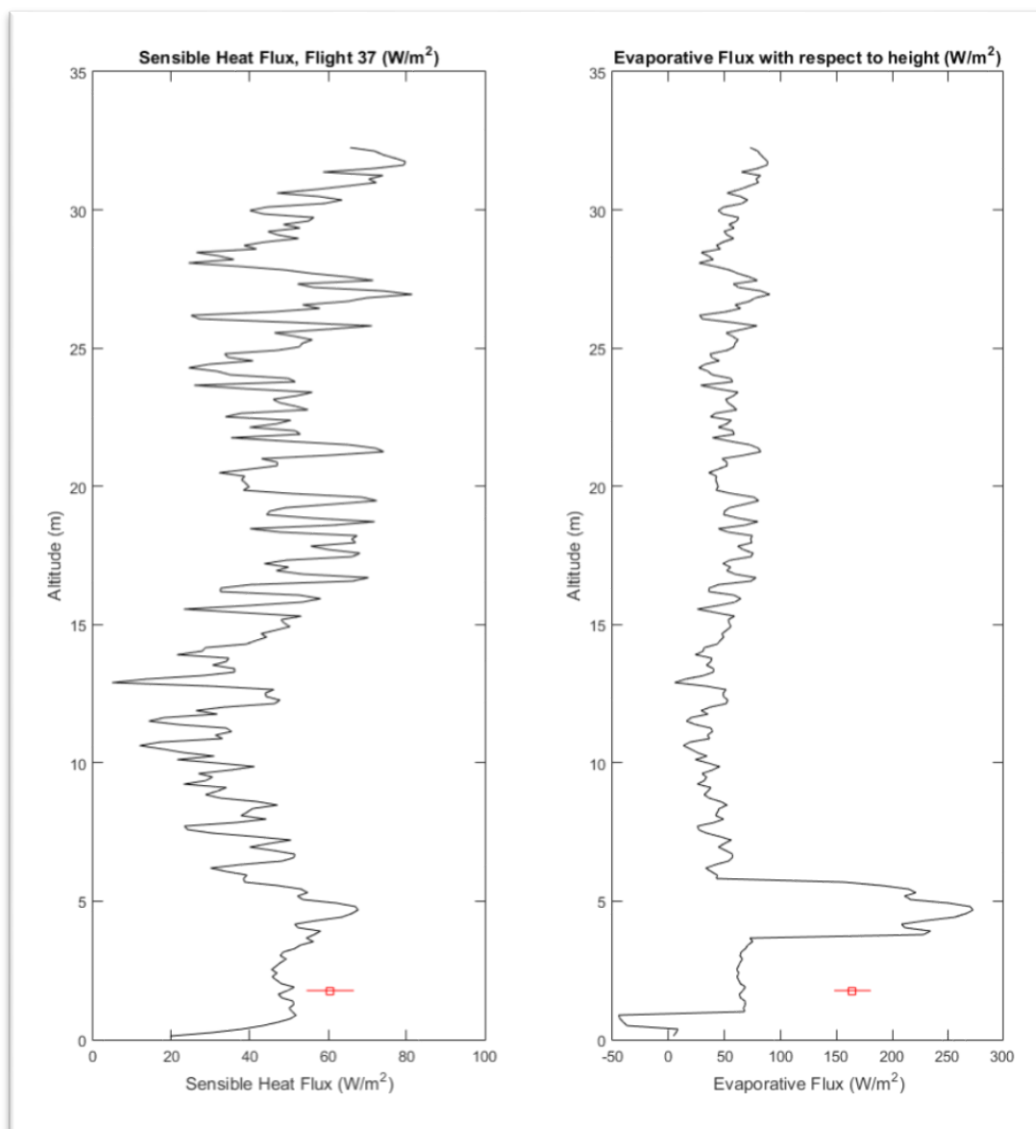


Figure 17: Flight showing reasonable profiles, but uncorrelated with Irgason data. Note the effect of Bowen Ratio Fluxes on the data set. Flight 37; 7/20/15, 09:15.

a flight with reasonable sensible and latent heat flux profiles that do not match directly with Irgason-derived data.

Of note within Figure 17 is, again, the sharp increase in evaporative flux at around 5 m. This corresponds to a momentary drop in derived Bowen Ratio values, which would in turn lead to an increase in evaporative flux along that portion of the profile. The ratio drops from approximately 6 down to 3 for the profile range seen, then returns to 6 again. For further comparisons, see Appendix D.

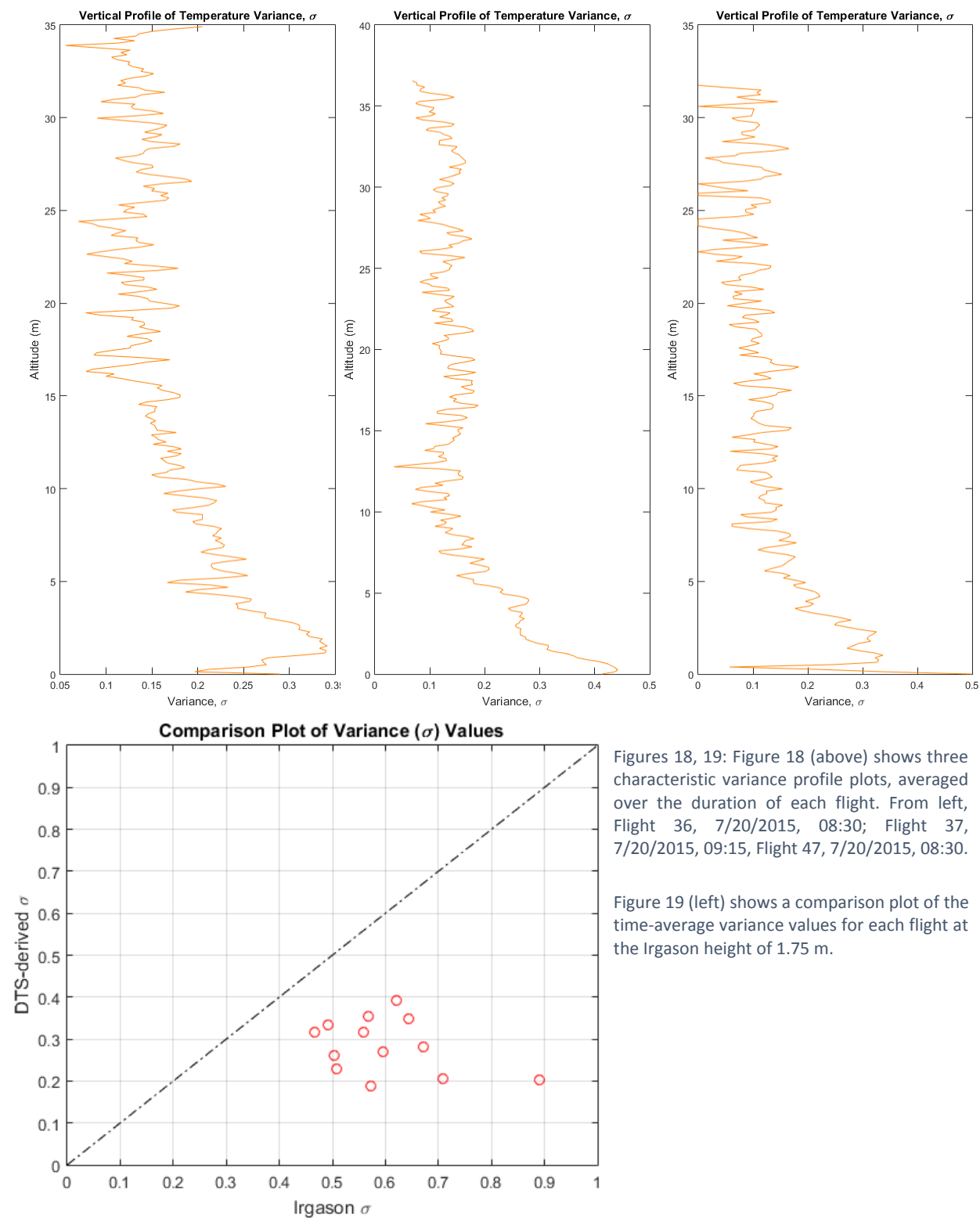
Variance

Figures 14 – 17 have embedded in their calculation the vertical variance of temperature (see equation (19)). Figure 18 shows three characteristic morning variance profiles. Appendix C has the full set of variance profiles.

There is a common trend toward small variances at higher altitudes. Careful review of equation (19) shows that this reduction in variance can, in these cases, prove to offset the increase in height, z . The result of this reduction in variance with corresponding increase in height can be seen particularly well when reviewed with the evaporative flux plot in Figure 17. This plot is from the same flight (Flight 37) as the middle plot in Figure 18. Here the variance offset results in a relatively constant flux with height, starting at around 6m off the ground. Afternoon flights showed largely similar trends in variance with respect to altitude.

Despite this correlation, the trend in variance values calculated via the DTS data were consistently lower than variance values obtained from the Irgason (Figure 19). One reason behind

this might be in how dry air temperature was obtained; via duplexed temperature profiling. This will be discussed further later on. In short, variance calculations may be better than what would be expected when creating equation (19) to determine evaporative flux.



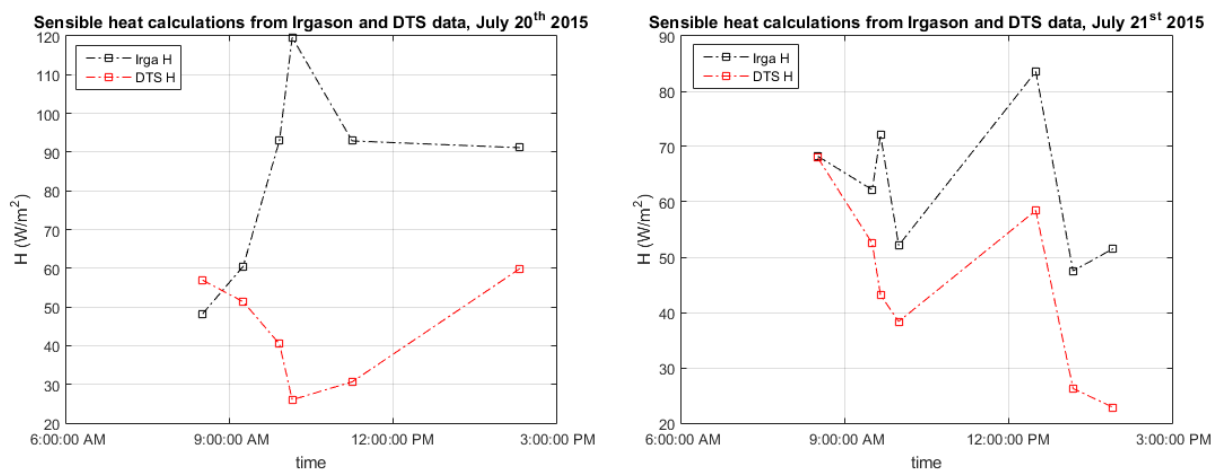
Figures 18, 19: Figure 18 (above) shows three characteristic variance profile plots, averaged over the duration of each flight. From left, Flight 36, 7/20/2015, 08:30; Flight 37, 7/20/2015, 09:15; Flight 47, 7/20/2015, 08:30.

Figure 19 (left) shows a comparison plot of the time-average variance values for each flight at the Irgason height of 1.75 m.

Variance values were mostly higher closer to the ground than at higher altitudes, until values began to level off, indicating an increase in total heat energy closer to the ground, a reasonable assumption.

Results Recap

With the sum of data presented, it is reasonable to say that a DTS-based approach to capturing data necessary for high resolution sensible and latent heat flux data is feasible. There are noticeable differences in calculated vertical temperature variance values (Figure 20) and therefore in sensible heat values. Again, looking at (16) and Figure 20, it is logical to then say that sensible heat values will also be relatively low. However, the DTS-derived sensible heat data, while perhaps not precise, does track with sensible heat values obtained through the Irgason. Further, DTS and Irgason sensible heat values track with time of day.



The largest issue to address is the systemic under-estimation of temperature variance calculations used as a surrogate for windspeed. Spectral analysis of the DTS data, when compared with Irgason data, shows the potential to correct the variance values obtained from the DTS. With

a more precisely calculated variance calculation, sensible heat and evaporative flux calculations will improve.

There is a noticeable increase in plot 'noise' when moving from initial plots of temperature and specific humidity. This is an artifact of, among other things, the variability noticed in Bowen Ratio values observed with respect to altitude. Bowen Ratio's, to the author's knowledge, have only once been observed in this fashion (see (Euser et al., 2014) for another example). This is a novel, new approach to calculating Bowen Ratio values. A result of this approach is an increase in numeric variability in inputs to sensible heat calculations. These flight-dependent variations in Bowen Ratio's combined with the induced variability in sensible heat calculations from variance profile predictions being continuously underestimated results in an output that is significantly more variable than a temperature profile averaged over the same time period. This isn't a sign of a system not working properly however, but rather an indication that more than merely temperature affects the profiles of evaporative flux. Indeed, these data sets are an enlightening first step into determining the complexity of this system. An initial outset being to further the knowledge of, plainly, how much water is leaving a homogeneous system seems an achievable goal.

Discussion: Positives, Shortcomings, and Moving Forward

Feasibility of DTS as a Humidity Measuring Device

The Oxbow Conservation Area field study has proven that, with careful and diligent modification of a small-diameter fiber optic cables, accurate, precise values of humidity can be measured in the lower atmosphere. Evidence also shows that short sampling periods of as little as 90 seconds (Appendix A: Flight 41, 7/21/2015, 9:59 am), can provide a sufficient number of sampling periods to measure specific humidity to the same level of reliability provided by Irgason set up. More than half of the flights conducted provided data sufficient to calculate specific humidity within the Irgason's margin of error.

Another positive outcome from the humidity data analysis proved that 3M vent tape modification was reusable. Field modifications were not needed during the deployment. The modified cable was stored in a water bath overnight on July 19th and 20th, meaning it was continuously wetted for approximately 72 hours consecutively, with only the brief flight time durations to dry out.

The feasibility and reliability of utilizing UAV's for fiber optic cable deployment proved mixed. While repeatability and flexibility of deployment were undeniable, flight duration proved to be a significant hindrance to collecting sufficient amounts of data over time. Initial comparisons of spectral analysis from Irgason and DTS data showed – surprisingly – that long-term data was the limiting factor on precise variance calculations.

Isolated discrepancies in the data were noticed in some flights. Figure 21 shows a full color plot of the duration of a sample flight. In the figure, horizontal streaks in the data – above the plot’s background temperature (note: not ambient temperature, as the entire plot is reflective of the wet bulb measurement) are noticed. These streaks are rare, but are the result of a minor defect - likely an unsaturated portion of the cable - in the tape along the cable. The larger profiles however, are considered robust enough to be trustworthy.

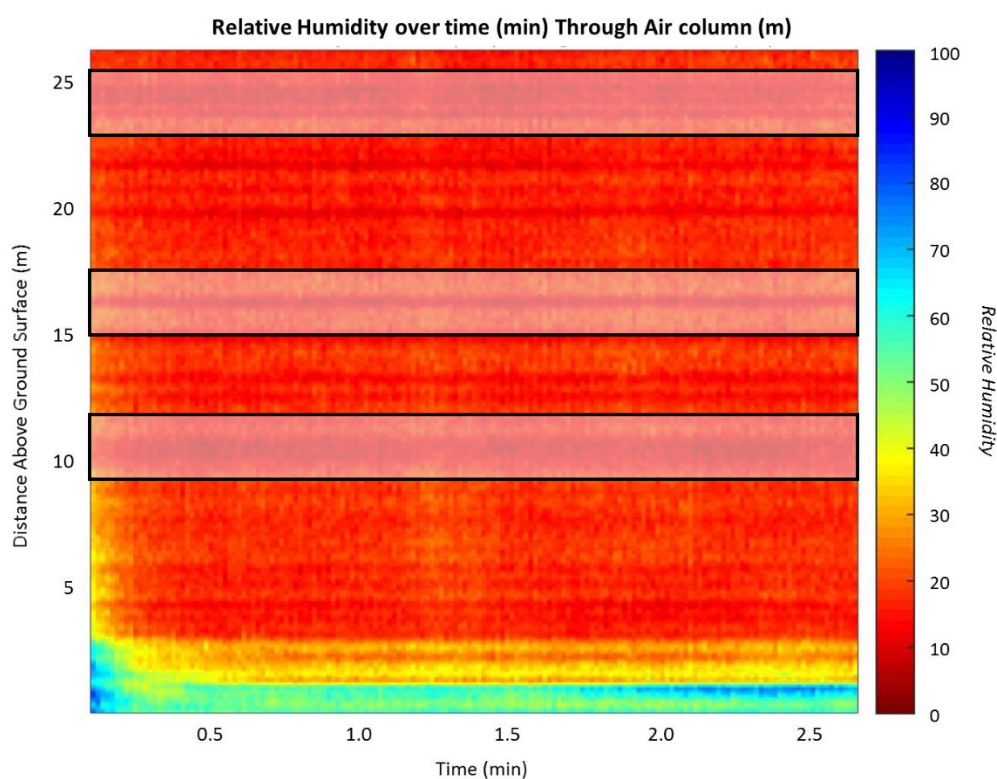


Figure 21: Preliminary analysis of the Oxbow data, Flight 50 (not used for analysis). The highlighted areas are where defects in the wet bulb temperature caused fluctuations in data.

Because repeatability of the deployment of the tape via UAV was proven to be plausible, duration of the instrument deployment became the limiting factor. UAV’s, while flexible (one can measure anywhere a DTS system can be safely deployed and it is safe to fly), can only fly for short periods of time. Further limiting the duration was the saturation wetting period of the tape. The

13 flights' data used for this analysis did not have this problem. Usable data periods of up to four minutes were collected, meaning the UAV was airborne for up to 8 minutes (90-120 seconds to ascent to altitude and stabilize, and another 90 seconds to descend from hovering altitude). However, longer duration flights, did experience a gradual drying of the wet bulb cable from the drone down. Therefore, if short duration measurements are all that are needed, this new approach is a feasible method, but if longer duration measurements are required, a new method of cable deployment or a drone with much longer flight durations should be considered.

Further analysis on the properties of the tape might also contribute to closing the gap between measured specific humidity of reliable methods and the tested approach. The initial justification for using this type of tape, instead of other approaches, was that it was proven to maintain its adhesiveness when wet, it was porous (analogous to a leaf structure with open stomata), and it wasn't too resistive to water vapor dissipation; meaning water could more readily be wicked away from it than from a cotton ball. The latter justification was an important consideration when comparing the application of a sling psychrometer to an environment where windspeed could be a limiting factor. If the analogous 'cotton' part of the wet bulb thermometer could more easily wick away water, then correct temperature via evaporative cooling of the tape would be attainable.

One slight improvement on tape-based modification to the cable would be roll a section of tape around the cable instead of folding it. Folding the tape provided stability, but created an uneven surface area that acted at times as a small wind sail. In calmer conditions (like those

analyzed here; horizontal wind speeds near the ground never getting above 5 m/s) this problem is mitigated. Regardless of wind speed however, this physical issue should be vetted further.

Other cable modifications were attempted, but repeatable, reliable and comparable data for analysis was not available. The larger, more powerful Matrix UAV proved robust enough to carry a fully saturated fiber optic cable like that shown in Figure 7a and 7b, to a height of 70m for approximately 15 minutes. Therefore, it was proven that a deployment of these cable types was possible and longer saturation periods could possibly be attainable. However, the positives of utilizing a UAV instead of a short tower must still be weighed.

The Implementation of UAV's for Broader Atmospheric Sensing

The implementation of UAV's has, in the last ten years, proven to be a major boon in the field of lower atmospheric sensing and remote sensing. This field experiment only added to the considerable lexicon of UAV-based research. However, the UAV approach did have shortcomings, in addition to the one mentioned in the previous section.

The UAV used for this flight proved to have unreliable vertical resolution for measuring its altitude accurately. This proved to be a hindrance, resulting in the loss of entire flights worth of data due to severely fluctuating altitudes. It is plausible that altitude problems were a result of the mass of the cable being lifted to 40 m was approximately equal to the payload capacity of the drone. This problem, however, was observed in many flights with only the duplexed, dry cable, and also during test flights with no payload. GPS modifications can be made to the IRIS+ to aid with fixing this problem, but even under the best of circumstances, vertical resolution is no greater than 2.0 m. Modern, RTK-level-accuracy gps units are available for integration into newer,

more robust drone platforms. This will significantly improve the telemetry precision problem in the future.

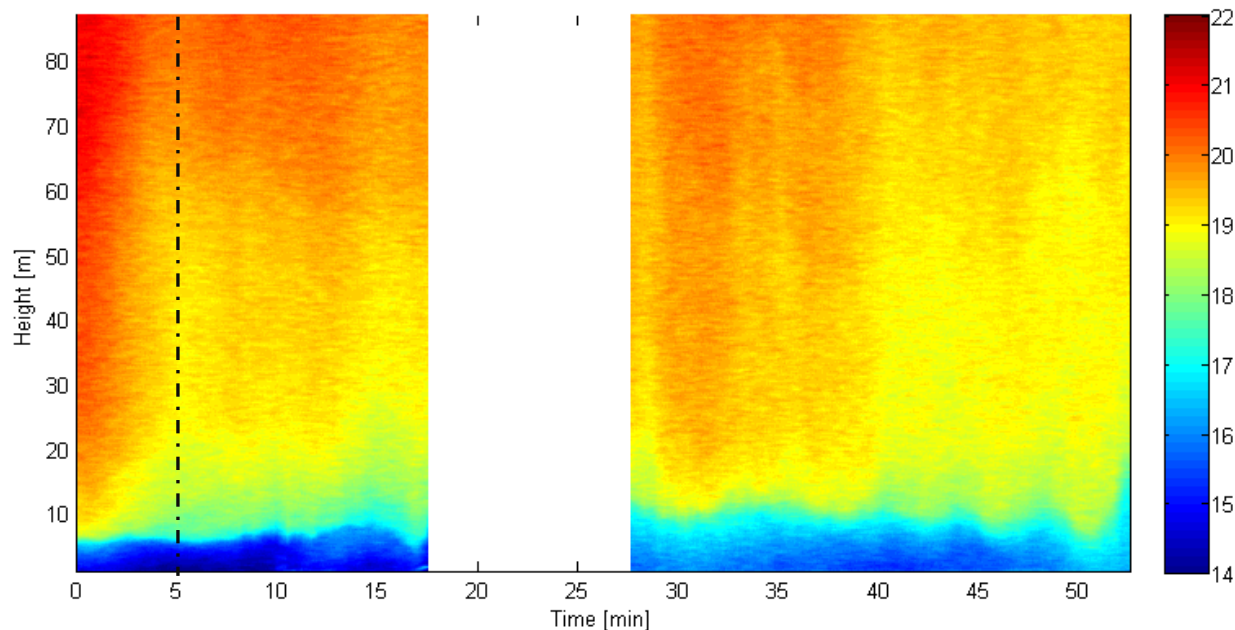


Figure 22: Two flights plotted together to show the initial degradation of the evening surface layer. The increase of periodicity along the top of the blue (colder) section of air is the development of the K-M wave (Temperature is in °C). Data collected during a summer, 2014 field deployment in Hermiston, OR.

Obtaining Certificates of Authorization and the requisite formal training needed to legally and safely fly drones is getting easier and more accessible. At the time of this experiment – though only one year ago – it would be more difficult to obtain needed credentials and paperwork to complete flight plans. For the direct application of DTS with drones, the concept is surprisingly pragmatic. Vertical profiles of humidity and energy fluxes are critical components of the energy balance of a hydrologic system. With increased altitude, flight duration, and lift capacity, more complex mechanical processes regarding morning and evening ABL transitions can be mapped. Figure 22 shows an example of a phenomenon in atmospheric boundary layer meteorology called Kelvin-Helmholtz waves (K-M waves).

The development of K-M waves along the layer between two different-density air parcels indicated the introduction of an advected, shearing force significantly contributing to the initial instability of the surface layer. Traditionally, it is thought that buoyant forces, created through re-radiated longwave radiation off the Earth's surface, acts as the catalyst (Stull, 1988). Warm air heating and expanding under cold air convects, catalyzing mixing. As the radiated heat increases, so does the buoyant-driven mixing. Figure 22 shows there is more to this explanation. DTS and UAV's proved to be a (relatively) low cost alternative to expensive LIDAR methods designed to capture similar data. Furthermore, LIDAR approaches usually ignore the bottom 30 – 100 m of the air, DTS implementation has proven that there is more going on directly above the ground; mechanical properties that have only sparsely been measured at the spatial and temporal resolution DTS can provide.

Response Times, Sampling Rates and Variance

DTS and Fiber Optic Cable Technology

Moving beyond humidity and temperature profiles proved less reliable, though data collected is reasonable, if not yet precise. A few considerations are worth implementing for future deployments of this design, and the ideal is a way to increase sampling rates of the DTS.

The Silixa Ultima DTS used in this experiment provided researchers with the fastest currently available sampling rate of any DTS on the market. However, it is reasonable to assume future improvements beyond the 1Hz limit are feasible. DTS systems are programmed and configured under the assumption that multiple kilometers of fiber optic cable will be used. This necessarily means an initial, substantial number of photons must be beamed through the cable

in order to create sufficient a number of Raman backscattered light. The result of this means the sampling of Raman backscattered light is slowed in order to account for the relatively high numbers of Raman backscatter at the beginning of the cable (note Figure 2, the downward slope is a result of a reduced number of Stokes and Anti-Stokes values as a function of distance from the DTS sensor). Because, for lower atmospheric sensing, only 100-200 meters of cable are needed; or 300-400 for a humidity measuring setup analogous to the one implemented in this study (see Figure 1). Reducing the initial photon energy may provide the ability to sample backscattered light at a higher rate. This higher rate may then allow for a better variance calculation; the critical component to calculating sensible heat using the Tillman approach.

Before this complex modification should be considered, a closer look into the temperature response rate of the cables must be considered. A sling psychrometer must be spun for approximately one minute before an accurate relative humidity value can be calculated, and in our study, one flight of as short as 90 seconds provided significantly accurate temperature and specific humidity calculations. However, for flux measurements to work well, longer sampling intervals combined with shorter sampling rates must be obtained. By comparison to the DTS, an Irgason can sample at 5 – 10Hz, the minimum required sampling rate of vertical humidity fluxes (“Campbell Scientific: IRGASON Integrated Gas Analyzer and Sonic Anemometer,” 2014). Therefore, further study on closing this gap should be conducted. Data similar to that collected in this field study may provide sufficient information to do so, but more precise field set ups (multiple Irgason’s in closer proximity to a fiber optic cable for example) must be configured. To the author’s knowledge, a 90 second sampling interval with this approach to calculating humidity

is the fastest quantifiable response time that provided significant results, indicating a promising new direction for this method in the near future.

Variance Analysis

Further technical issues with collecting temperature information for variance calculations follow this subsection. This section covers the mathematical approach to improving temperature variance calculations; spectral correction.

As has been mentioned, the variance calculations done with the dataset retrieved are the biggest issue that must be resolved. An additional analytical step was completed to attempt to reconcile the gap in the Irgason's reported variance and the temperature variance derived from

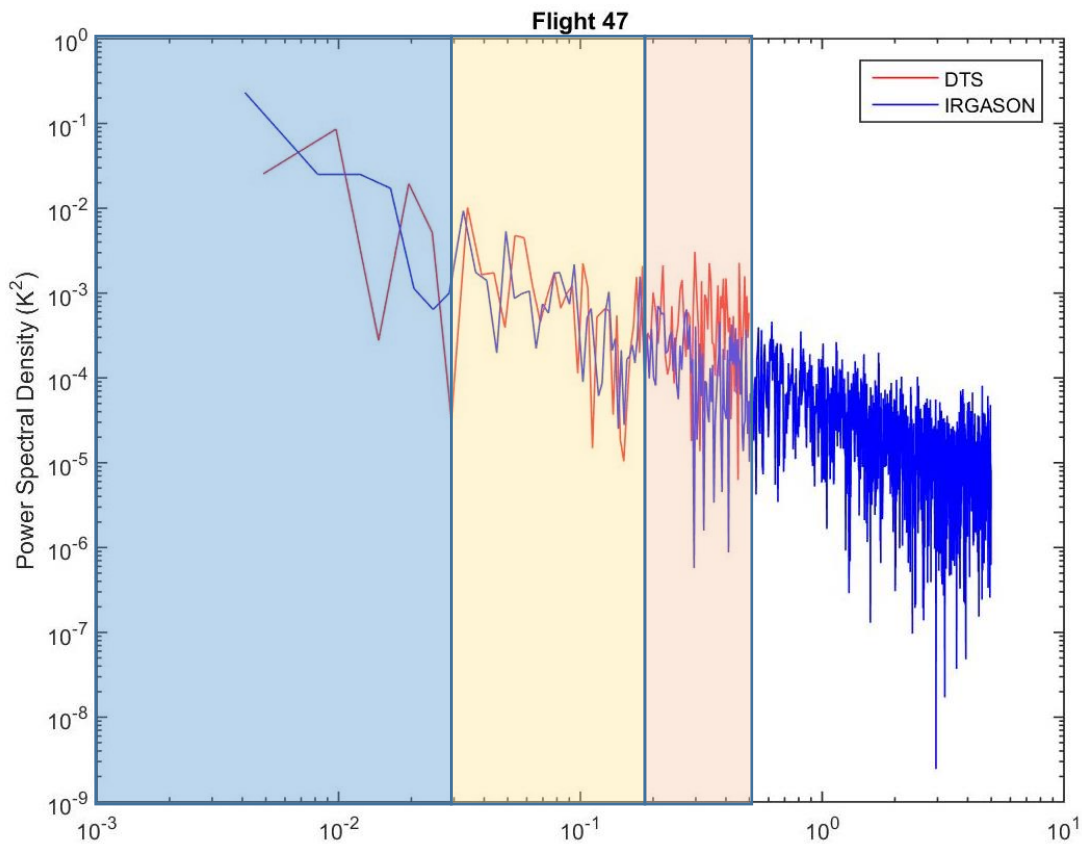


Figure 23: Comparative frequency plots from the DTS-derived data and the Irgason data. Slope of the Irgason data approaches a benchmark. The DTS frequency data, if it were sampling accurately, would follow Irgason frequency energy dissipation. The point along the plot where the DTS plot begins to rise up and level off is the indication that DTS data isn't correctly sampling anymore.

the DTS. This was done using spectral correction algorithms developed by the NewAg laboratory at Oregon State University.

The first step was to compare, via spectral analysis, the two spectra derived from the two measuring devices. Figure 23 shows an example plot that compares the two spectra (Appendix E contains the spectra comparison plots for all thirteen flights). While spectral correction, a process that attempts to reconcile lower-than-necessary sampling rates, did improve the underestimation issue with the DTS variance, it did not fully correct the problem. Figure 24 shows a sample plot of the new comparative variance plots (Appendix E contains all variance plots).

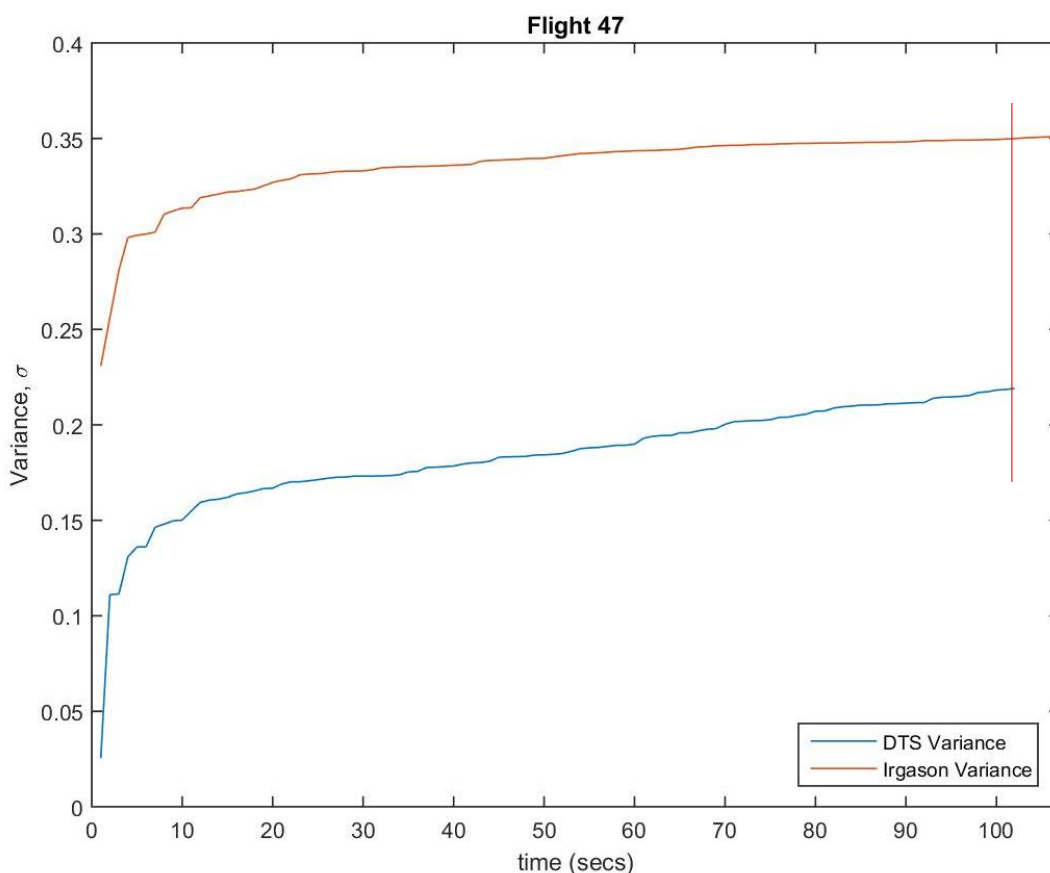


Figure 24: Corrected Variance values plotted with respect to time/frequency. This shows that at lower frequencies, the variance values are most different. As the frequency value increases, the variance values start to trend with each other. The vertical red line indicates where comparison variance values are made. Perhaps counter-intuitively, variance values are summated as one moves from left to right; the final point is that the variance is compared by looking at the last point on the DTS variance value and the Irgason variance value at the same frequency. This is shown via the red vertical line.

While the intention of the spectral correction process was to improve the assumed issue of the DTS's inability to sample at a high enough frequency to capture smaller scale turbulence events (turbulence events being the carrier of scalar information, including temperature), it showed another systemic issue with the DTS-derived information that wasn't initially thought to be a problem; sampling intervals.

A more thorough examination of Figure 23 is required to explain this discovery. The plot is broken into three representative sections. The middle shaded region represents the sampling interval where DTS and Irgason information is matched appropriately; in short, the DTS derived information is accurate. The right-most shaded region represents the area where DTS data is beginning to deviate away from the Irgason data. This 'leveling' off of DTS data is showing us that – even after spectral correction – the sampling rate isn't quite fast enough to accurately measure temperature changes at that frequency. Figure 23 shows a minimum function frequency of approximately 0.25 Hz, or 4 seconds.

The left-most shaded region is the corrected portion of an interesting point to the story. It is shown here that the two frequency plots aren't aligning, though the inaccuracy is fundamentally different here than in the right-most shaded region. This discrepancy is due to the unexpected issue of sampling interval. This discrepancy then indicates that flight times were too short to collect sufficient sampling points in time to hone in on a true variance calculation at that low a frequency.

The insights gleaned from this additional analysis showed two things. 1: Sampling times for variance calculations via a DTS could be faster, but spectral correction can significantly

contribute to the increase in variance calculation precision, and 2: the lower frequency values – which reflect the DTS’s ability to capture longer time scale events, was insufficient to accurately measure variance. Figure 24 shows the summary variance calculations over time (and therefore frequency). The pattern in these plots show this trend, and further indicate that, as was shown, the larger scale in accuracy was the true reason why DTS based variance calculations were underestimated.

On the Critical Components of the Calculation Process

In the analysis of this information, two important sensitivities were noticed: Bowen Ratio values and the temperature variance used from DTS-Derived data. Honing in on wet bulb temperature response rates are recommended next steps in increasing precision. The bigger question mark then is in how best to approach approximating the Bowen Ratios needed to then calculate sensible heat flux. Increasing accuracy in actual water vapor pressure calculations would presumably improve precision of plotted e_a and T_{air} (see Figures 11-13) used to interpret Bowen Ratios.

The use of this data set has shown a new problem in estimating Bowen Ratios. It was assumed plots like those in Figure’s 11-13 were accurate reflections of reality; meaning the complexity was an accurate interpretation of the state of the A.B.L.; or at the very least, partly accurate. As an investigation into data in Appendix D might glean, repeatable patterns within all of these plots can be seen; further indicating the complexity, yet repeatability of the patterns extracted through this approach. The biggest question moving forward then, is how best to accurately and sufficiently derive Bowen Ratio’s with similar data sets.

The second issue is the use of vertical temperature variance calculations in equations similar to (16) and (19). Variance is the significant factor in (16) and (19) (along with the Bowen Ratio in E flux calculations), therefore its accuracy is critical. Given how temperature data was collected via DTS: via a fast-response and duplexed fiber optic cable, it may be reasonable to argue that variance calculations done with this data are an appropriate reflection of our field design's ability to reduce noise. It is reasonable to assume that our variance calculations are continually less than Irgason variance values because our approach to capturing temperature successfully reduces noise. Mathematically though, this results in a variance number that is smaller, meaning (again, analyzing equation (16)) calculated H values would become smaller. This is an interesting result, but one that must be addressed. Current thinking is to re-evaluate the C_1 fitting parameter within (16). Further analysis would show the feasibility of this approach. The C_1 parameter is chosen because it is the only other constant in the equation that tracks on the same scale as σ (both are raised to the $3/2$ power), and it is the only non-dimensional number within the equation that is derived specifically for this equation (Tillman, 1972).

Summary

Utilization of DTS and UAV's as a means to capture reliable data for specific humidity profiles is determined to be feasible. Further calculations to create sensible and latent heat fluxes have proven to be plausible, but with some field modifications and programming modifications necessary deliver sufficient precision. Faster DTS sampling rates, an improved modification strategy for the wet bulb cable, and a more refined co-location of secondary sensors to improve precision are suggested. Duplexed fiber optic cables for temperature sensing are recommended

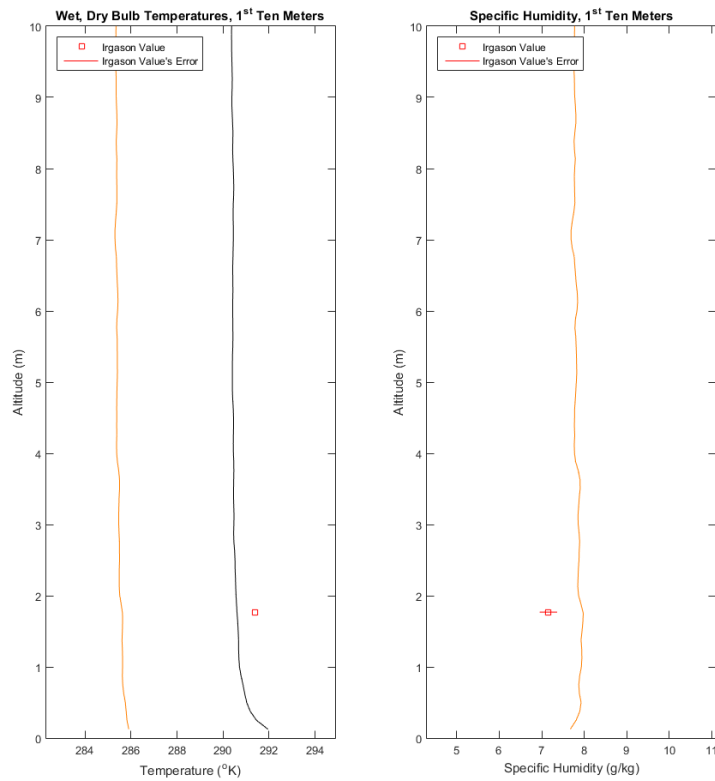
for any future deployments of this matter, as it is likely a means of reducing noise in the data that has previously not been accounted for in design equations like (16) and (19).

Use of UAV's to deploy fiber optic cables for heat and vapor fluxes may not be necessary. In all flights conducted last July, the significant changes occurred in the first 10-15m. However 30-40m profiles did provide new insight and showed previously unmeasured complexity in variation of air vapor pressure; and therefore Bowen Ratio derivations. Future deployments with the DTS configuration outlined in this study could be done with short towers as

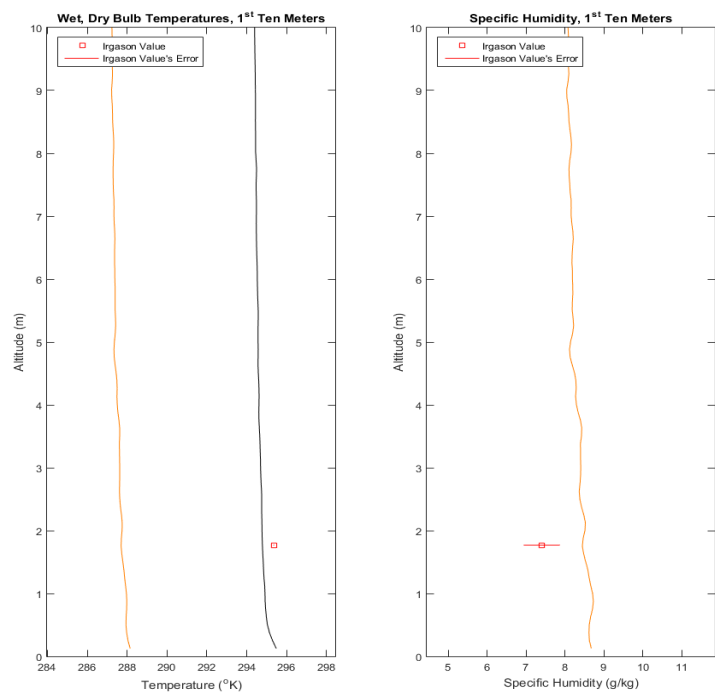
Given that Eddy Covariance is considered the most robust way of measuring energy, mass and momentum fluxes above ground despite relatively larger errors in even the most precise experimental setup and data analysis (Salesky et al., 2012), strong encouragement into a novel, cheaper and more robust alternative is suggested. The "Lasers and Drones" deployment has shown a path toward that novel alternative.

Appendix A: Temperature and Specific Humidity Profiles

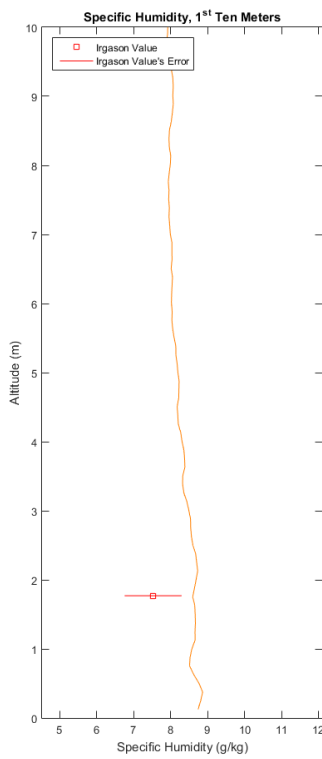
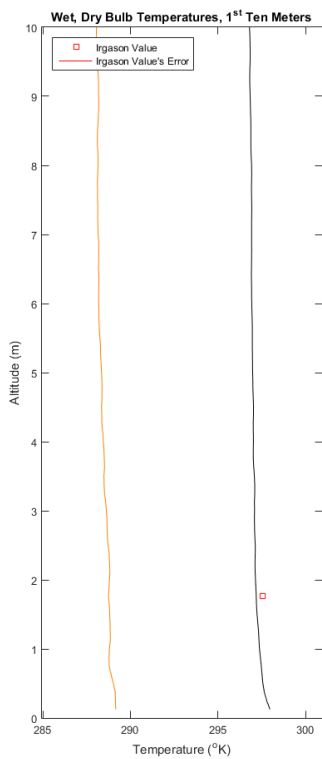
Flight 36
07/20/15
08:30



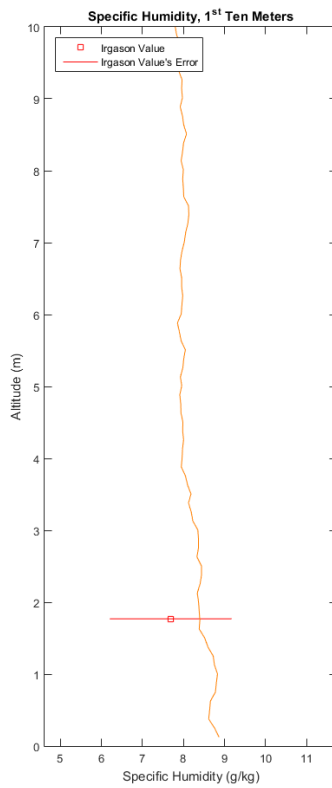
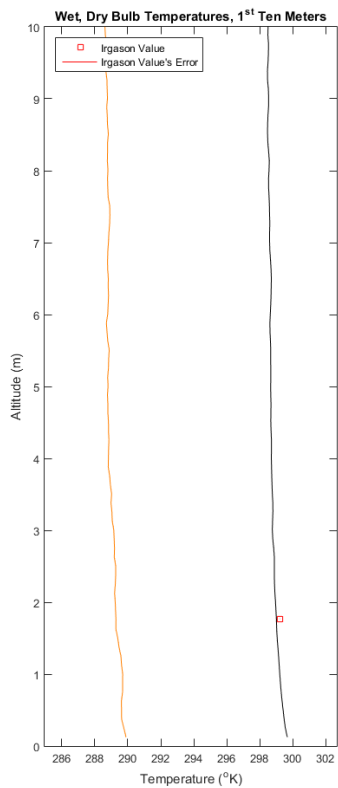
Flight 37
07/20/15
09:15



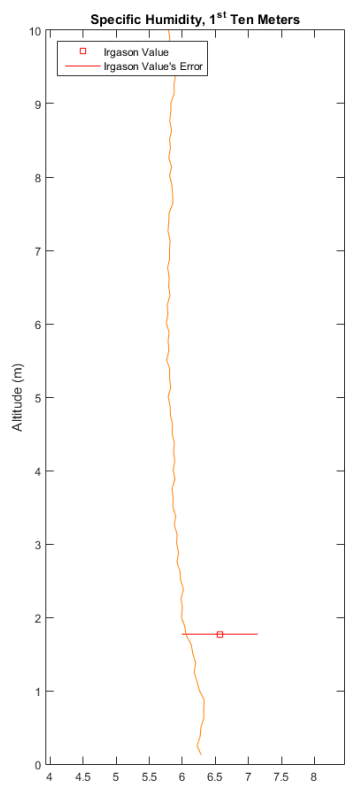
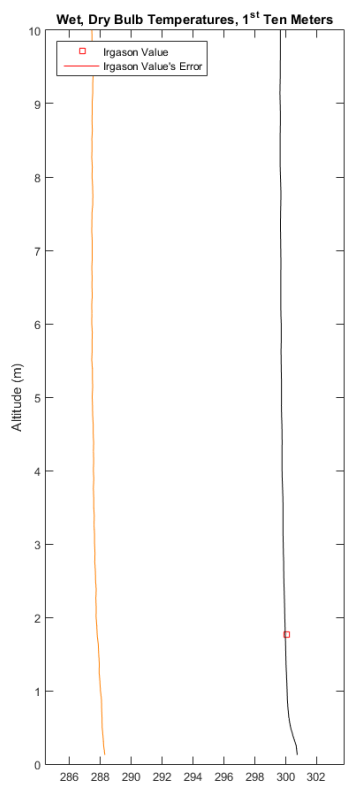
Flight 40
07/20/15
09:55



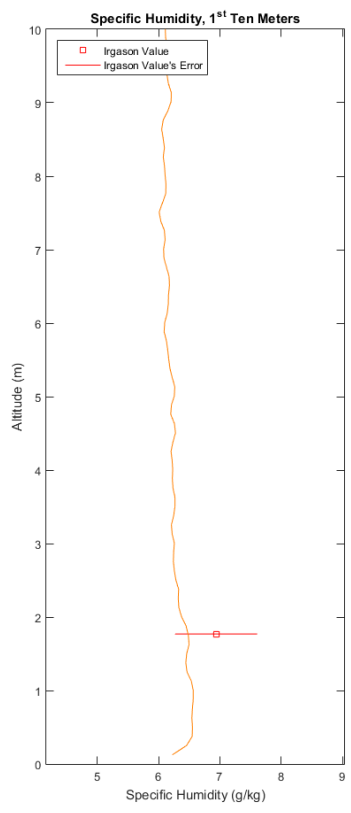
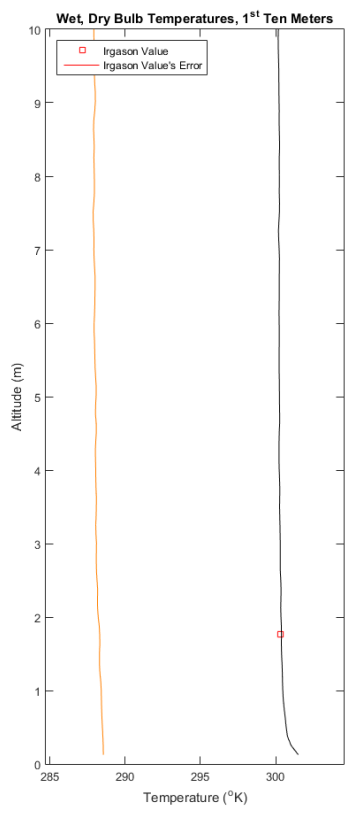
Flight 41
07/20/15
10:09



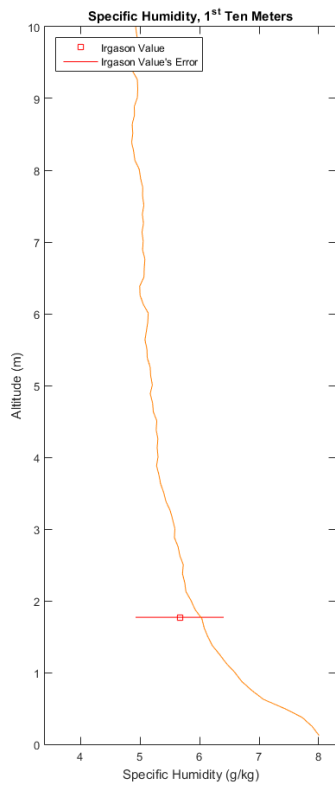
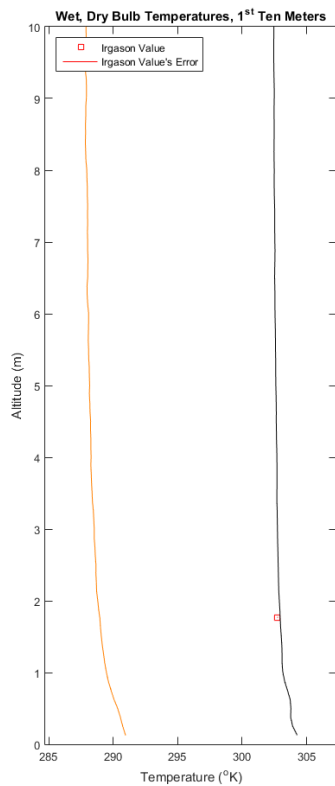
Flight 42
07/20/15
11:15



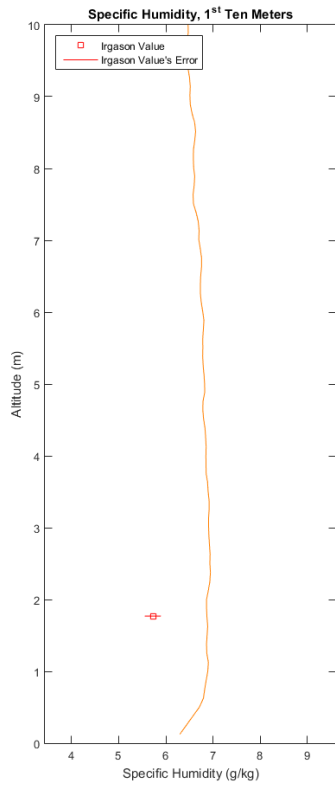
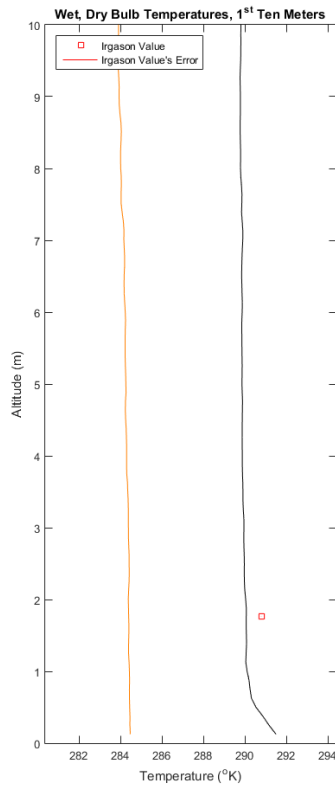
Flight 43
07/20/15
14:20



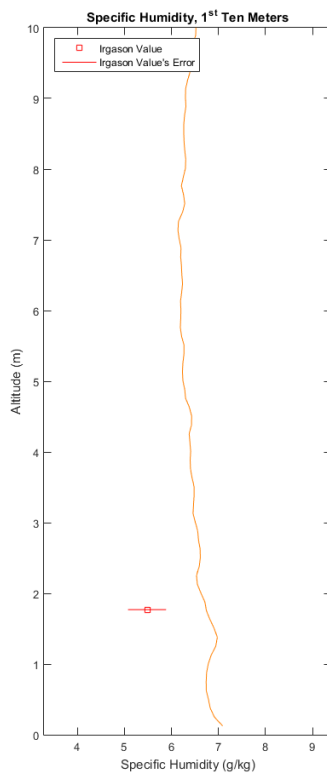
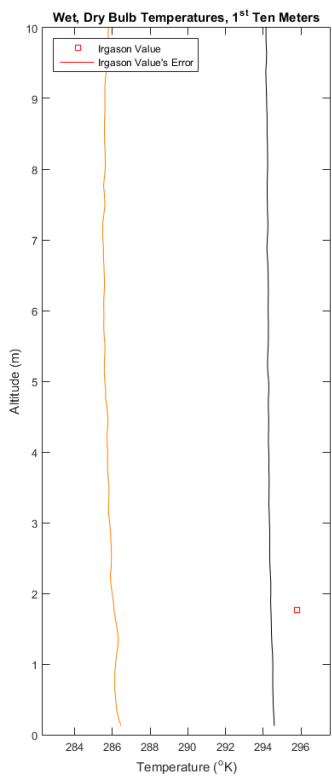
Flight 47
07/21/15
08:30



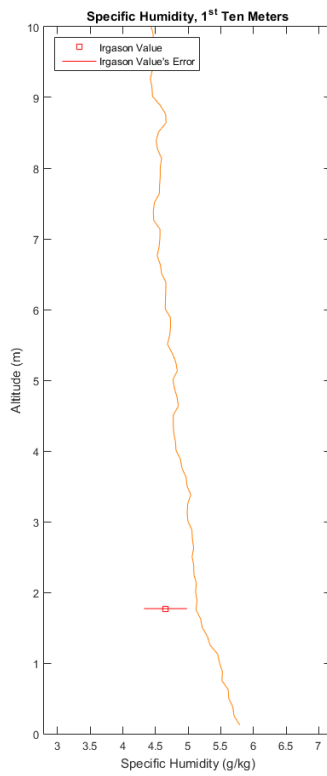
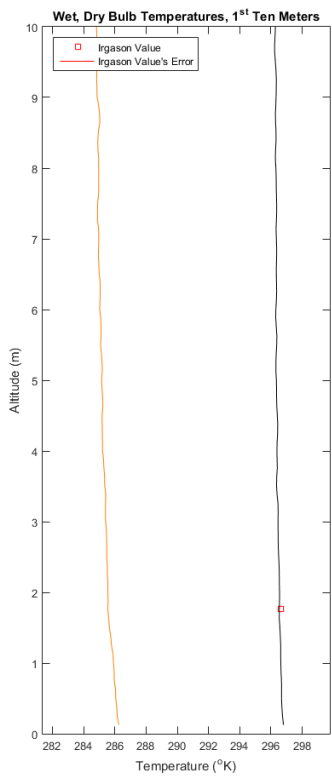
Flight 61
07/21/15
09:30



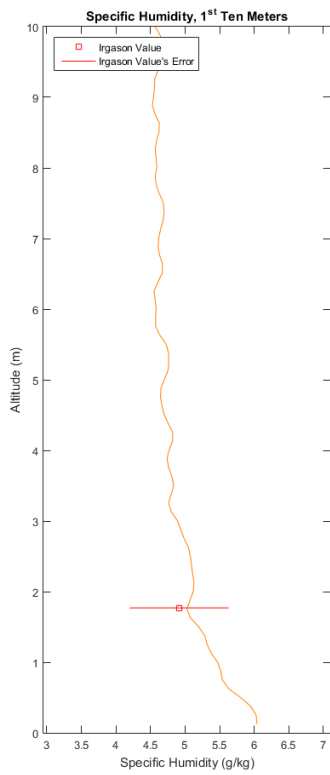
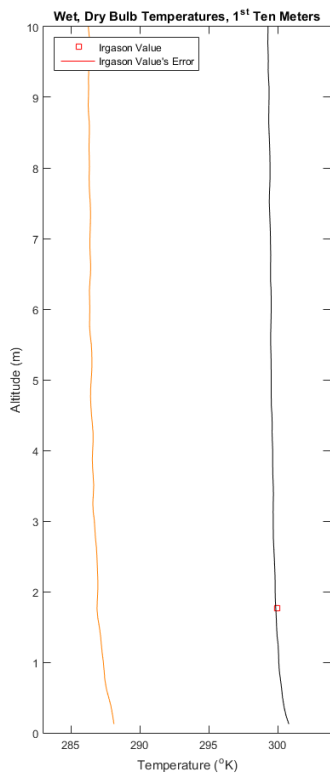
Flight 63
07/21/15
09:39



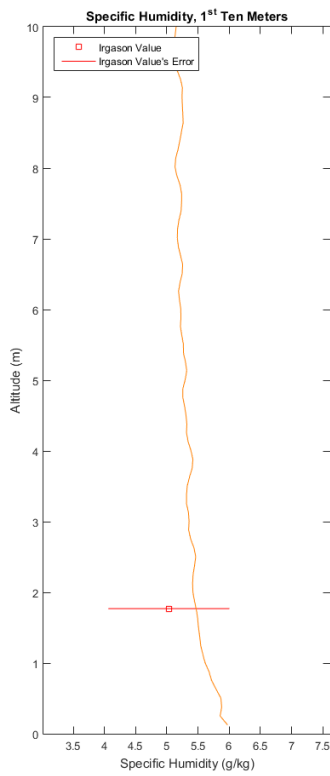
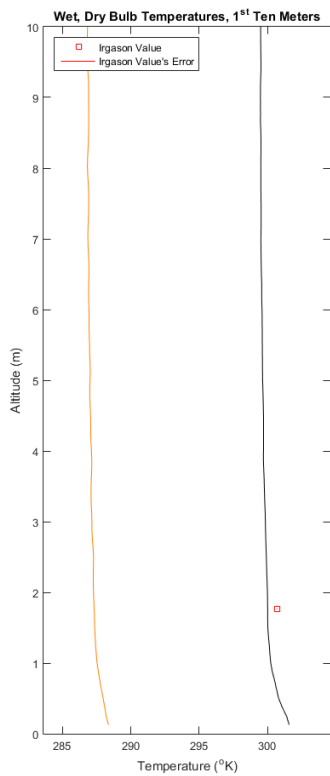
Flight 64
07/21/15
09:59



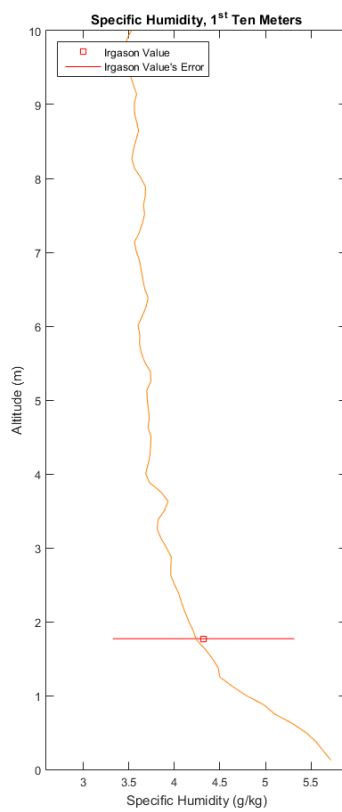
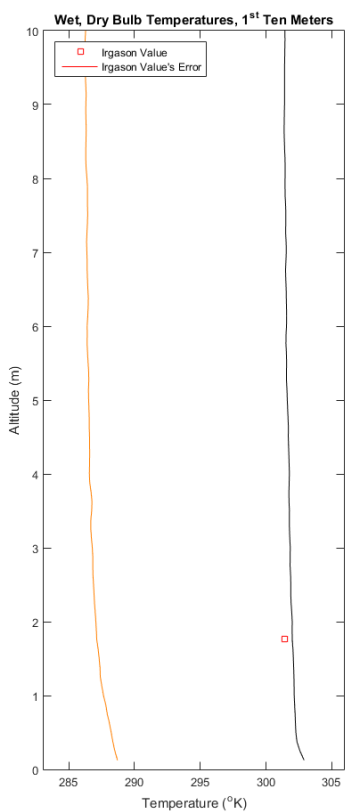
Flight 68
07/21/15
12:30



Flight 69
07/21/15
13:11

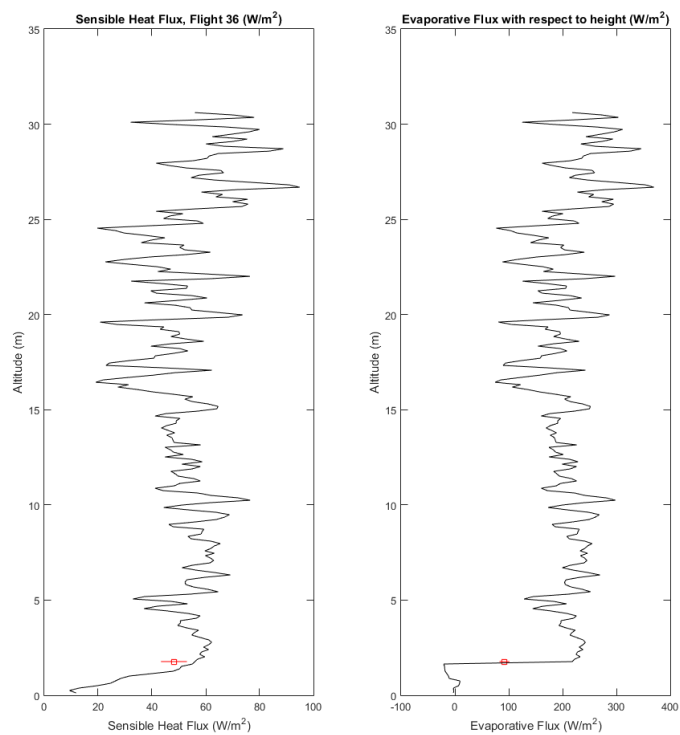


Flight 71
07/21/15
13:55

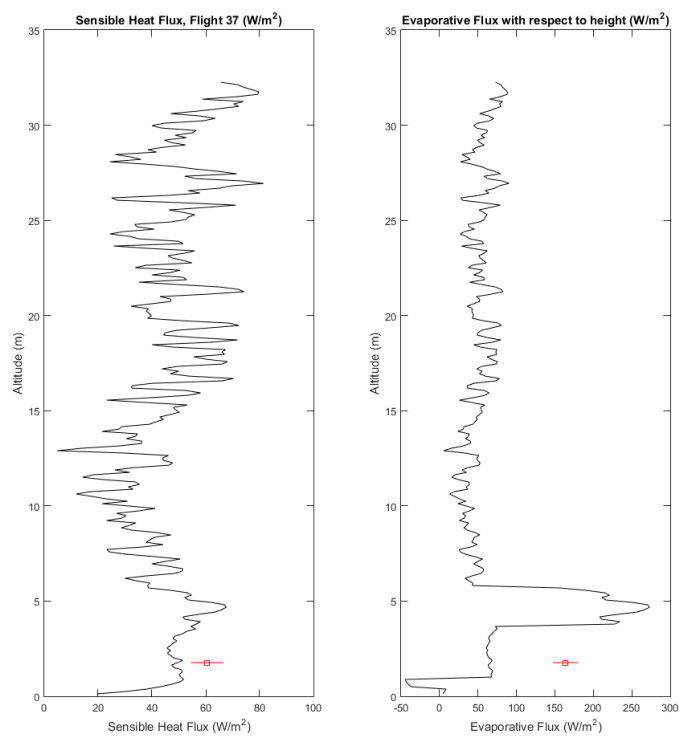


Appendix B: Flux Plots

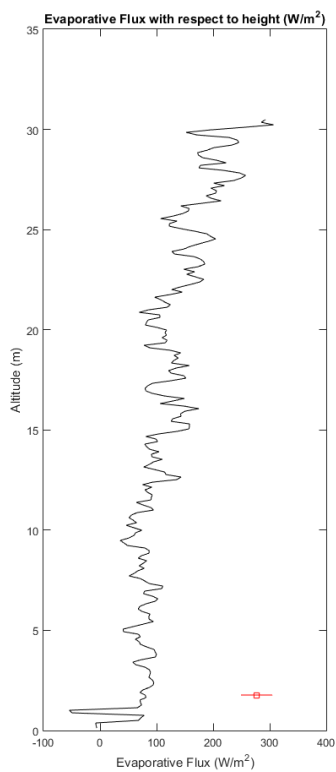
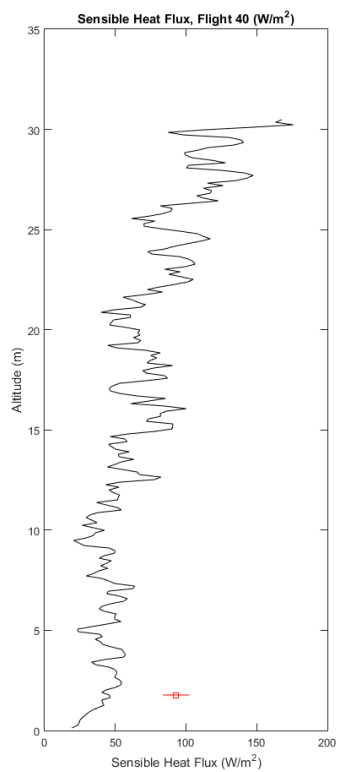
Flight 36
07/20/15
08:30



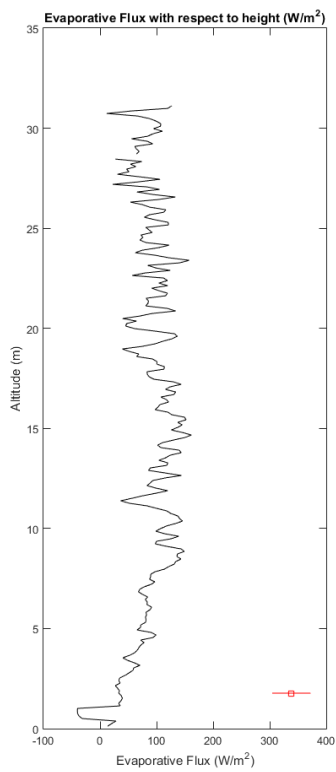
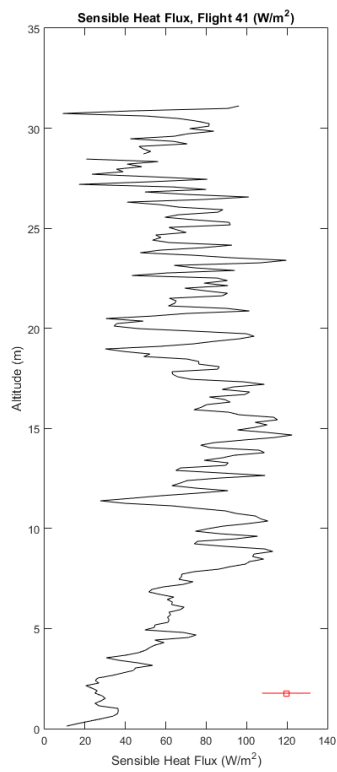
Flight 37
07/20/15
09:15



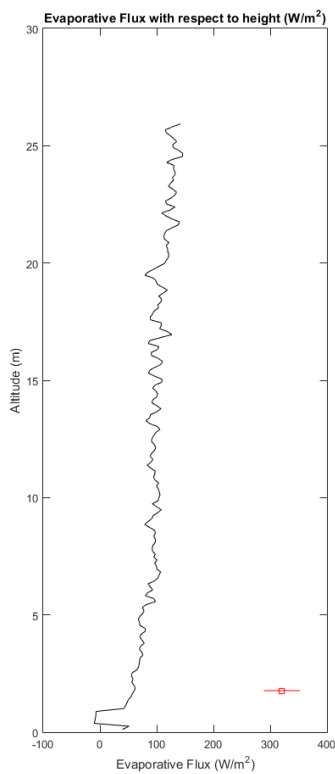
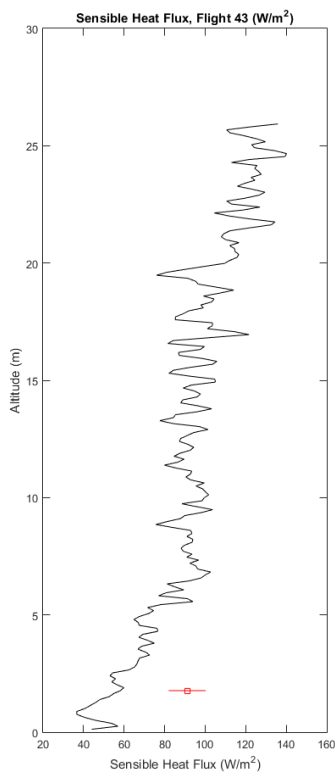
Flight 40
07/20/15
09:55



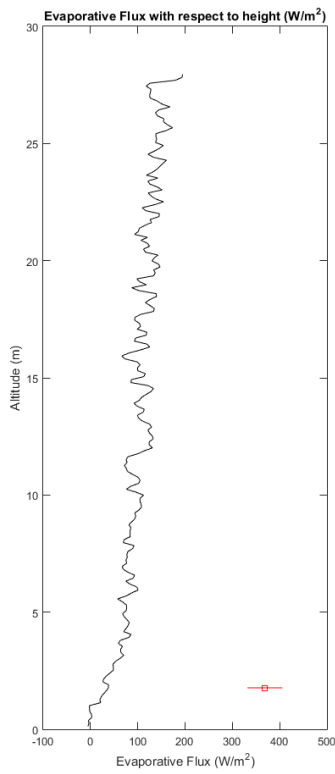
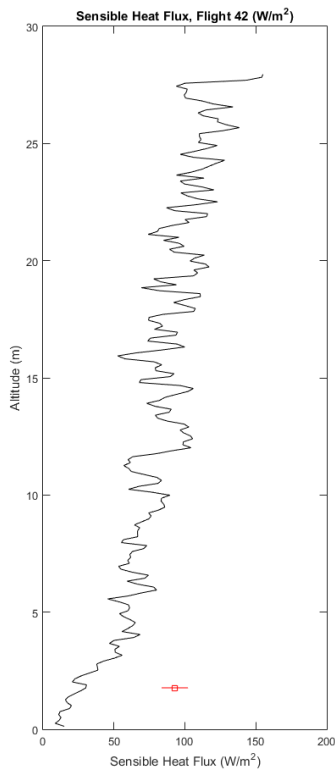
Flight 41
07/20/15
10:09



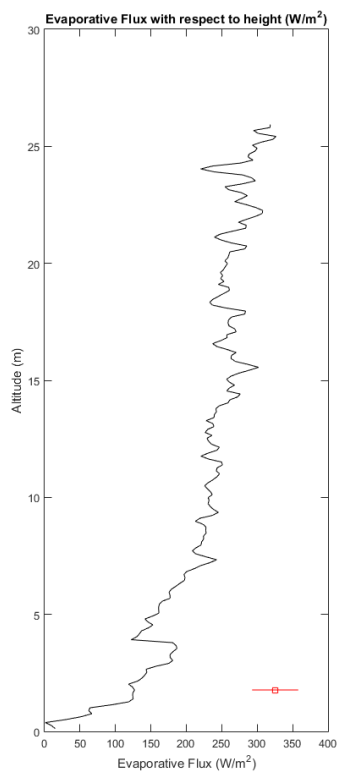
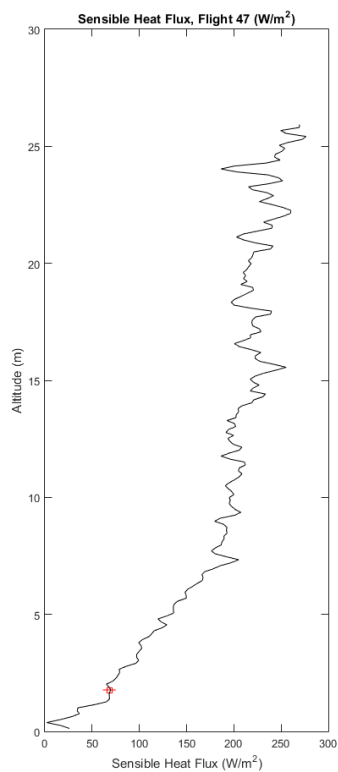
Flight 42
07/20/15
11:15



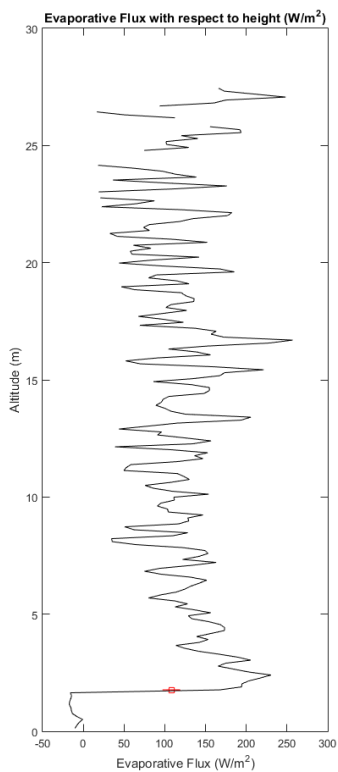
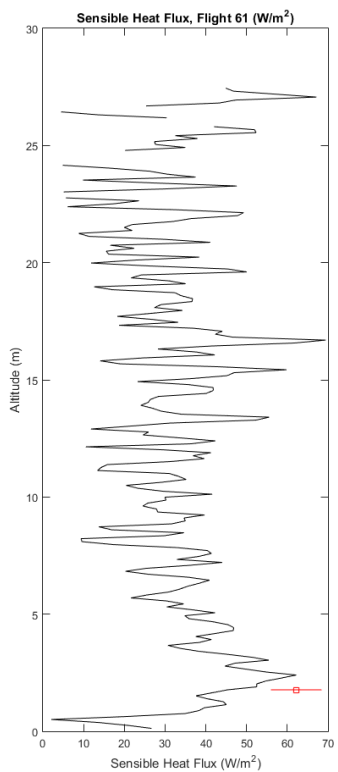
Flight 43
07/20/15
14:20



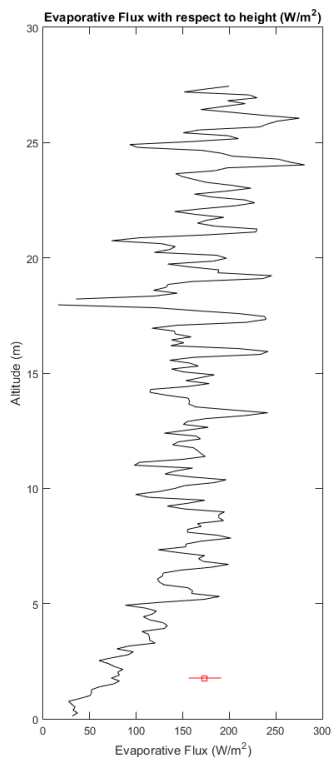
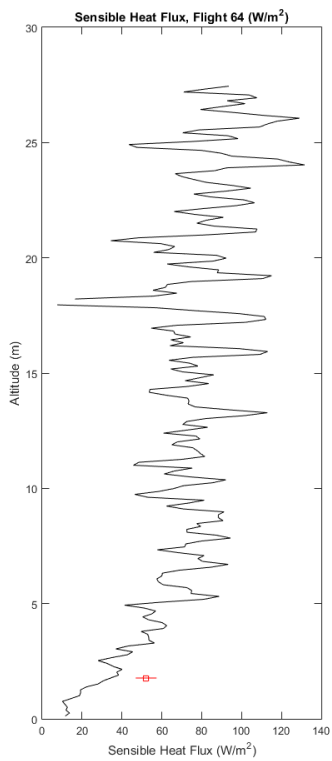
Flight 47
07/21/15
08:30



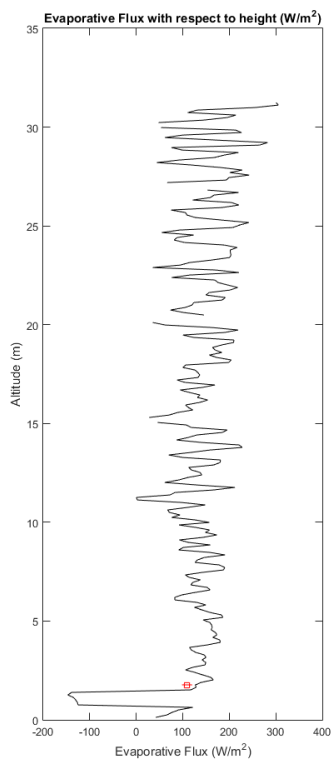
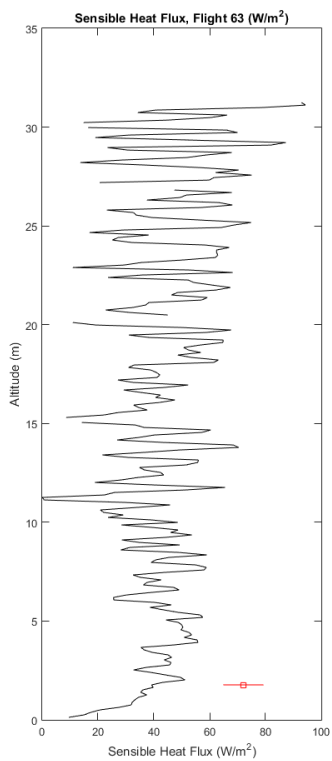
Flight 61
07/21/15
09:30



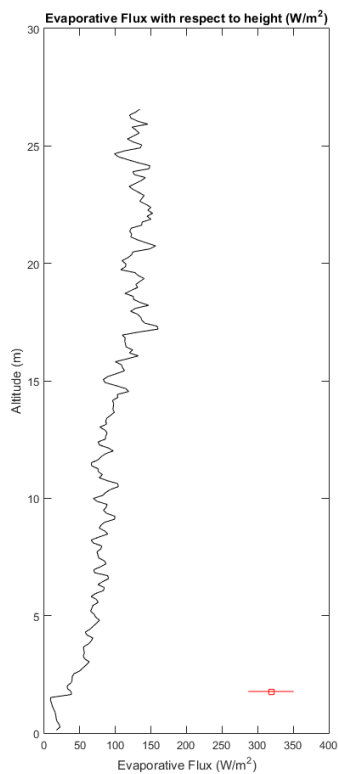
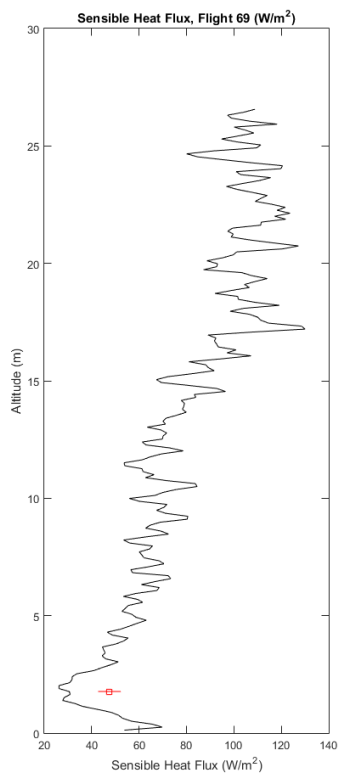
Flight 63
07/21/15
09:39



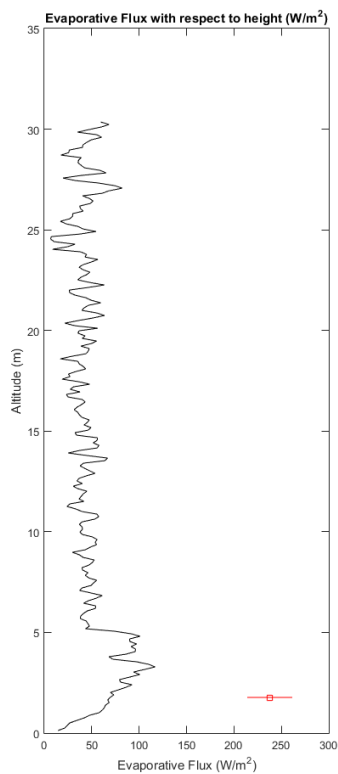
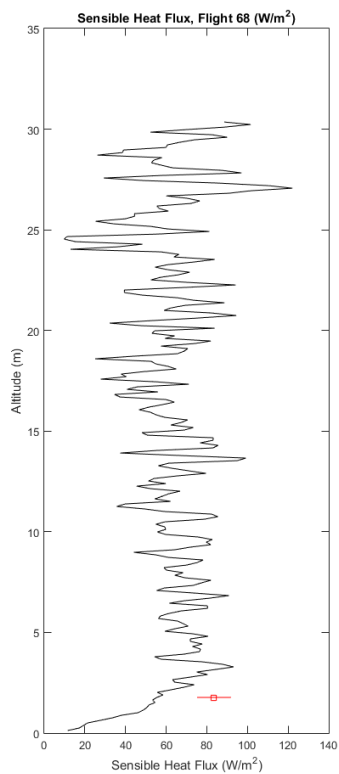
Flight 64
07/21/15
09:59



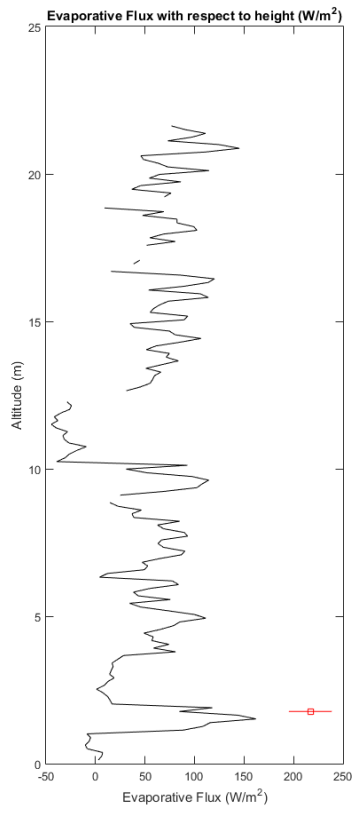
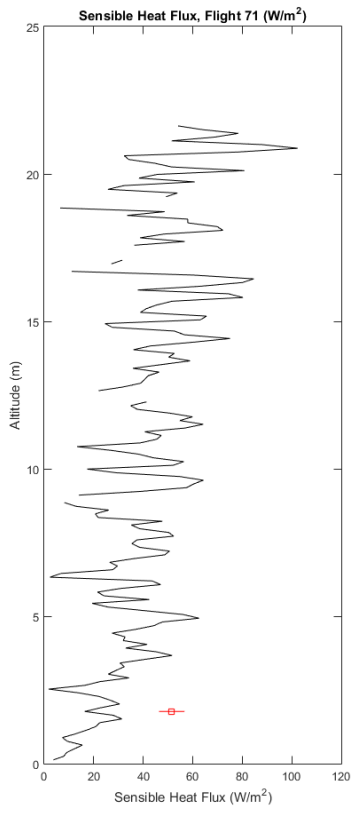
Flight 68
07/21/15
12:30



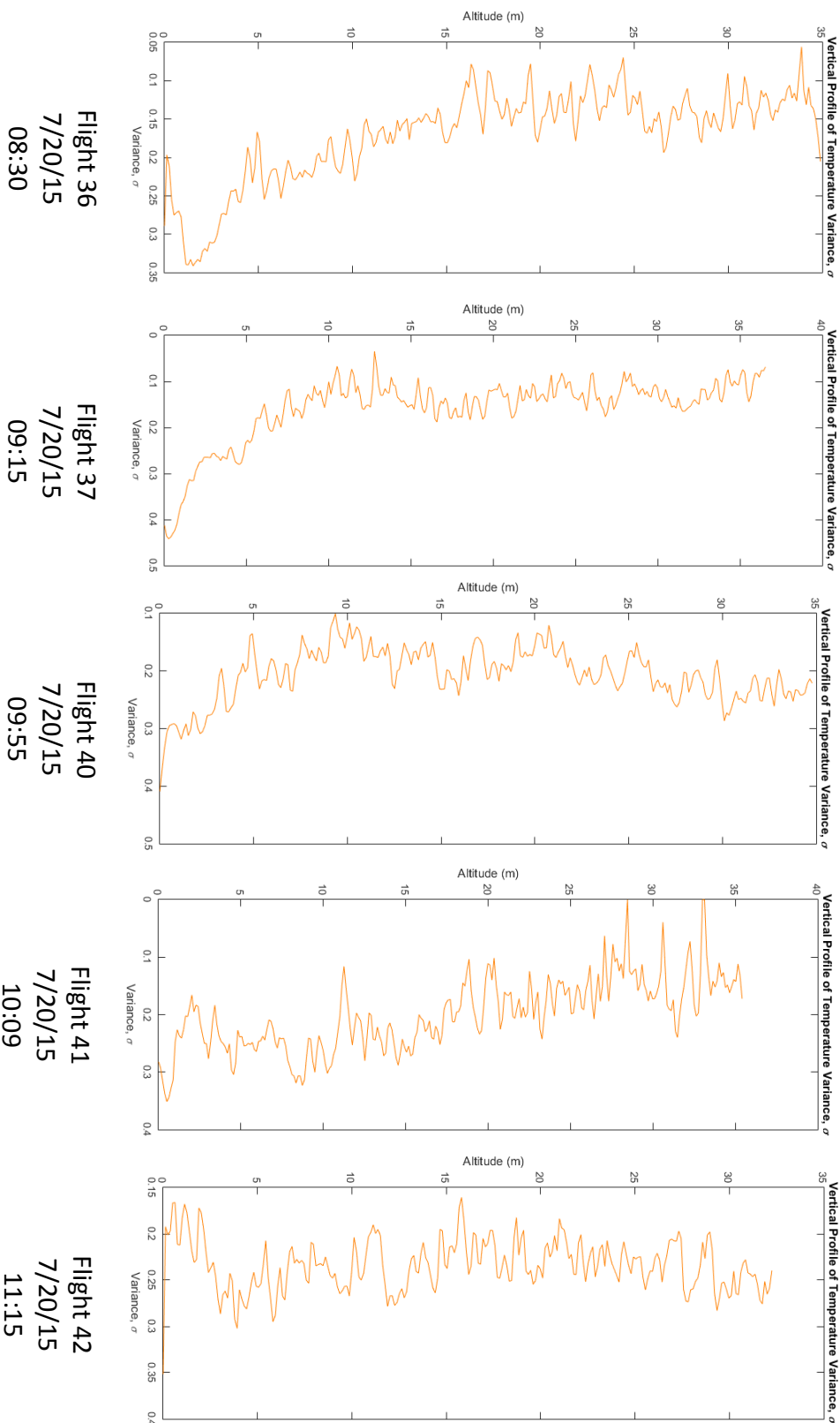
Flight 69
07/21/15
13:11

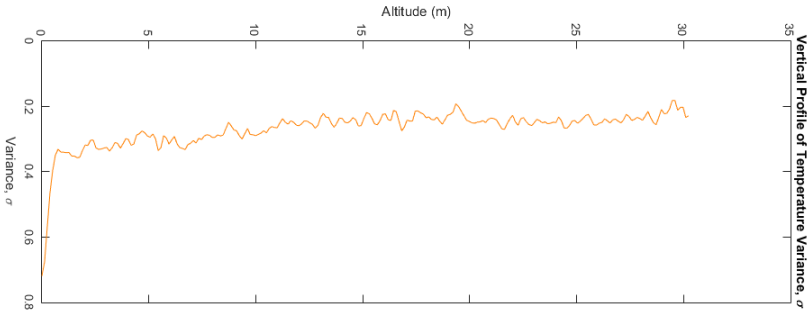


Flight 71
07/21/15
13:55

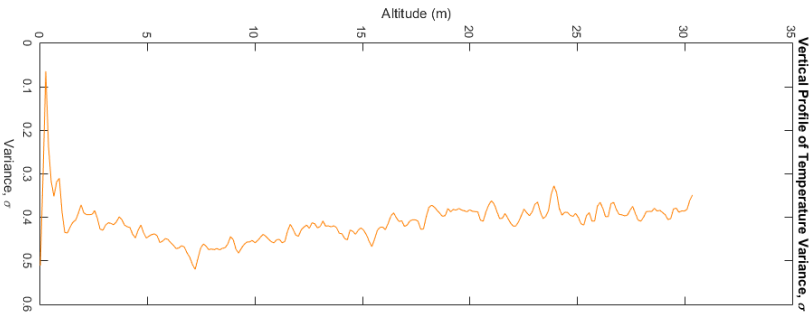


Appendix C: Variance Plots

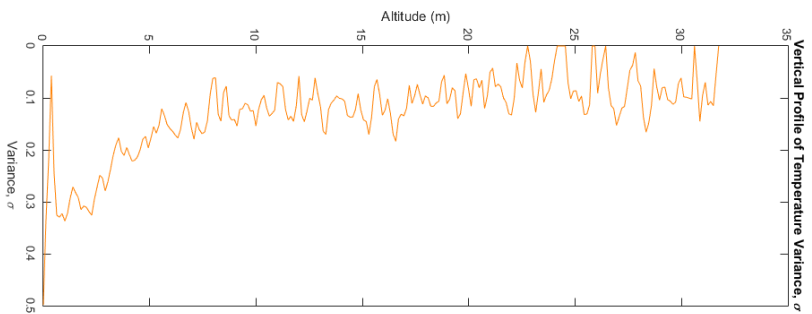




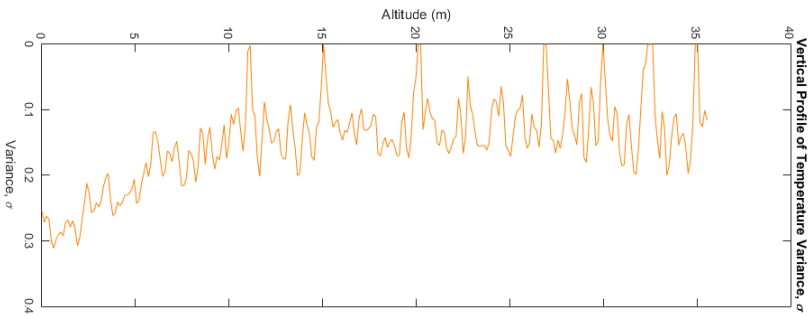
Flight 43
7/20/15
014:20



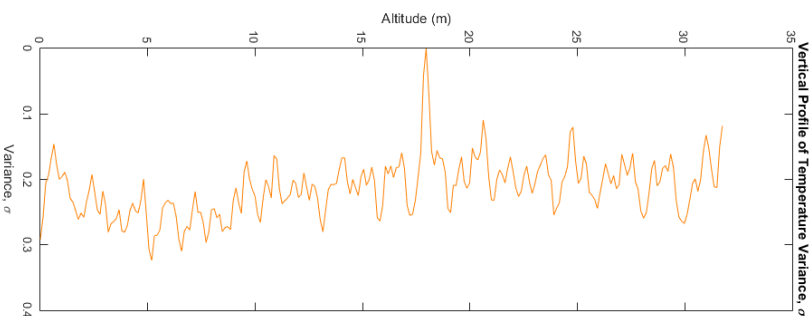
Flight 47
7/21/15
08:30



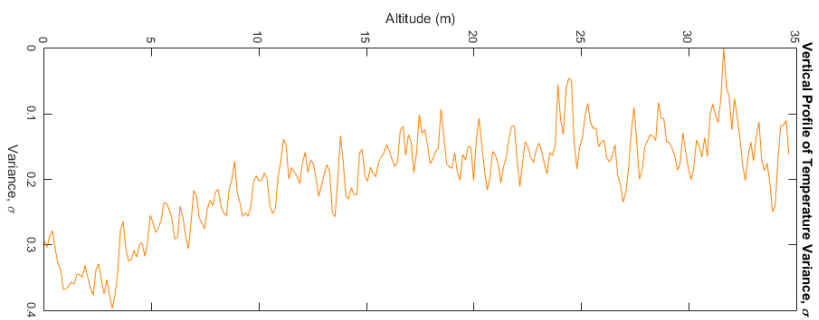
Flight 61
7/21/15
09:30



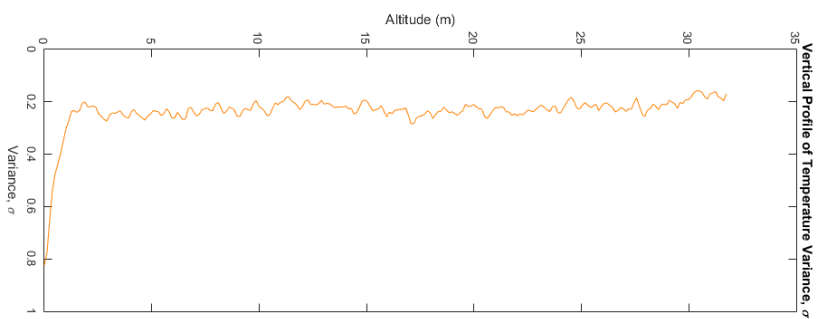
Flight 63
7/20/15
9:39



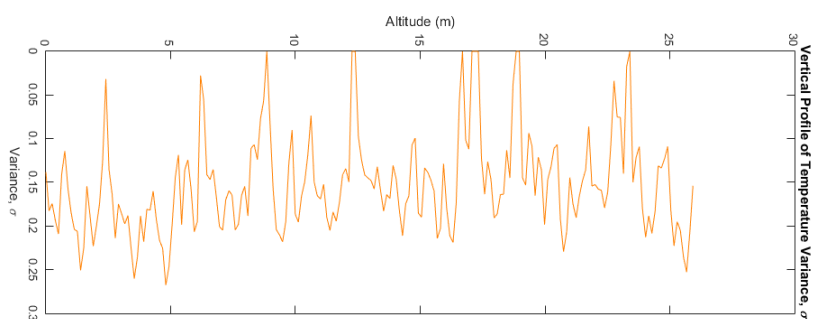
Flight 64
7/21/15
9:59



Flight 68
7/21/15
12:30

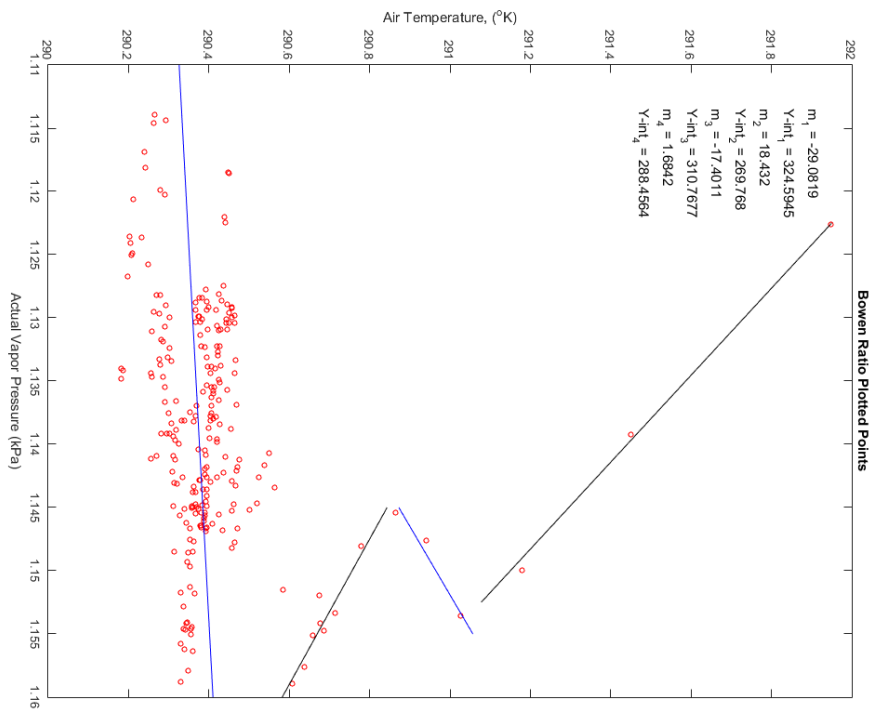


Flight 69
7/20/15
13:11

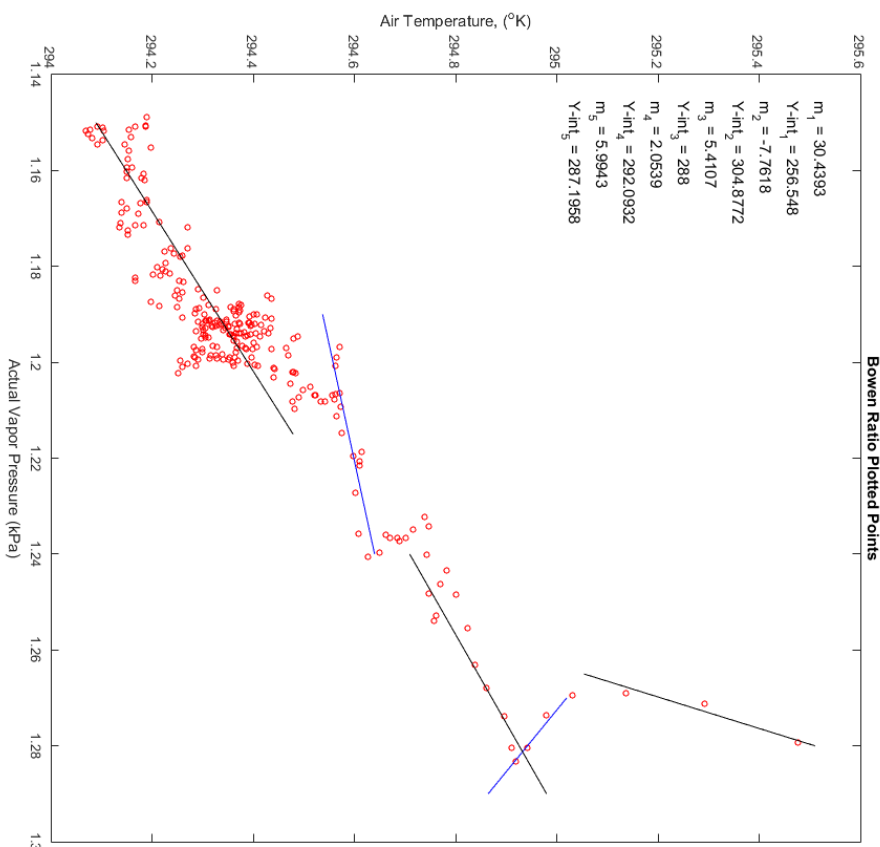


Flight 71
7/21/15
13:55

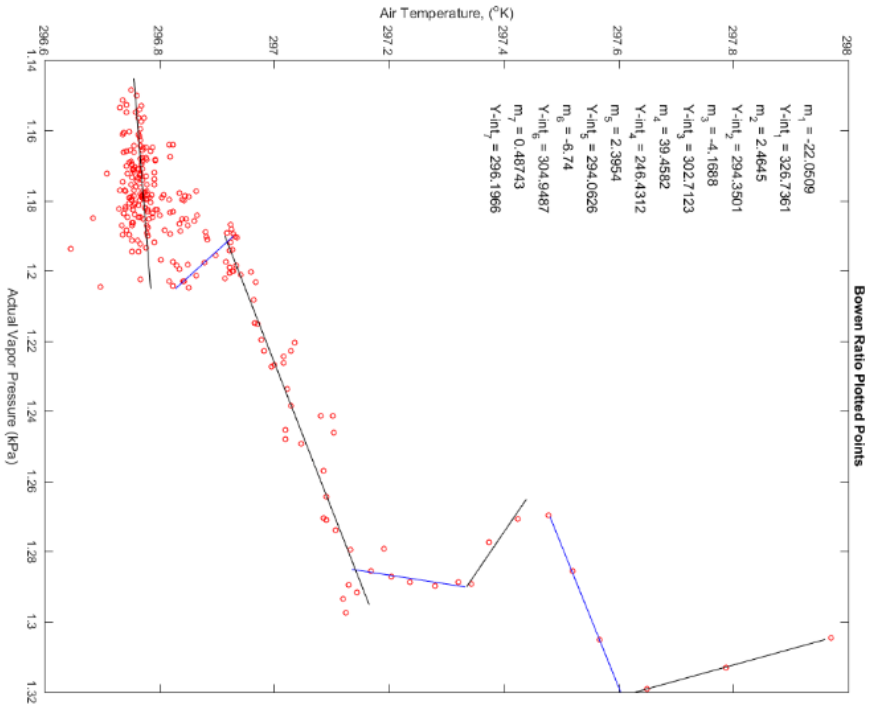
Appendix D: Bowen Ratio Plots



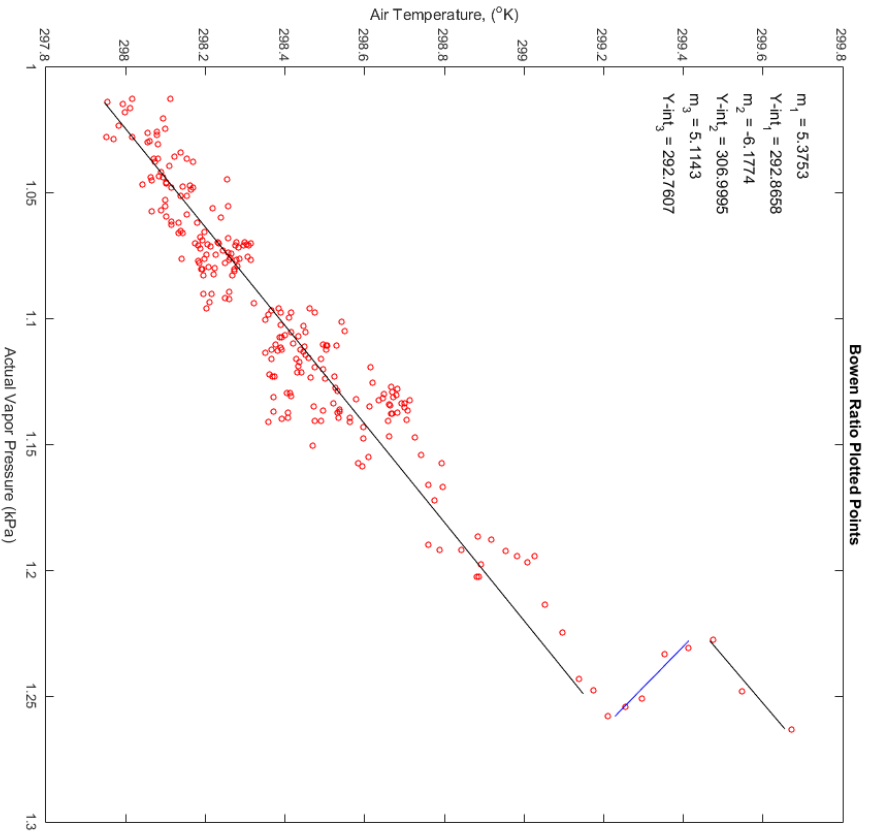
Flight 36
7/20/15
08:30



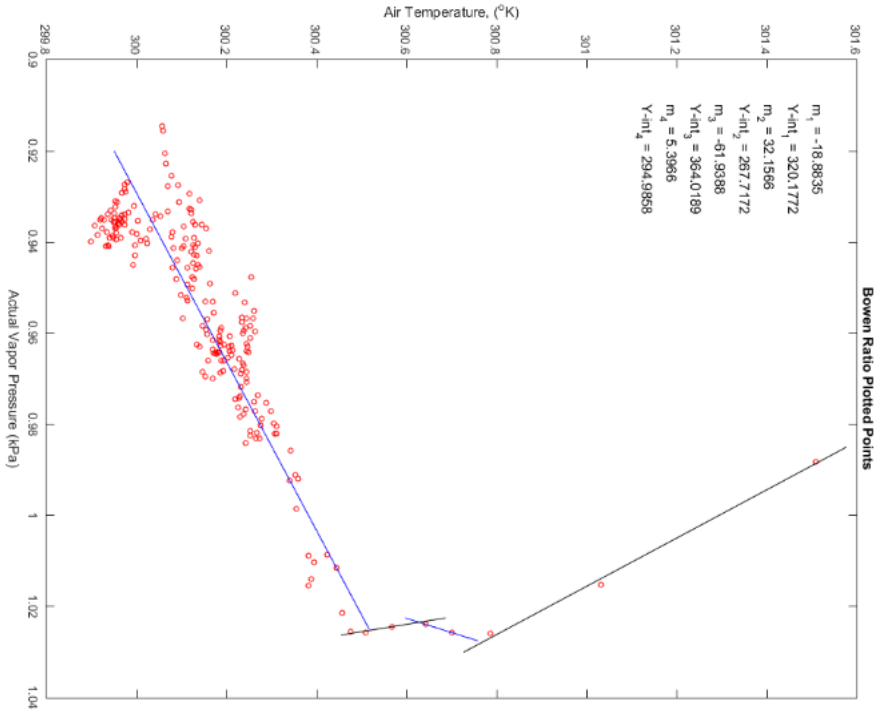
Flight 37
7/20/15
09:15



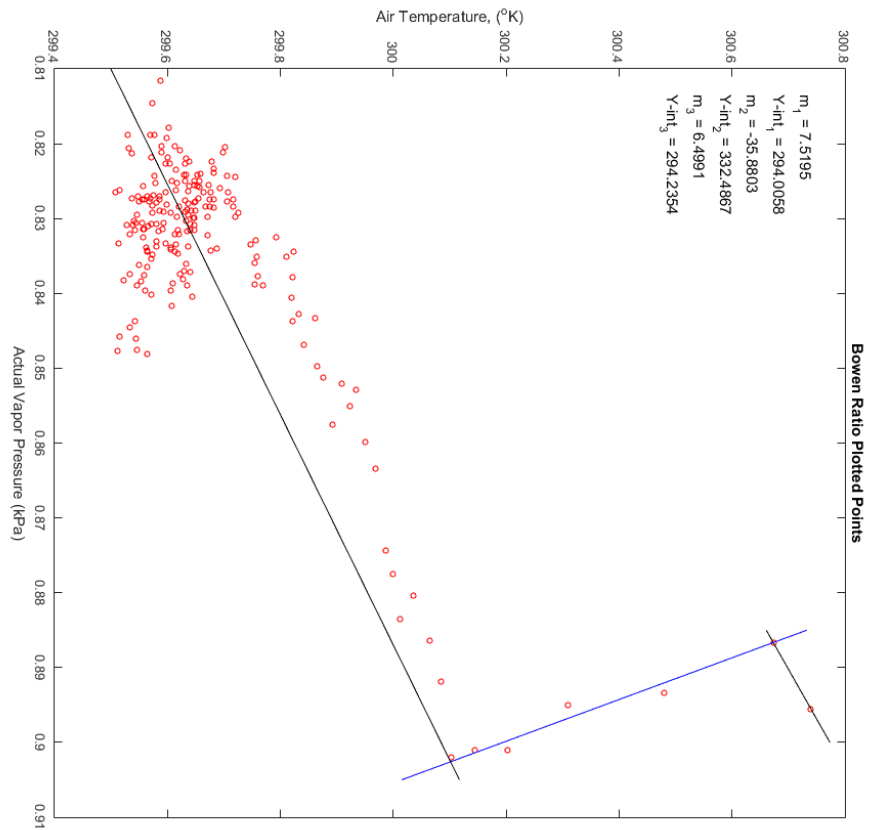
Flight 40
7/20/15
09:55



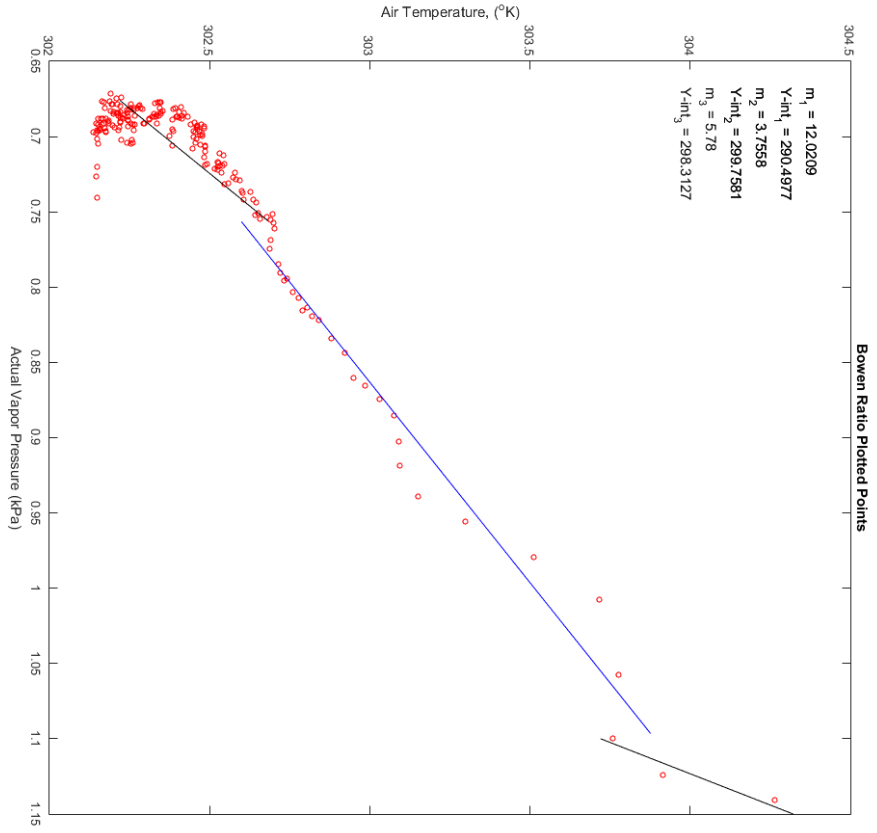
Flight 41
7/20/15
10:09



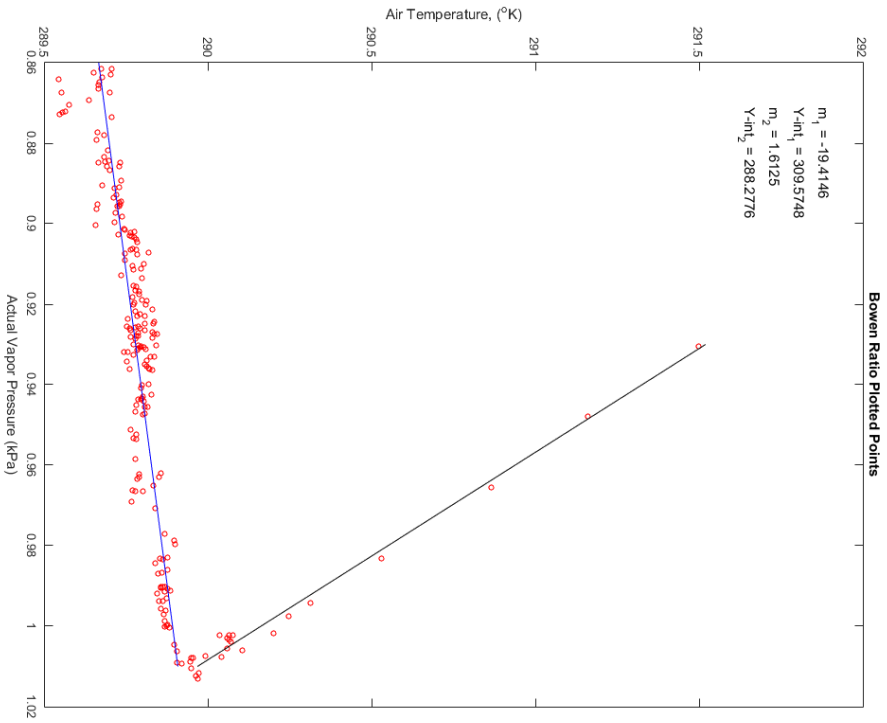
Flight 42
7/20/15
11:15



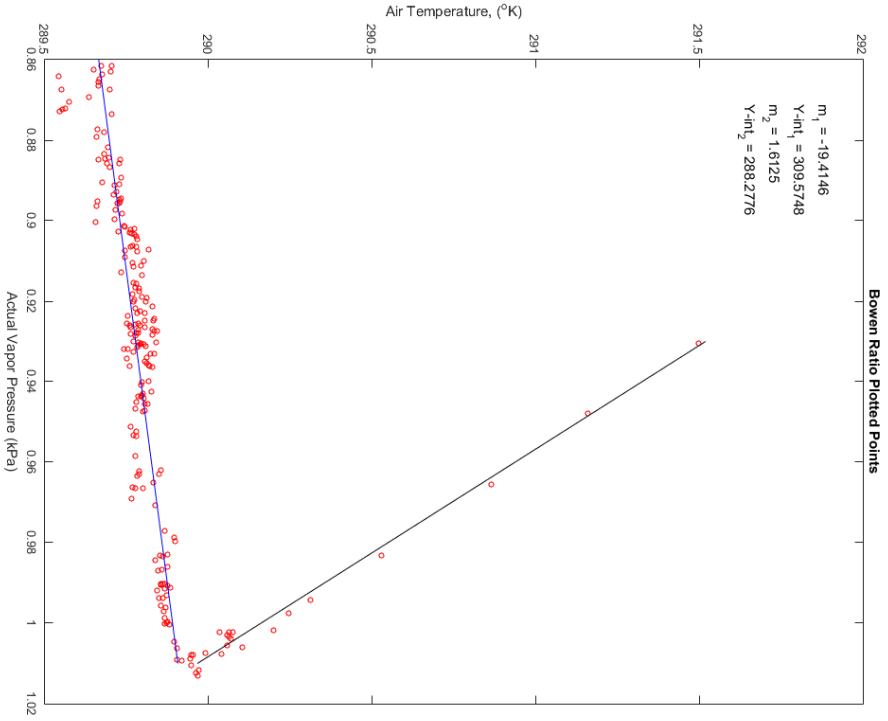
Flight 43
7/20/15
14:20



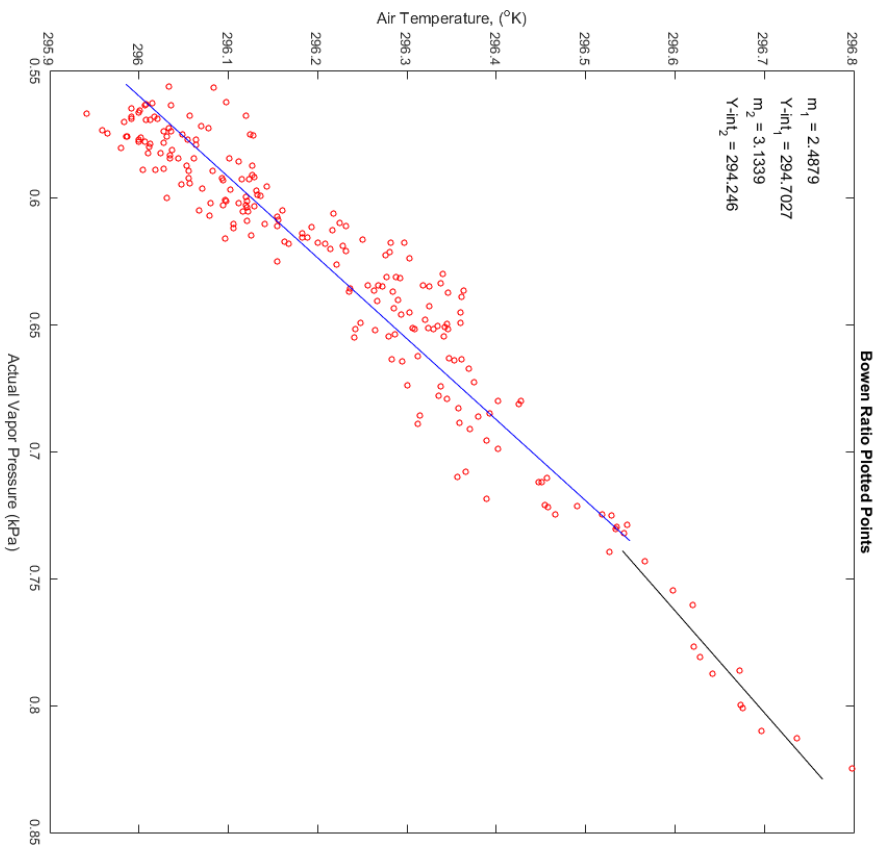
Flight 47
7/21/15
08:30



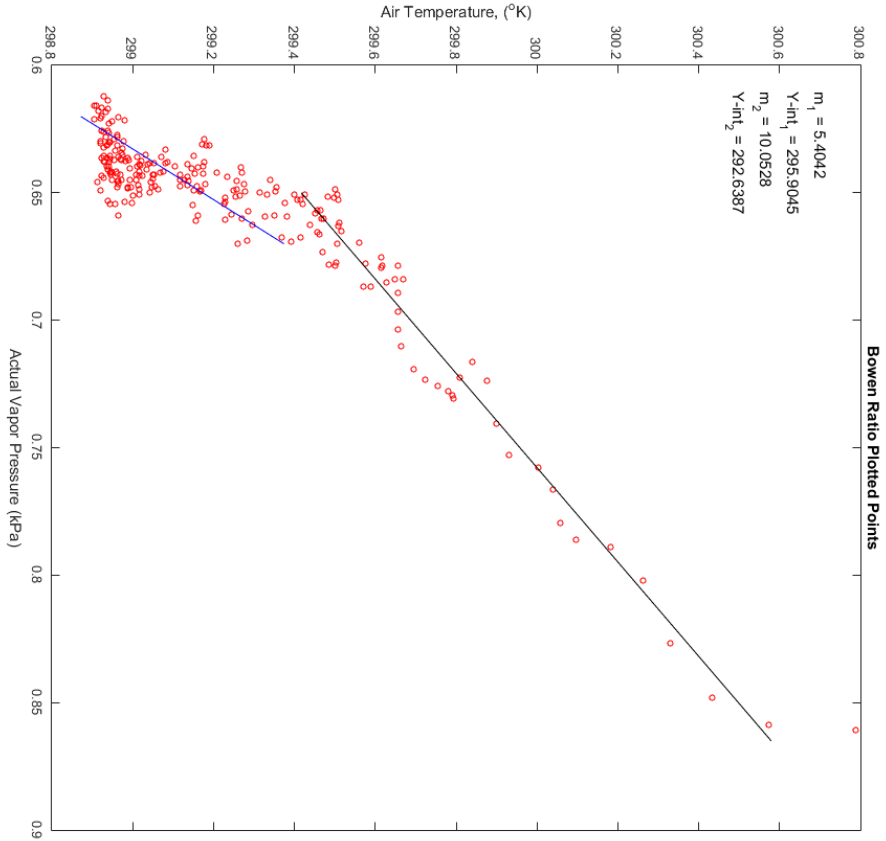
Flight 61
7/21/15
9:30



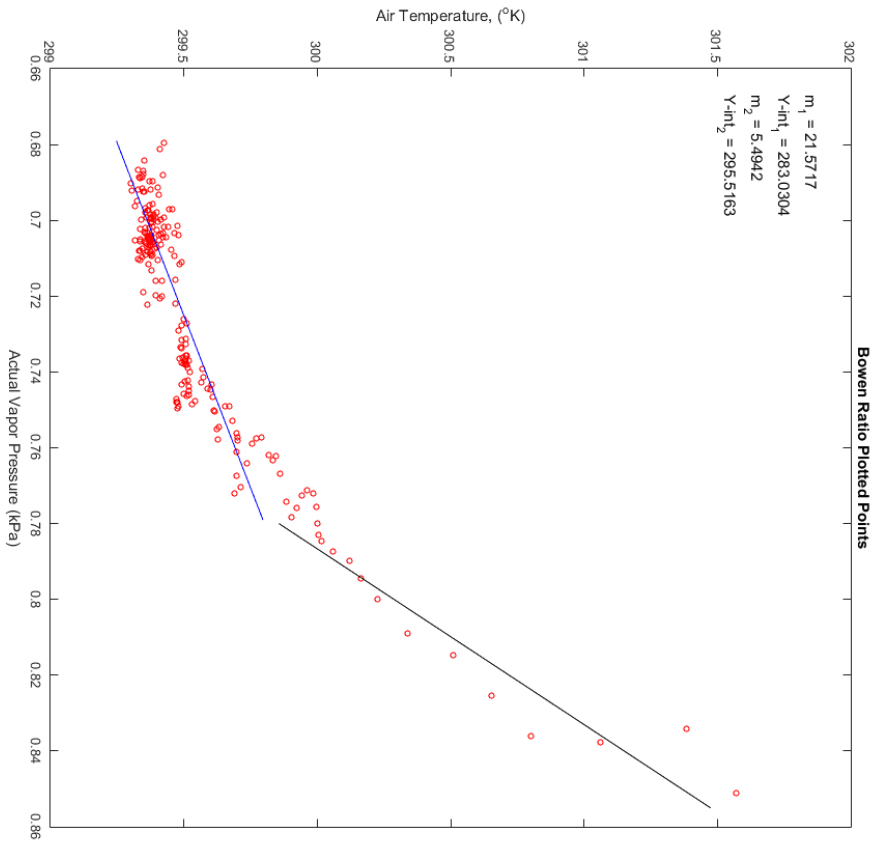
Flight 63
7/21/15
9:39



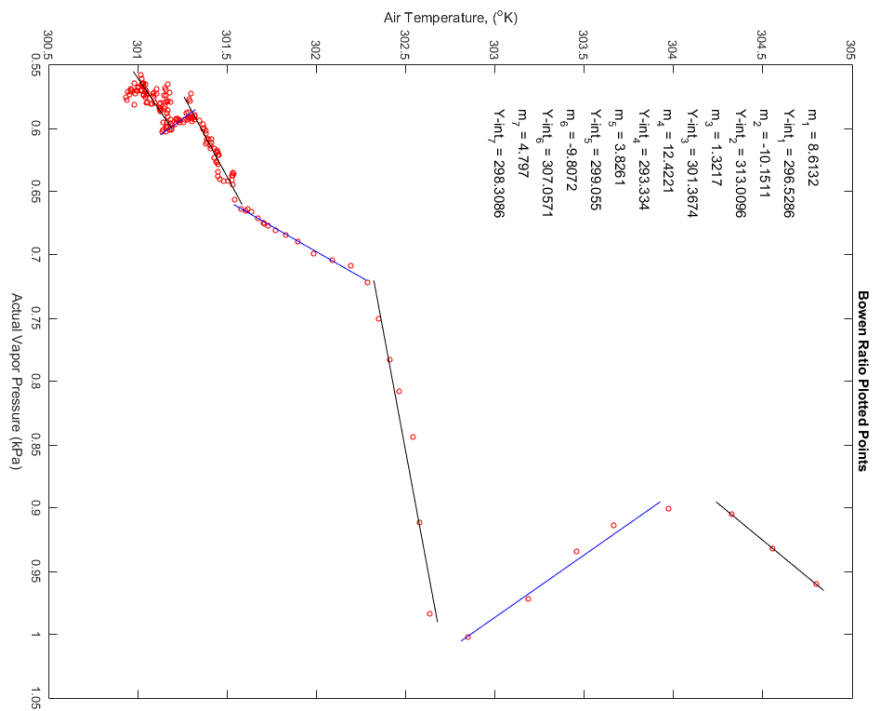
Flight 64
7/21/15
9:59



Flight 68
7/21/15
12:30



Flight 69
7/21/15
13:11



Flight 71
7/21/15
13:11

BIBLIOGRAPHY

3M Specifications Sheet for Vent Tape: Technical Specifications Sheet, n.d.

Allen, R.G., Pereira, L.S., Raes, D., Smith, M., 1998. Crop Evapotranspiration: Guidelines for Computing Crop Water Requirements.

Arnon, A., Selker, J., Lensky, N., 2014. Correcting artifacts in transition to a wound optic fiber: Example from high-resolution temperature profiling in the Dead Sea. *Water Resour. Res.* 50, 5329–5333. doi:10.1002/2013WR014910

Aubinet, M., Vesala, T., Papale, D. (Eds.), 2012. *Eddy Covariance*. Springer Netherlands, Dordrecht.

Bakker, M., Caljé, R., Schaars, F., van der Made, K.-J., de Haas, S., 2015. An active heat tracer experiment to determine groundwater velocities using fiber optic cables installed with direct push equipment: heat tracer experiments with vertical fiber optic cables. *Water Resour. Res.* 51, 2760–2772. doi:10.1002/2014WR016632

Bond, R.M., Stubblefield, A.P., Van Kirk, R.W., 2015. Sensitivity of summer stream temperatures to climate variability and riparian reforestation strategies. *J. Hydrol. Reg. Stud.* 4, 267–279. doi:10.1016/j.ejrh.2015.07.002

Bowen, I.S., 1926. Bowen_1926_The Ratio of heat Losses by Conduction and by Evaporation from any Water Surface.pdf.

Briggs, M.A., Lautz, L.K., McKenzie, J.M., Gordon, R.P., Hare, D.K., 2012. Using high-resolution distributed temperature sensing to quantify spatial and temporal variability in vertical hyporheic flux: HIGH-RESOLUTION HYPORHEIC FLUX PATTERNS. *Water Resour. Res.* 48, n/a-n/a. doi:10.1029/2011WR011227

Brutsaert, W., 2005. *Hydrology: An Introduction*.

Brutsaert, W., 1982. *Evaporation into the Atmosphere: Theory, History, and Applications*. Reidel, Dordrecht, Holland/ Boston, U.S.A.

Campbell Scientific: IRGASON Integrated Gas Analyzer and Sonic Anemometer, 2014.

Castellví, F., 2012. Fetch requirements using surface renewal analysis for estimating scalar surface fluxes from measurements in the inertial sublayer. *Agric. For. Meteorol.* 152, 233–239. doi:10.1016/j.agrformet.2011.10.004

BIBLIOGRAPHY (Continued)

- Castellví, F., Snyder, R.L., 2010. A New Procedure Based on Surface Renewal Analysis to Estimate Sensible Heat Flux: A Case Study over Grapevines. *J. Hydrometeorol.* 11, 496–508. doi:10.1175/2009JHM1151.1
- Dakin, J.P., Pratt, D.. J., Bibby, G.W., Ross, J.N., 1985. Distributed optical fibre Raman temperature sensor using a semiconductor light source and detector. *Electron. Lett.* 21, 569-.
- Davis, T.W., Kuo, C.-M., Liang, X., Yu, P.-S., 2012. Sap Flow Sensors: Construction, Quality Control and Comparison. *Sensors* 12, 954–971. doi:10.3390/s120100954
- de Jong, S.A.P., Slingerland, J.D., van de Giesen, N.C., 2015. Fiber optic distributed temperature sensing for the determination of air temperature. *Atmospheric Meas. Tech.* 8, 335–339. doi:10.5194/amt-8-335-2015
- Dingman, S.L., 2008. *Physical Hydrology: 2nd Edition*, 2nd ed. Waveland Press, Inc.
- Euser, T., Luxemburg, W.M.J., Everson, C.S., Mengistu, M.G., Clulow, A.D., Bastiaanssen, W.G.M., 2014. A new method to measure Bowen ratios using high-resolution vertical dry and wet bulb temperature profiles. *Hydrol. Earth Syst. Sci.* 18, 2021–2032. doi:10.5194/hess-18-2021-2014
- Fedorovich, E., 2011. Wyngaard, J. C., 2010: *Turbulence in the Atmosphere*: Cambridge University Press, New York, 393 pp. Bound.-Layer Meteorol. 139, 543–549. doi:10.1007/s10546-011-9596-2
- Ferraro, J.R., Nakamoto, K., Brown, C.W., 2003. *Introductory Raman spectroscopy*, 2nd ed. ed. Academic Press, Amsterdam ; Boston.
- Geli, H.M.E., Neale, C.M.U., Watts, D., Osterberg, J., De Bruin, H.A.R., Kohsiek, W., Pack, R.T., Hipps, L.E., 2012. Scintillometer-Based Estimates of Sensible Heat Flux Using Lidar-Derived Surface Roughness. *J. Hydrometeorol.* 13, 1317–1331. doi:10.1175/JHM-D-11-085.1
- Hausner, M.B., Suárez, F., Glander, K.E., Giesen, N. van de, Selker, J.S., Tyler, S.W., 2011. Calibrating Single-Ended Fiber-Optic Raman Spectra Distributed Temperature Sensing Data. *Sensors* 11, 10859–10879. doi:10.3390/s111110859
- Hilgersom, K.P., van Emmerik, T.H.M., Solcerova, A., Berghuijs, W.R., Selker, J.S., van de Giesen, N.C., 2016. Practical considerations for enhanced-resolution coil-wrapped Distributed Temperature Sensing. *Geosci. Instrum. Methods Data Syst. Discuss.* 1–24. doi:10.5194/gi-2016-1

BIBLIOGRAPHY (Continued)

- Keller, C.A., Huwald, H., Vollmer, M.K., Wenger, A., Hill, M., Parlange, M.B., Reimann, S., 2011. Fiber optic distributed temperature sensing for the determination of the nocturnal atmospheric boundary layer height. *Atmospheric Meas. Tech.* 4, 143–149. doi:10.5194/amt-4-143-2011
- Kersey, A.D., 1996. A review of recent developments in fiber optic sensor technology. *Opt. Fiber Technol.* 2, 291–317.
- Kobs, S., Hausner, M.B., 2015. USER GUIDE.docx.
- Korzoun, V.I., 1978. World Water Balance and Water Resources of the Earth. USSR Natl. Comm. Int. Hydrol. Decade.
- Penman, H.L., 1948. Natural evaporation from open water, bare soil and grass, in: *Proceedings of the Royal Society of London A: Mathematical, Physical and Engineering Sciences*. The Royal Society, pp. 120–145.
- Sailxa-ULTIMA-DTS-DATASHEET.pdf, 2015.
- Salesky, S.T., Chamecki, M., Dias, N.L., 2012. Estimating the Random Error in Eddy-Covariance Based Fluxes and Other Turbulence Statistics: The Filtering Method. *Bound.-Layer Meteorol.* 144, 113–135. doi:10.1007/s10546-012-9710-0
- Selker, J.S., Thévenaz, L., Huwald, H., Mallet, A., Luxemburg, W., van de Giesen, N., Stejskal, M., Zeman, J., Westhoff, M., Parlange, M.B., 2006. Distributed fiber-optic temperature sensing for hydrologic systems: RAPID COMMUNICATION. *Water Resour. Res.* 42, n/a-n/a. doi:10.1029/2006WR005326
- Stull, R., 1988. *An Introduction to Boundary Layer Meteorology*. Kluwer Academic Publishers, Dordrecht/Boston/London.
- Swinbank, W.C., 1951. Swinbank_1951_Measurement of Vertical Transfer of Heat and Water Vapor by Eddies in the Lower Atmosphere.pdf.
- Thomas, C.K., Kennedy, A.M., Selker, J.S., Moretti, A., Schroth, M.H., Smoot, A.R., Tufillaro, N.B., Zeeman, M.J., 2012. High-Resolution Fibre-Optic Temperature Sensing: A New Tool to Study the Two-Dimensional Structure of Atmospheric Surface-Layer Flow. *Bound.-Layer Meteorol.* 142, 177–192. doi:10.1007/s10546-011-9672-7
- Tillman, J.E., 1972. The Indirect Determination of Stability, Heat and Momentum Fluxes in the Atmospheric Boundary Layer from Simple Scalar Variables During Dry Unstable Conditions.pdf. *J. Appl. Meteorol.* 11, 783–792. doi:http://dx.doi.org/10.1175/1520-0450(1972)011<0783:TIDOSH>2.0.CO;2

BIBLIOGRAPHY (Continued)

- Tyler, S.W., Selker, J.S., Hausner, M.B., Hatch, C.E., Torgersen, T., Thodal, C.E., Schladow, S.G., 2009. Environmental temperature sensing using Raman spectra DTS fiber-optic methods: DTS FIBER-OPTIC SENSING. *Water Resour. Res.* 45, n/a-n/a. doi:10.1029/2008WR007052
- Ukil, A., Braendle, H., Krippner, P., 2012. Distributed Temperature Sensing: Review of Technology and Applications. *IEEE Sens. J.* 12, 885–892. doi:10.1109/JSEN.2011.2162060
- Van Bavel, C.H.M., 1966. Potential Evaporation: The Combination Concept and Its Experimental Verification. *Water Resour. Res. US Water Conserv. Lab.* 2, 455–467.
- Zeeman, M.J., Selker, J.S., Thomas, C.K., 2015. Near-Surface Motion in the Nocturnal, Stable Boundary Layer Observed with Fibre-Optic Distributed Temperature Sensing. *Bound.-Layer Meteorol.* 154, 189–205. doi:10.1007/s10546-014-9972-9